International Journal of Photoenergy

Dynamics in Photoexcited DNA Bases and Related Molecules

Guest Editors: Yusheng Dou, Zhisong Wang, Fuli Li, and Roland E. Allen

Dynamics in Photoexcited DNA Bases and Related Molecules

International Journal of Photoenergy

Dynamics in Photoexcited DNA Bases and Related Molecules

Guest Editors: Yusheng Dou, Zhisong Wang, Fuli Li, and Roland E. Allen

Editorial Board

Contents

Hindawi Publishing Corporation
International Journal of Photoenergy
Volume 2015, Article ID 501028, 2 pages
http://dx.doi.org/10.1155/2015/501028

Editorial

Dynamics in Photoexcited DNA Bases and Related Molecules

Yusheng Dou,[1,2] Zhisong Wang,[3] Fuli Li,[4] and Roland E. Allen[5]

[1] *Institute of Computational Chemistry, Chongqing University of Posts and Telecommunications, Chongqing 400065, China*
[2] *Department of Physical Sciences, Nicholls State University, P.O. Box 2022, Thibodaux, LA 70310, USA*
[3] *Department of Physics, National University of Singapore, Singapore 117542*
[4] *Department of Applied Physics, Xi'an Jiaotong University, Xi'an 710049, China*
[5] *Department of Physics and Astronomy, Texas A&M University, College Station, TX 77843-4242, USA*

Correspondence should be addressed to Yusheng Dou; yusheng.dou@nicholls.edu

Received 15 September 2014; Accepted 15 September 2014

Deoxyribonucleic acid (DNA), the hereditary basis of life's genetic identity, has been of enormous interest for more than a century and particularly since its structure was determined in 1953. Nucleobases are primary building blocks and UV chromophores in DNA. Exposing DNA to radiation in the 200–300 nm range results in strong UV absorption by these bases, which could lead to photochemical reactions causing DNA damage. Fortunately, highly efficient nonradiative decay pathways exist in DNA bases, assuring that most excited molecules quickly relax to the electronic ground state without leading to harmful reactions. The electron dynamics following photoexcitation plays an important role in this deactivation, which is clearly essential for life. Since the development of ultrafast laser pulses and high performance computers, there has been tremendous progress in understanding the electron dynamics of DNA bases, but it is far from complete.

In this special issue, we selected six peer-reviewed research articles which present recent progress in understanding the electronic response of DNA bases excited by laser pulses, mostly through semiclassical dynamical simulations. There is also a brief review of deactivation processes in DNA bases studied with this approach. In the paragraphs below, we provide a brief overview of the key results in each paper.

In "Detailed Photoisomerization Dynamics of a Green Fluorescent Protein Chromophore Based Molecular Switch," quantum yields were found to be 32% for the *trans*-to-*cis* photoisomerization of BMH and 33% for *cis*-to-*trans*. These simulations indicate that the average excited state lifetime of *trans*-BMH is about 1460 fs, which is shorter than that found for *cis*-BMH (3100 fs). For both the *trans*-to-*cis* and *cis*-to-*trans* reactions, rotation around the central C2=C3 bond is the dominant reaction mechanism. Deexcitation occurs at an avoided crossing near a conical intersection which is close to the midpoint of the rotation.

The paper "Competing Deactivation Channels for Excited π-Stacked Cytosines" suggests that the deactivation channel leading to the electronic ground state of stacked bases competes with the path that leads to dimerization. For both pathways, the initial excited state was found to lead to a charge-separated neutral excimer state by charge transfer. Vibrational energy distribution determines the fate of the excimer at the avoided crossing.

The paper "Electron Correlation Effects on the Longitudinal Polarizabilities and Second Hyperpolarizabilities of Polyenes: A Finite Field Study" reports finite-field-based *ab initio* calculations of the longitudinal polarizabilities (α_L) and second hyperpolarizabilities (γ_L) of conjugated polyenes and proposes that electron correlation reduces linear longitudinal polarizability and enhances longitudinal second hyperpolarizability for short polyenes, with the effects decreasing as the chain length increases.

The paper "Constraint Trajectory Surface-Hopping Molecular Dynamics Simulation of the Photoisomerization of Stilbene" extends the trajectory surface hopping (TSH) method from full to flexible dimensional potential energy surfaces by combining the TSH method with constrained molecular dynamics. In this approach, classical trajectories are followed in Cartesian coordinates with constraints in

internal coordinates, while nonadiabatic switching probabilities are calculated separately in free internal coordinates by Landau-Zener and Zhu-Nakamura formulas along the seam.

The paper "Detailed Molecular Dynamics of the Photochromic Reaction of Spiropyran: A Semiclassical Dynamics Study" reports a realistic simulation study for the photoinduced ring-opening reaction of spiropyran. The main results show two different pathways: one involves hydrogen out-of-plane (HOOP) torsion of the phenyl ring nearby the N atom, and the other dominant pathway corresponds to the ring-opening reaction of *trans*-SP to form the most stable merocyanine (MC) product.

In the paper "Bonded Excimer in Stacked Cytosines: A Semiclassical Simulation Study," the formation of a covalent bond between two stacked cytosines is found to facilitate the deactivation of the electronically excited DNA bases by lowering the energy gap between the LUMO and HOMO.

We believe that the papers published in this special issue represent a significant positive contribution to this general field.

Acknowledgments

We would like to express our sincere appreciation to all the authors for submitting their exciting scientific results to this special issue. We are also grateful to all the reviewers around the world, whose dedicated efforts and high-quality work have made this issue possible. Last but not least, we would like to thank the editorial board of the International Journal of Photoenergy for giving us the opportunity to publish this special issue.

Yusheng Dou
Zhisong Wang
Fuli Li
Roland E. Allen

Hindawi Publishing Corporation
International Journal of Photoenergy
Volume 2015, Article ID 937474, 6 pages
http://dx.doi.org/10.1155/2015/937474

Research Article

Bonded Excimer in Stacked Cytosines: A Semiclassical Simulation Study

Weifeng Wu,[1] Shuai Yuan,[1] Jiajie She,[1] Yusheng Dou,[2] and Roland E. Allen[3]

[1]*Institute of Computational Chemistry, Chongqing University of Posts and Telecommunications, Chongqing, 400065, China*
[2]*Department of Physical Sciences, Nicholls State University, P.O. Box 2022, Thibodaux, LA 70310, USA*
[3]*Department of Physics and Astronomy, Texas A&M University, College Station, TX 77843-4242, USA*

Correspondence should be addressed to Shuai Yuan; yuanshuai@cqupt.edu.cn and Yusheng Dou; yusheng.dou@nicholls.edu

Received 13 May 2014; Accepted 21 July 2014

Academic Editor: Fuli Li

The formation of a covalent bond between two stacked cytosines, one of which is excited by an ultrafast laser pulse, was studied by semiclassical dynamics simulations. The results show that a bonded excimer is created, which sharply lowers the energy gap between the LUMO and HOMO and consequently facilitates the deactivation of the electronically excited molecule. This is different from the case of two stacked adenines, where the formation of a covalent bond alters the nonadiabatic deactivation mechanism in two opposite ways. It lowers the energy gap and consequently leads to the coupling between the HOMO and LUMO levels, thus enhancing the deactivation of the electronically excited molecule. On the other hand, it leads to restriction of the deformation vibration of the pyrimidine in the excited molecule, because of a steric effect, and this delays the deactivation process of the excited adenine molecule with return to the electronic ground state.

1. Introduction

The mechanism and, therefore, the time scale, for electronically excited DNA bases to decay to their ground state, are greatly affected by base stacking. Decay of a monomer DNA base occurs on a subpicosecond time scale through a conical intersection between the lowest electronic excited state and the ground state [1–4]. Excited stacked bases show different nonradiative decay pathways [5]. Poorly stacked bases show a monomer-like decay pathway, while strongly stacked bases exhibit a slower decay channel. The slow decay channel is explained by the formation of an excimer between an excited base and a ground state neighboring base. Excimers have a longer lifetime with substantial charge transfer character [5–11].

Two stacked molecules may form a chemical bond, resulting in a bonded excimer. It has been reported [12, 13] that the formation of a bonded excimer plays a role in the rapid charge-transfer quenching reaction of a singlet excited state formed between cyanoaromatic electron acceptors and pyridine. The density functional theory (DFT) calculations suggest [12, 13] that the formation of a covalent bond between two stacked molecules lowers the energy of charge-transfer state significantly. One question that arises is whether the formation of a chemical bond between two adjacent bases also plays a rule in the nonadiabatic decay process of stacked DNA bases. Since the formation of a chemical bond is considerably exothermic, an excimer (or exciplex if two bases are not identical) already formed in stacked DNA bases may go further to form a bonded excimer (or exciplex).

Our previous semiclassical dynamics simulation [14] for the effect of π-stacking on the decay channels of an adenine molecule excited by an ultrafast laser pulse finds the formation a bonded excimer between two stacked bases after laser excitation. The formation of the bonded excimer shrinks the energy gap between the HOMO and LUMO energy levels and, thus, favors the nonadiabatic decay process. On the other hand, the formation of the bonded excimer also results in steric hindrance of the excited adenine, which restricts the molecular deformation that leads to nonradiative decay to the ground state. The simulation results, thus, lead to the conclusion that the formation of a covalent bond between

two stacked bases alters the electronic structure but also induces the steric effect, with both mechanisms affecting the nonradiative decay of excited DNA base molecules.

The work reported here provides evidence that the formation of a covalent bond dose in fact plays a role in nonadiabatic decay of electronic excitation in two stacked cytosine molecules. Our simulations use a semiclassical dynamics technique, in which all the degrees of freedom of the system are included in the calculations and the forces acting on each nucleus are calculated on-the-fly. The results show that a covalent bond is formed between two adjacent bases in some trajectories after laser excitation and provide fundamental information for understanding this important phenomenon in the nonradiative decay of stacked-bases.

2. Methodology

Our technique here is semiclassical electron-radiation-ion dynamics (SERID). A detailed description of this method has been published elsewhere [15, 16] and only a brief summary is presented here. The valence electrons are treated with a quantum mechanical approach while both the radiation field and the motion of the nuclei are treated classically. The one-electron states are updated by solving the time-dependent Schrödinger equation at each time step (usually 0.05 femtosecond in duration) in a nonorthogonal basis:

$$i\hbar\frac{\partial\mathbf{\Psi}_j}{\partial t} = \mathbf{S^{-1}}\cdot\mathbf{H}\cdot\mathbf{\Psi}_j, \tag{1}$$

where $\mathbf{S}$ represents the overlap matrix of the atomic orbitals. The vector potential $\mathbf{A}$ of the radiation field is included in the electronic Hamiltonian via the time-dependent Peierls substitution [17]:

$$\mathbf{H}_{ab}\left(X-X'\right) = \mathbf{H}^0_{ab}\left(X-X'\right)\exp\left\{\frac{iq}{\hbar c}\mathbf{A}\cdot\left(X-X'\right)\right\}, \tag{2}$$

where $\mathbf{H}_{ab}(X - X')$ is the Hamiltonian matrix element for basis functions a and b on atoms atpositions X and X', respectively, and $q = -e$ is the charge of the electron.

The forces acting on nuclei or ions are computed by the Ehrenfest equation in an "on-the-fly" approach:

$$M_l\frac{d^2X_{l\alpha}}{dt^2} = -\frac{1}{2}\sum_j\Psi_j^+\cdot\left\{\frac{\partial\mathbf{H}}{\partial X_{l\alpha}} - i\hbar\frac{\partial\mathbf{S}}{\partial X_{l\alpha}}\cdot\frac{\partial}{\partial t}\right\}\cdot\Psi_j - \frac{\partial U_{\text{rep}}}{\partial X_{l\alpha}}, \tag{3}$$

where U_{rep} is the effective nuclear-nuclear repulsive potential and $X_{l\alpha} = \langle\widehat{X}_{l\alpha}\rangle$ is the expectation value of the time-dependent Heisenberg operator for the α coordinate of the nucleus labeled by l (with $\alpha = x, y,$ or z).

The Hamiltonian matrix H, overlap matrix S, and effective nuclear-nuclear repulsive potential U_{rep} are calculated in the density-functional tight-binding approximation [18, 19]. These quantities are functions only of the nuclear distance and the results from the calculations for a dimer can be tabulated and employed in the time-dependent calculations. The basis functions used in the present simulations are the 1s atomic orbital of H and the valence s and p orbitals of C and N (spin up and spin down states are not distinguished). In this approach, the electronic energy of a molecule can be written as

$$E_{\text{elec}} = \sum_{i=\text{occ}} n_i\varepsilon_i + \sum_{\alpha>\beta}U_{\text{rep}}\left(\left|X_\alpha - X_\beta\right|\right), \tag{4}$$

where ε_i and $\mathbf{n_i}$ are the eigenvalue and occupation number of Kohn-Sham orbital $\mathbf{i}$. The first summation goes over all occupied orbitals. The effective repulsive potential $U_{\text{rep}}(|X_\alpha - X_\beta|)$ is a function of the interatom distance.

We have previously applied the SERID technique to study nonadiabatic decay in adenine [20, 21], photodissociation of the cyclobutane thymine dimer [22, 23], photoinduced dimerization of thymine [24], and the cytosine dimer [25], and the results were found to be consistent with experimental observations. A limitation of this method is that the simulation trajectory moves along a path produced by averaging over all the terms in the Born-Oppenheimer expansion [26–30]

$$\Psi^{\text{total}}\left(X_n, x_e, t\right) = \sum_i\Psi_i^n\left(X_n, t\right)\Psi_i^e\left(x_e, X_n\right) \tag{5}$$

rather than following the time evolution of a single potential energy surface [28–30] (here, X_n and x_e represent the sets of nuclear and electronic coordinates, respectively, and the Ψ_i^e are eigenstates of the electronic Hamiltonian at fixed X_n). The strengths of the present approach are that it retains all of the X_n nuclear degrees of freedom and it incorporates both the excitation due to a laser pulse and the subsequent deexcitation at an avoided crossing near a conical intersection.

A dynamical simulation was run for ground-state cytosine at room temperature (298 K) for 2000 fs. A second cytosine molecule of the same geometry was oriented such that C_5–C_5' = 3.45 Å, C_6–C_6' = 3.43 Å, and C_5–C_6–C_6'–C_5' = 26.4°; primed labels refer to atoms of the second ground-state cytosine molecule. The simulation was continued for another 2000 fs. Twenty structures at 200 fs intervals were recorded. The structure at 1000 fs is shown in Figure 1, where the two molecules are stacked such that the interatomic distances C_5–C_5' and C_6–C_6' are 3.85 and 3.90 Å, respectively, and the dihedral angle C_4–C_5–C_5'–C_4' is 36.1°. Each of the twenty structures was used as the starting geometry for a simulated trajectory initiated by laser excitation. In the following discussion, the excited cytosine molecule will be referred to as molecule C and the other unexcited molecule as C′.

A 25 fs FWHM laser pulse with a Gaussian profile and photon energy of 4.1 eV was used in the simulations. The selected photon energy corresponds to the energy gap between the LUMO and HOMO, as calculated with the present approximations. A fluence in the range 100 to 300 J/m^2 was used, so that the forces produced do not break any bonds. The simulation was run at the selected laser pulse for 500 trajectories and only a typical trajectory is reported in this paper because other trajectories have shown similar properties.

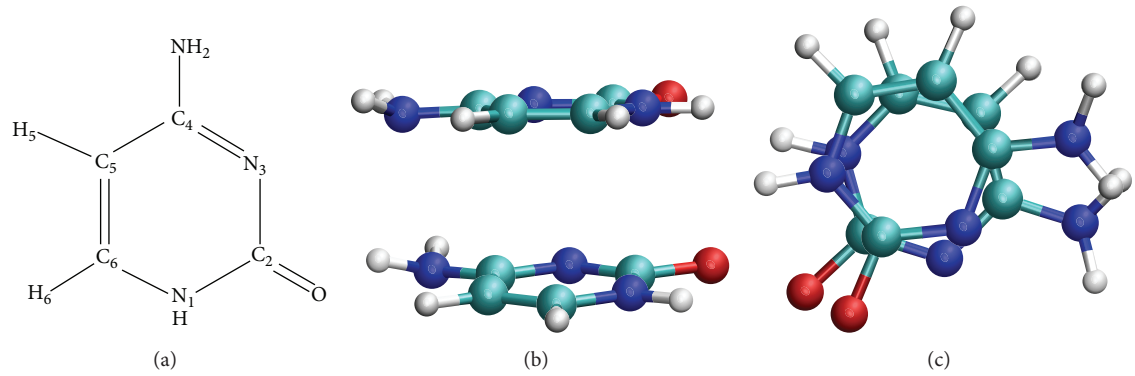

Figure 1: Structure and atomic labeling for the stacked cytosine molecules.

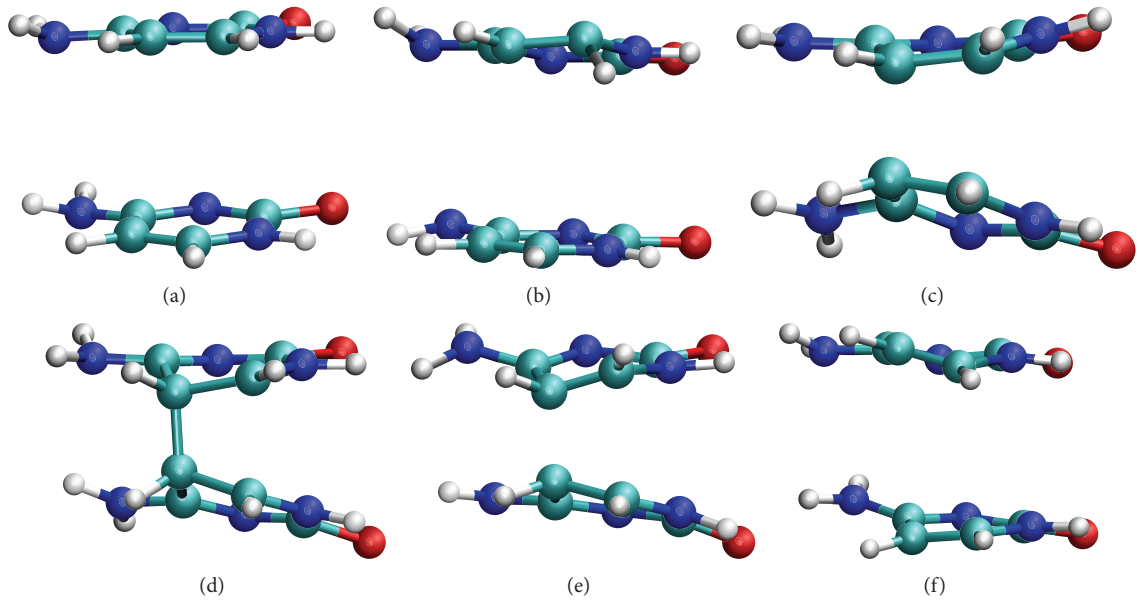

Figure 2: Snapshots taken from the simulation of two stacked cytosine molecules at (a) 0, (b) 244, (c) 923, (d) 964, (e) 993, and (f) 1082 fs.

3. Results and Discussion

The results for a representative trajectory are shown in Figures 2 through 5. Six snapshots from the simulation are shown in Figure 2. Starting from the equilibrated geometry, the bottom molecule is electronically excited by the laser pulse (fluence = 44.01 J/m^2). The excited molecule undergoes an out-of-plane vibration of the N atom from 244 fs to 923 fs (Figures 2(b) and 2(c)). The unexcited molecule also becomes active in vibration because of the stacking interaction. The planar structure of both molecules shows a significant deformation at the C_5 and C_5' sites after 923 fs (Figure 2(c)) and a chemical bond has been formed between these atoms after 923 fs (Figure 2(d)). After 993 fs, the bond has been broken and two stacked molecules move away from each other (Figure 2(f)).

The variations of the distance between the C_5 and C_5' atoms with time are shown in Figure 3 which confirms that the formation of a chemical bond with a length of ~1.5 Å takes place at about 964 fs; the bond stays stable for a short time and is then dissociated. Figure 3 also shows the changes in the distance between the C_5 and C_5' atoms, providing evidence for the potential formation of the cyclobutane dimer.

The variations with time of the HOMO and LUMO levels of two stacked molecules are presented in Figure 4(a), and the time-dependent population of these frontier molecular orbitals is plotted in Figure 4(b). The gap between the HOMO and LUMO initially is about 4.5 eV and becomes less than 2.5 eV after 100 fs, when the laser pulse ends. There are two avoided crossings at 923 and 993 fs when the gap is about 0.06 and 0.18 eV, respectively. The energies of the HOMO and LUMO move back to approximately their initial values after that. It is seen from Figure 4(b) that the laser excitation promotes about 1 electron from the HOMO to the LUMO, and the couplings between the HOMO and LUMO at ~920 fs and ~990 fs lead to the transfer of electrons from LUMO to

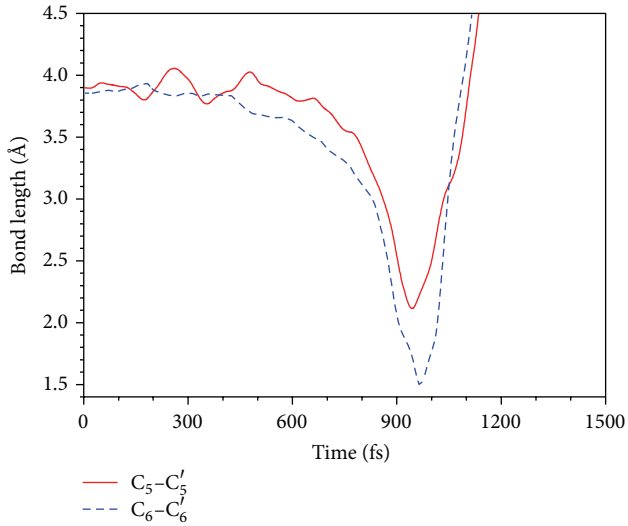

FIGURE 3: The variations with time of the lengths between the C_5 and C_5' atoms and the C_6 and C_6' atoms in two stacked cytosine molecules.

HOMO. The initial promotion of electrons from the HOMO to the LUMO brings molecule C to an electronically excited state and excites some vibrational modes, for example, the out-of-plane vibration of $-NH_2$, as seen in Figure 2. The decrease in the energy gap between the HOMO and LUMO after laser excitation is attributed to the changes in the structure of stacked bases molecules due to the excitation of different vibrational modes. Further diminution of the energy gap from ~850 fs to ~1050 fs is a result of the strong interaction between the two stacked molecules. Specifically, the avoided crossings at 923 fs and 993 fs are associated with the interaction between the C_6 and C_6' atoms and the C_5 and C_5' atoms, which leads to the formation of the chemical bond between two adjacent molecules. The avoided crossings result in the transfer of electrons from the LUMO to HOMO, which eventually brings excited molecules to the electronic ground state.

Figure 5 shows the variation with time of the C_5–C_6 and C_5'–C_6' bond lengths. The C_5–C_6 bond stretches from an initial value of ~1.33 Å to ~1.47 Å after laser excitation. It remains at this length until ~1000 fs and then returns to approximately its initial length. On the other hand, the same bond for the unexcited molecule only vibrates about its initial length for the entire simulation time. The C_4'–C_5' bond length sharply rises up from ~1.37 Å to ~1.48 Å after 900 fs and suddenly drops down to its initial value after 1000 fs.

The changes in the C_5–C_6 bond length is due to excitation and deexcitation of the cytosine molecule, while the changes in the C_5' – C_6' bond length between ~900 fs and ~1000 fs can be attributed to the formation of the bonded excimer between two adjacent cytosine molecules.

The simulation results presented in this section suggest the photophysical processes described below. By raising about 1 electron from the HOMO to the higher level frontier molecular orbitals, the laser pulse promotes the top molecule from the electronic ground state to a low-lying energy state $\pi\pi^*$. In this electronically excited state, the C_5–C_6 bond becomes longer. The interaction between excited base and unexcited base due to the stacking effect attracts the two molecules closer to each other. At about 900 fs, a covalent bond is formed between the C_5 and C_5' atoms, leading to the formation of the bonded excimer state. The formation of the covalent bond between two cytosine molecules breaks the π-π conjugation of the unexcited cytosine. This lengthens the C_5'–C_6' bond and shortens the C_4'–C_5' and C_6'–N_1' bonds (which are not shown here). The energy gap between the LUMO and HOMO decreases sharply from 900 fs to 1100 fs, suggesting that the bonded excimer state is substantially lower than the unbonded state in energy. After 900 fs, the system thus evolves as a bonded excimer state. It then enters the vicinity of the conical intersection twice, at 923 fs and 993 fs, respectively, and it decays to the ground state through a channel resulting from the coupling between the LUMO and HOMO. The coupling occurs primarily because of the formation of the covalent bond between two adjacent molecules. The return to the electronic ground state of the excited molecule is confirmed by the changes in the bond lengthens described above.

The formation of a covalent bond between two adjacent molecules has also been suggested in stacked adenines [14]. It was found by semiclassical dynamics simulations that the bond formation and breaking greatly alter the coupling, leading to decays of the excited system to the ground state and suggesting the involvement of the bonded excimer in the nonradiative decay process for stacked bases. The formation of a covalent bond between two stacked adenine molecules has two opposite effects on nonradiative decay. First it stabilizes the excimer state, which is evidenced by the decrease in the LUMO energy level and thus makes a positive contribution to the excited state lifetime. On the other hand, it limits the conformational flexibility of each molecule. For example, this bond hinders the out-of-plane deformations of the pyrimidine ring [21, 22] and, therefore, limits the freedom to achieve the deformation required for accessing the deactivating conical intersections.

Compared to adenine, the cytosine conformation exhibits only a very limited steric effect. This may, at least partially, explain the fact that stacked cytosines have a shorter deactivation time scale than stacked adenine.

4. Conclusion

The present investigation focuses on the formation of covalent bond between two stacked cytosines after laser excitation, which strongly affects the HOMO and LUMO energy levels and dominates their couplings. It is these couplings that lead to nonadiabatic decay of the excited system to the electronic ground state. The results for stacked cytosines are different from those for stacked adenines, where formation of a covalent bond affects nonadiabatic decay of the excited system in two different ways. It stabilizes the bonded excimer state between two stacked adenine molecules and also leads to a steric effect which inhibits nonradiative decay.

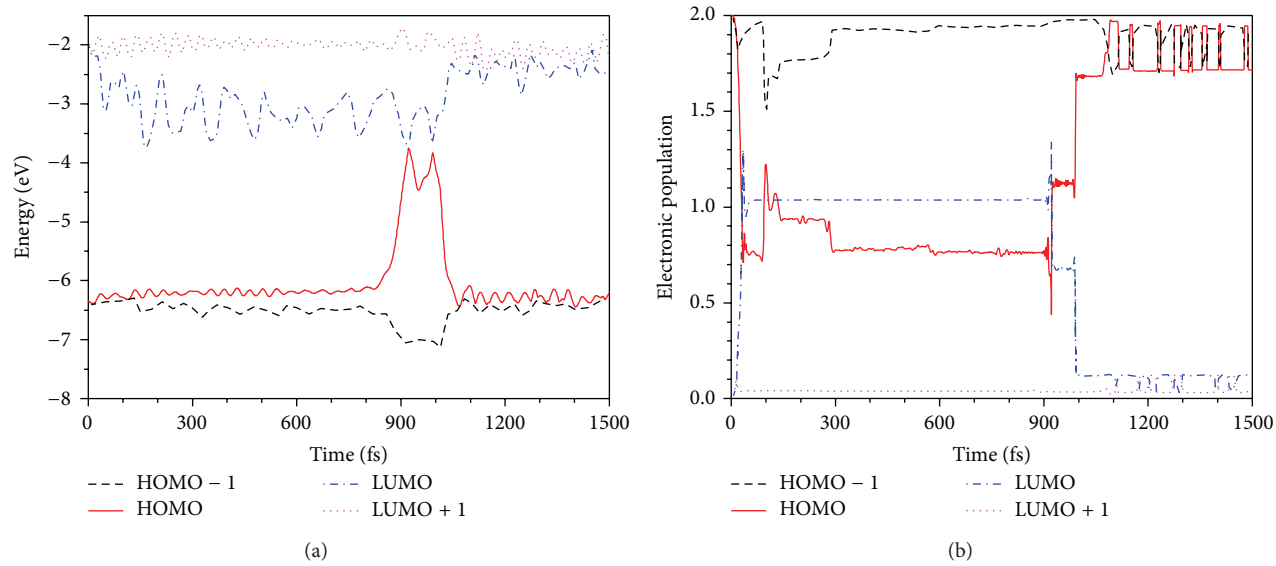

Figure 4: (a) The variations with time, (b) the time-dependent populations of the HOMO-1, HOMO LUMO, and LUMO + 1 energies of two stacked cytosine molecules.

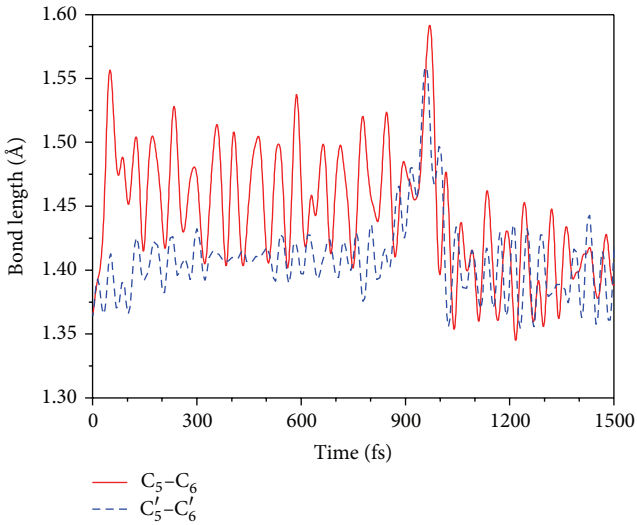

Figure 5: The variations with time of the lengths between the C_5 and C_6 atoms and the C_5' and C_6' atoms in two stacked cytosine molecules.

Conflict of Interests

The authors declare that there is no conflict of interests regarding the publication of this paper.

Acknowledgments

This work is supported by the National Natural Science Foundation of China (Grants no. U1330138 and no. 21203259) and the Natural Science Foundation Project of CQ CSTC (cstc2011jjA00009) and Project of the Science Technology Foundation of Chongqing Education Committee, China (nos. KJ120516 and KJ120521), and Telecommunications (no. A2012-92).

References

[1] J.-M. L. Pecourt, J. Peon, and B. Kohler, "Ultrafast internal conversion of electronically excited RNA and DNA nucleosides in water," *Journal of the American Chemical Society*, vol. 122, no. 38, pp. 9348–9349, 2000.

[2] N. Ismail, L. Blancafort, M. Olivucci, B. Kohler, and M. A. Robb, "Ultrafast decay of electronically excited singlet cytosine via a $\pi,\pi*$ to $n_O,\pi*$ state switch," *Journal of the American Chemical Society*, vol. 124, no. 24, pp. 6818–6819, 2002.

[3] M. Z. Zgierski, S. Patchkovskii, T. Fujiwara, and E. C. Lim, "The role of out-of-plane deformations in subpicosecond internal conversion of photoexcited purine bases: absence of the ultrafast decay channel in propanodeoxyguanosine," *Chemical Physics Letters*, vol. 440, no. 1–3, pp. 145–149, 2007.

[4] L. Serrano-Andrés, M. Merchán, and A. C. Borin, "A three-state model for the photophysics of adenine," *Chemistry*, vol. 12, no. 25, pp. 6559–6571, 2006.

[5] C. T. Middleton, K. de la Harpe, C. Su, Y. K. Law, C. E. Crespo-Hernández, and B. Kohler, "DNA excited-state dynamics: from single bases to the double helix," *Annual Review of Physical Chemistry*, vol. 60, pp. 217–239, 2009.

[6] Z. Pan, M. McCullagh, G. C. Schatz, and F. D. Lewis, "Conformational control of thymine photodimerization in purine-containing trinucleotides," *Journal of Physical Chemistry Letters*, vol. 2, no. 12, pp. 1432–1438, 2011.

[7] M. Z. Zgierski, T. Fujiwara, and E. C. Lim, "Conical intersections and ultrafast intramolecular excited-state dynamics in nucleic acid bases and electron donor-acceptor molecules," *Chemical Physics Letters*, vol. 463, no. 4–6, pp. 289–299, 2008.

[8] C. E. Crespo-Hernández, B. Cohen, and B. Kohler, "Molecular spectroscopy: complexity of excited-state dynamics in DNA—reply," *Nature*, vol. 441, no. 7094, article E8, 2006.

[9] B. Cohen, P. M. Hare, and B. Kohler, "Ultrafast excited-state dynamics of adenine and monomethylated adenines in solution: implications for the nonradiative decay mechanism," *Journal of the American Chemical Society*, vol. 125, no. 44, pp. 13594–13601, 2003.

[10] T. Takaya, C. Su, K. de la Harpe, C. E. Crespo-Hernández, and B. Kohler, "UV excitation of single DNA and RNA strands produces high yields of exciplex states between two stacked bases," *Proceedings of the National Academy of Sciences of the United States of America*, vol. 105, no. 30, pp. 10285–10290, 2008.

[11] C. E. Crespo-Hernández, B. Cohen, and B. Kohler, "Base stacking controls excited-state dynamics in A·T DNA," *Nature*, vol. 436, no. 7054, pp. 1141–1144, 2005.

[12] Y. S. Wang, O. Haze, J. P. Dinnocenzo, S. Farid, R. S. Farid, and I. R. Gould, "Bonded exciplexes. A new concept in photochemical reactions," *The Journal of Organic Chemistry*, vol. 72, no. 18, pp. 6970–6981, 2007.

[13] Y. Wang, O. Haze, J. P. Dinnoeenzo, S. Farid, R. S. Farid, and I. R. Gould, "Bonded exciplex formation: electronic and stereoelectronic effects," *The Journal of Physical Chemistry A*, vol. 112, no. 50, pp. 13088–13094, 2008.

[14] S. Yuan, W.-Y. Zhang, A.-Y. Li, Y.-M. Zhu, and Y.-S. Dou, "Dynamics simulation of a new deactivation pathway for stacked adenines," *Acta Physico—Chimica Sinica*, vol. 27, no. 4, pp. 825–830, 2011.

[15] Y. Dou, B. R. Torralva, and R. E. Allen, "Semiclassical electron-radiation-ion dynamics (SERID) and cis-trans photoisomerization of butadiene," *Journal of Modern Optics*, vol. 50, no. 15-17, pp. 2615–2643, 2003.

[16] Y. Dou, B. R. Torralva, and R. E. Allen, "Interplay of electronic and nuclear degrees of freedom in a femtosecond-scale photochemical reaction," *Chemical Physics Letters*, vol. 392, no. 4–6, pp. 352–358, 2004.

[17] T. B. Boykin, R. Chris Bowen, and G. Klimeck, "Electromagnetic coupling and gauge invariance in the empirical tight-binding method," *Physical Review B*, vol. 63, no. 24, Article ID 245314, 2001.

[18] D. Porezag, T. Frauenheim, T. Köhler, G. Seifert, and R. Kaschner, "Construction of tight-binding-like potentials on the basis of density-functional theory: application to carbon," *Physical Review B*, vol. 51, no. 19, pp. 12947–12957, 1995.

[19] M. Elstner, D. Porezag, G. Jungnickel et al., "Self-consistent-charge density-functional tight-binding method for simulations of complex materials properties," *Physical Review B*, vol. 58, no. 11, pp. 7260–7268, 1998.

[20] Y. B. Lei, S. Yuan, Y. S. Dou, Y. B. Wang, and Z. Y. Wen, "Detailed dynamics of the nonradiative deactivation of adenine: a semiclassical dynamics study," *Journal of Physical Chemistry A*, vol. 112, no. 37, pp. 8497–8504, 2008.

[21] Y. S. Dou, S. S. Xiong, W. F. Wu, S. Yuan, and H. Tang, "Photoinduced dissociation of cyclobutane thymine dimer studied by semiclassical dynamics simulation," *Journal of Photochemistry and Photobiology B: Biology*, vol. 101, no. 1, pp. 31–36, 2010.

[22] W. Y. Zhang, S. Yuan, Z. J. Wang et al., "A semiclassical dynamics simulation for a long-lived excimer state of π-stacked adenines," *Chemical Physics Letters*, vol. 506, no. 4–6, pp. 303–308, 2011.

[23] S. Yuan, Z. Shen, W. Y. Zhang, Y. S. Dou, and G. Y. Lo, "Thymine dimer splitting in the T<>T-G trinucleotide model system: a semiclassical dynamics and TD-DFT study," *International Journal of Biological Macromolecules*, vol. 66, pp. 267–272, 2014.

[24] W. Zhang, S. Yuan, A. Li, Y. Dou, J. Zhao, and W. Fang, "Photoinduced thymine dimerization studied by semiclassical dynamics simulation," *The Journal of Physical Chemistry C*, vol. 114, no. 12, pp. 5594–5601, 2010.

[25] S. Yuan, W. Zhang, L. Liu, Y. Dou, W. Fang, and G. V. Lo, "Detailed mechanism for photoinduced cytosine dimerization: a semiclassical dynamics simulation," *Journal of Physical Chemistry A*, vol. 115, no. 46, pp. 13291–13297, 2011.

[26] R. E. Allen, T. Dumitrica, and B. Torralva, "Electronic and structural response of materials to fast, intence laser pluse," in *Ultrafast Physical Processes in Semiconductors*, K. T. Tsen, Ed., pp. 315–384, Academic Press, New York, NY, USA, 2001.

[27] W. Domcke, D. R. Yarkony, and H. Köppel, *Conical Intersections: Electronic Structure, Dynamics & Spectroscopy*, World Scientific Publishing, Singapore, 2004.

[28] M. Baer, *Beyond Born-Oppenheimer: Electronic Nonadiabatic Coupling Terms and Conical Intersections*, Wiley-Interscience, Hoboken, NJ, USA, 2006.

[29] M. J. Bearpark, F. Bernardi, S. Clifford, M. Olivucci, M. A. Robb, and T. Vreven, "Cooperating rings in cis-stilbene lead to an S0/S1 conical intersection," *The Journal of Physical Chemistry A*, vol. 101, no. 21, pp. 3841–3847, 1997.

[30] B. G. Levine and T. J. Martínez, "Isomerization through conical intersections," *Annual Review of Physical Chemistry*, vol. 58, pp. 613–634, 2007.

Hindawi Publishing Corporation
International Journal of Photoenergy
Volume 2014, Article ID 597165, 11 pages
http://dx.doi.org/10.1155/2014/597165

Research Article

Detailed Photoisomerization Dynamics of a Green Fluorescent Protein Chromophore Based Molecular Switch

Chen-Wei Jiang,[1] Ai-Ping Fang,[1] Di Zhao,[1] Hong-Rong Li,[1] Rui-Hua Xie,[1,2] and Fu-Li Li[1]

[1] *MOE Key Laboratory for Nonequilibrium Synthesis and Modulation of Condensed Matter and Department of Applied Physics, Xi'an Jiaotong University, Xi'an 710049, China*
[2] *Department of Physics, Hubei University, Wuhan 430062, China*

Correspondence should be addressed to Chen-Wei Jiang; jiangcw@mail.xjtu.edu.cn and Fu-Li Li; flli@mail.xjtu.edu.cn

Received 25 April 2014; Accepted 16 July 2014; Published 3 September 2014

Academic Editor: Yusheng Dou

With density-functional-based nonadiabatic molecular dynamics simulations, *trans*-to-*cis* and *cis*-to-*trans* photoisomerizations of a green fluorescent protein chromophore based molecule 4-benzylidene-2-methyloxazol-5(4H)-one (BMH) induced by the excitation to its S_1 excited state were performed. We find a quantum yield of 32% for the *trans*-to-*cis* photoisomerization of BMH and a quantum yield of 33% for its *cis*-to-*trans* photoisomerization. For those simulations that did produce *trans*-to-*cis* isomerization, the average S_1 excited state lifetime of *trans*-BMH is about 1460 fs, which is much shorter than that of *cis*-BMH (3100 fs) in those simulations that did produce *cis*-to-*trans* isomerization. For both photoisomerization processes, rotation around the central C2=C3 bond is the dominant reaction mechanism. Deexcitation occurs at an avoided crossing near the S_1/S_0 conical intersection, which is near the midpoint of the rotation.

1. Introduction

Molecules with the ability to undergo photoisomerization under radiation would have potential applications in molecular switches and other molecular devices. Photoisomerization mechanisms of stilbene [1–3], fulgide [4–6], diarylethene [7–9], and azobenzene [10–14], together with their derivatives [15–19], have been widely studied during the last two decades. Despite their appealing features as effective molecular switches, azobenzene derivatives and above photochromic compounds are just examples of a whole family of compounds capable of performing controlled isomerization reactions. The discovery of new or alternative photoswitch types could expand the applicability of the switch concept to different and increasingly complex molecular environments.

The chromophore of the green fluorescent protein, as a biomolecule from jellyfish *Aequorea victoria*, has been widely used as a genetically encoded noninvasive fluorescence marker in bioimaging [20]. Recently, several studies have revealed that the green fluorescent protein chromophore and its different modifications undergo photo-induced Z/E isomerization under radiation [21–26], which offer them the opportunity to be molecular switches. Through investigation of several spectral modification of synthetic chromophore analogues of wild-type green fluorescent protein, Voliani et al. [21] found that *cis*-to-*trans* photoisomerization should be a general mechanism of green fluorescent protein chromophores whose efficiency can be modulated by the detailed mutant-specific protein environment. Using femtosecond fluorescence upconversion spectroscopy and quantum chemical calculations, Rafiq et al. [22] investigated two green fluorescent protein chromophore analogs and proposed a multicoordinate relaxation mechanism. Oxazolone analogs, as well-known intermediates in the synthesis of green fluorescent protein derivatives, have attracted relatively little attention in terms of their photoswitching ability. Very recently, several oxazolone analogs of the green fluorescent protein chromophore were synthesized and predicted to be good candidates for molecular switches by Blanco-Lomas et al. [27].

To furnish a deeper and detailed mechanistic understanding of the photoisomerization reaction of those green fluorescent protein chromophore based molecular switches, semiclassical nonadiabatic molecular dynamics simulations were

performed for a molecule 4-benzylidene-2-methyloxazol-5(4H)-one (BMH, named as 2e in [27]) in our group. We found that the average lifetime of the S_1 excited state in *trans*-BMH is about 1450 fs, much shorter than that of *cis*-BMH (3100 fs), which is in good agreement with the experimental result [27].

This paper is organized as follows. Our semiclassical nonadiabatic molecular dynamics simulation method is briefly reviewed in Section 2. The detailed results and discussions are represented in Section 3, followed by a conclusion in Section 4.

2. Methodology

Our nonadiabatic molecular dynamics simulation method was named semiclassical electron-radiation-ion dynamics (SERID), which has been described in detail elsewhere [28, 29]. We only briefly review it under below.

To obtain the evolution equations of electrons and nuclei, we postulate a mixed classical-quantum action [30–32] $S = \int dt\, L$, where

$$L = \frac{1}{2}\left\langle \Psi_e \right| \left(i\hbar \frac{\partial}{\partial t} - \mathscr{H}_e \right) \left| \Psi_e \right\rangle + \text{h.c.} + \frac{1}{2}\sum_{k\alpha} M_k \left(\frac{dX_{k\alpha}}{dt} \right)^2 - U_{\text{rep}}. \quad (1)$$

$\mathscr{H}_e$ is the electronic Hamiltonian, $|\Psi_e\rangle$ is the electronic state, "h.c." means "Hermitian conjugate," k labels a nucleus with spatial coordinates α, and U_{rep} is the repulsive interaction between nuclei and ion cores. As shown in [32], if one makes the usual time-dependent effective-field approximation and employs a nonorthogonal basis, extremalization of this action leads to the time-dependent Schrödinger equation:

$$i\hbar \frac{\partial}{\partial t} \boldsymbol{\psi}(t) = \mathbf{S}^{-1} \cdot \mathbf{H} \cdot \boldsymbol{\psi}(t) \quad (2)$$

and to the equation of motion for the nuclei

$$M \frac{d^2 X}{dt^2} = -\frac{1}{2}\sum_n \boldsymbol{\psi}_n^\dagger \cdot \left(\frac{\partial \mathbf{H}}{\partial X} - i\hbar \frac{\partial \mathbf{S}}{\partial X} \frac{\partial}{\partial t} \right) \cdot \boldsymbol{\psi}_n + \text{h.c.} - \frac{\partial U_{\text{rep}}}{\partial X}. \quad (3)$$

The Hamiltonian matrix **H**, overlap matrix **S**, and repulsive potential U_{rep} are obtained from the density-functional-based parameterizations of Frauenheim and coworkers [33, 34].

The results of [14, 35–44] calculated with SERID method have provided a clear demonstration of the following features of simulations based on Ehrenfest dynamics: (1) electronic transitions are automatically observed at an avoided crossing near a conical intersection in configuration space predicted by Teller [45, 46], with energy released to molecular vibrations; (2) these transitions occur rapidly, over a time interval of ~2 femtosecond, during which the nuclei do not move appreciably.

Table 1: Optimized geometrical parameters of *cis*-BMH and *trans*-BMH, calculated with our SERID method and B3LYP/6-311G(d,p) implemented in Gaussian 03 software package. The lengths are in Å and the dihedral angles and bond angles are in degrees.

	SERID	B3LYP/6-311G(d,p)
cis		
C1C2C3C6	180.0	180.0
C3C2C1C5	0.0	0.0
C1C2H12C3	180.0	180.0
C1C2C3	127.0	129.9
C2C1C5	122.9	123.5
C2C3N21	127.6	129.4
C2–C3	1.37	1.35
C1–C2	1.45	1.45
C3–N21	1.42	1.40
trans		
C1C2C3C6	0.1	0.0
C3C2C1C5	0.1	0.0
C1C2H12C3	180.0	180.0
C1C2C3	130.8	134.3
C2C1C5	124.6	125.4
C2C3N21	119.0	120.3
C2–C3	1.37	1.36
C1–C2	1.45	1.45
C3–N21	1.43	1.41

In the present work, we have made a little change in the procedure that should lead to better results for the quantum yields. By simply placing an electron in the lowest unoccupied molecular orbital (LUMO) and a hole in the highest occupied molecular orbital (HOMO) in the beginning of nonadiabatic simulations, we focus exclusively on the S_0-S_1 excitation, as in other excited state molecular dynamics simulations [47, 48]. However, we still allow deexcitation to occur automatically at an avoided crossing near a conical intersection, since we found that deexcitation was already nearly complete in our present simulations.

3. Results and Discussion

We optimized the *cis* and *trans* structures of BMH in the ground state, starting from 300 K through reducing the nuclear velocities by a factor of 0.9997 after each time step of 0.01 fs until the total molecular kinetic energy was less than 10^{-7} eV. The optimized geometries of *cis* and *trans* BMH are presented in Figure 1, with their geometrical parameters summarized in Table 1. We also optimized both structures with B3LYP/6-311G(d,p) implemented in Gaussian 03 software package [49]. Both results are in good agreement with each other. The electronic energy of *cis*-BMH is 0.11 eV lower than that of *trans*-BMH in our SERID calculation, agreeing well with the energy difference (0.13 eV) obtained with B3LYP/6-311G(d,p) method. Both results confirm that *cis*-BMH is more stable than its *trans* isomer. Starting from its optimized geometry, each molecule was then heated to 300 K

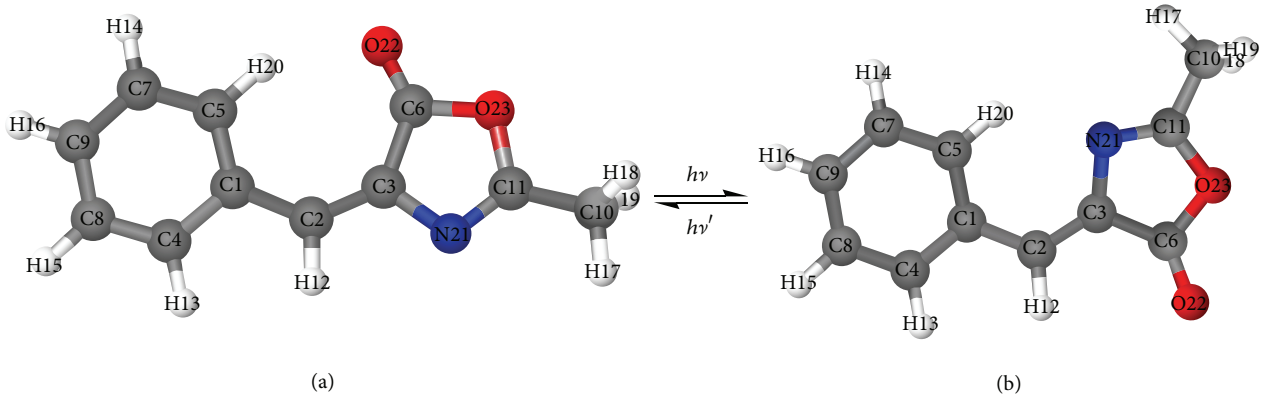

(a) (b)

Figure 1: Optimized geometries of (a) *trans* and (b) *cis* structures of BMH calculated with SERID. All atoms are labelled.

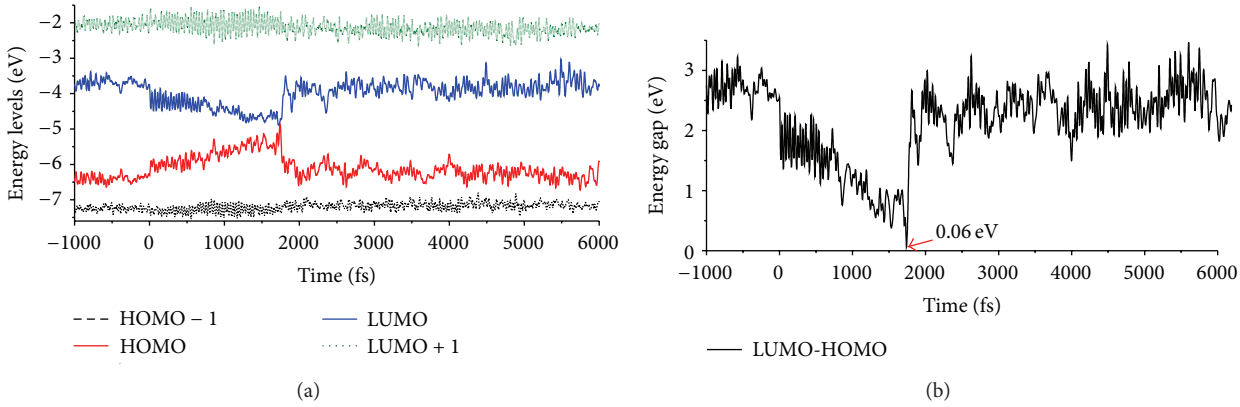

(a) (b)

Figure 2: Time dependence of (a) orbital energies from HOMO − 1 to LUMO + 1 and (b) LUMO-HOMO energy gap in BMH for the *trans*-to-*cis* isomerization. 0.06 eV is the minimum value of the LUMO-HOMO energy gap in this simulation.

(via random velocities resulting in this temperature) and then allowed to equilibrate and move in the electronic ground state for 10000 fs. The initial conditions for various simulations were then sampled from the configurations during the last half of this 10000 fs interval.

3.1. trans-to-cis Photoisomerization of BMH. Starting from the first excited state of *trans*-BMH with different initial conditions, 90 simulations have been performed, 29 of which resulted in *trans*-to-*cis* isomerization. So the quantum yield of this reaction in our calculation is about 32%. For the 29 simulations which did produce *trans*-to-*cis* isomerization, the average S_1 lifetime of *trans*-BMH is about 1460 fs. A detailed discussion of the isomerization mechanism in a representative simulation with a 1740 fs S_1 lifetime is presented below.

BMH molecule is excited to the S_1 excited state at time $t = 0$ fs. To compare the results before and after the excitation, the results before 0 fs are also presented in Figures 2–7 below. Time dependence of the four orbital energies nearest the initial HOMO-LUMO gap are displayed in Figure 2. As we can see, after the excitation at 0 fs, only the HOMO and LUMO energy levels are affected evidently. The energy gap between HOMO and LUMO orbitals, as shown in Figure 2(b), decreases continuously from 2.55 eV to 0.06 eV until 1739 fs. After about 1810 fs, the energy gap between HOMO and LUMO returns to about 2.66 eV and then vibrates around this new value until the end of our simulation. Electron occupations for the four orbitals presented in Figure 2(a) after the excitation are shown in Figure 3. As we can see, BMH deexcites to its ground state at about 1740 fs in 4 fs interval; nearly all electrons return to their ground state. The lifetime of the S_1 excited state in *trans*-BMH is thus about 1740 fs.

Variations of geometry for BMH are displayed in Figures 4–7. As displayed in Figure 4, dihedral angle C1C2C3C6 vibrates around 0° before the excitation at 0 fs, after the excitation, which increases continuously from −27° to about 73° at 1740 fs when BMH returns to the ground state. After the deexcitation at 1740 fs, the rotation around C2=C3 bond continues. Dihedral angle C1C2C3C6 reaches 180° (the optimized value for dihedral angle C1C2C3C6 in *cis*-BMH) at about 2040 fs and then vibrates around this new value, which can demonstrate that the molecule arrives at its *cis* geometry in about 2040 fs. Atomic distance between H20 and N21 displayed in Figure 7(c) can be another confirmation for the final *cis* geometry. After the excitation at 0 fs, the distance between H20 and N21 decreases continuously from about 4.4 Å to 2.2 Å until 2040 fs and then vibrates around this value until the end of our simulation. Other two dihedral

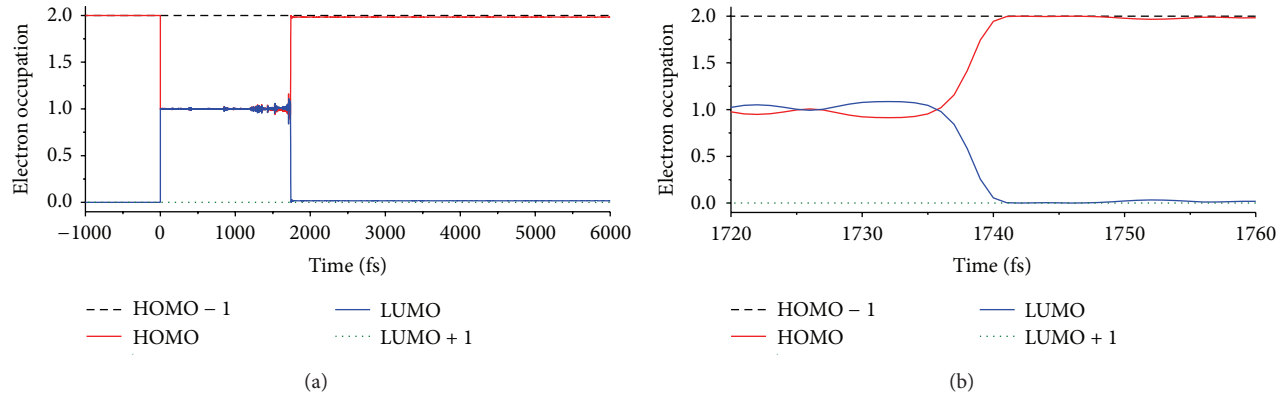

Figure 3: (a) Evolution of electron occupations in BMH from HOMO − 1 to LUMO + 1 for the *trans*-to-*cis* isomerization. (b) Details of Figure 3(a) from 1720 to 1760 fs.

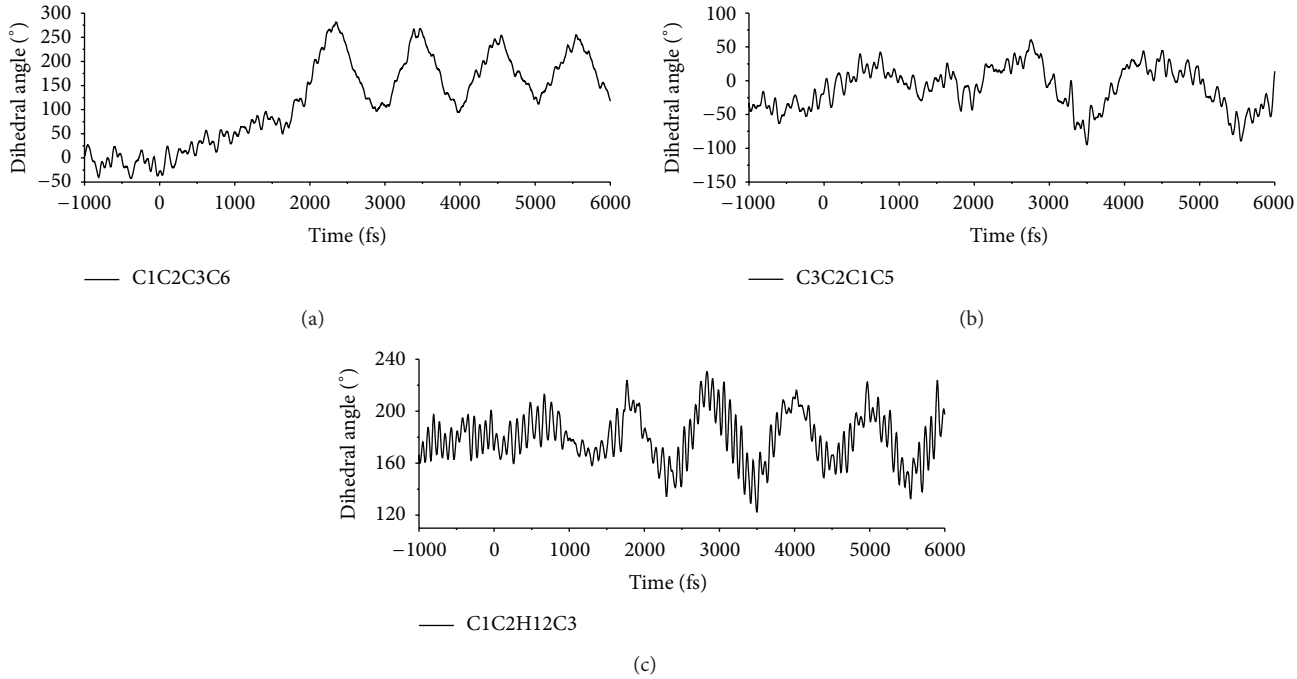

Figure 4: Time dependence in BMH of (a) C1C2C3C6 dihedral angle, (b) C3C2C1C5 dihedral angle,and (c) C1C2H12C3 dihedral angle for the *trans*-to-*cis* isomerization. All labels are defined in Figure 1.

angles C3C2C1C5 and C1C2H12C3 are also displayed in Figure 4. During the whole simulation, C3C2C1C5 vibrates around 0°. That is, there is no evident rotation around C1–C2 bond. C1C2H12C3 also does not vary evidently during the whole simulation and keeps on vibrating around 180°, which demonstrates that H12 atom stays nearly in a plane with atoms C1, C2, and C3 all the time.

Three bond angles in BMH during the *trans*-to-*cis* isomerization are presented in Figure 5. As we can see, during the whole simulation, C1C2C3 bond angle keeps on vibrating around 125°, while C2C1C5 bond angle keeps on staying around 121°. C2C3N21 vibrates around 119° (the optimized C2C3N21 value in *trans*-BMH) before the excitation at 0 fs and then stays around 128° (the optimized C2C3N21 value in *cis*-BMH) after the deexcitation at 1740 fs.

Time dependence of five bond lengths in BMH is shown in Figures 6 and 7. As shown in Figure 6, after the excitation at 0 fs, C2=C3 bond is weakened, increasing from 1.37 Å to 1.47 Å and then returning to 1.37 Å after the deexcitation at 1740 fs. On the other hand, other two bond lengths presented in Figure 6, C1–C2 and C3–N21, are shortened from 1.47 Å to 1.40 Å and from 1.43 Å to 1.37 Å after the excitation at 0 fs, respectively. After the deexcitation at 1740 fs, both bond angles, C1–C2 and C3–N21, return to their initial values before the excitation. Time dependence of other two carbon-carbon bonds, C3–C6 and C1–C4, which are connected with

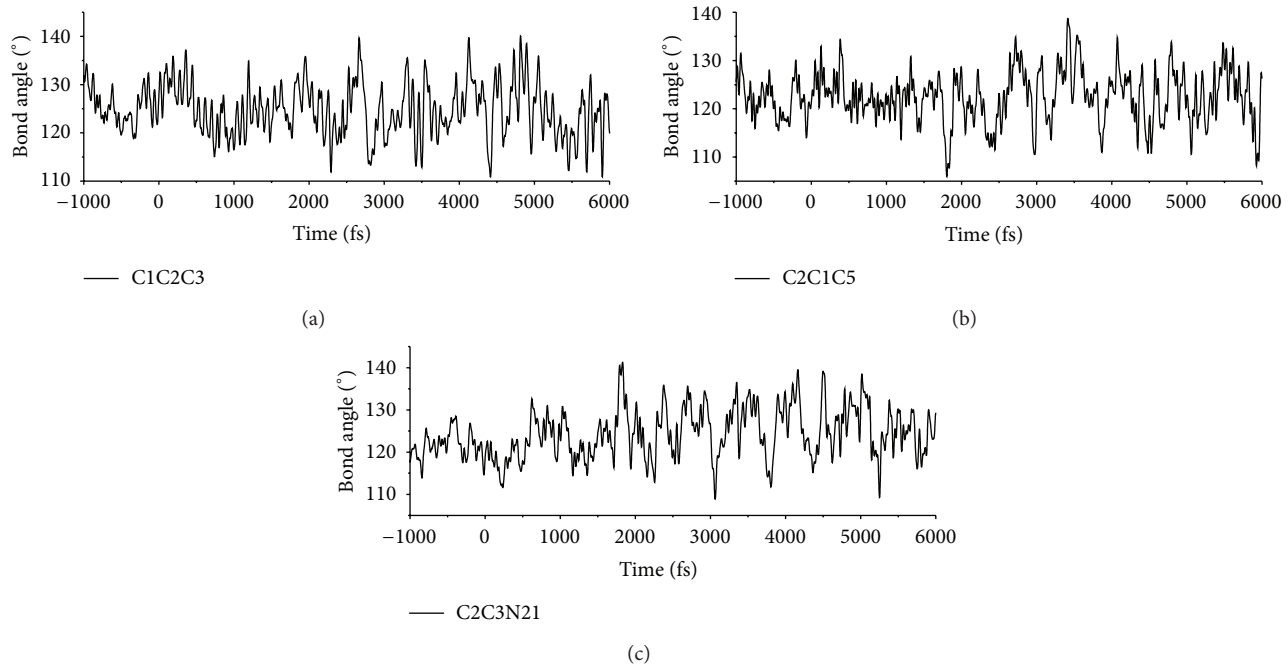

Figure 5: Time dependence in BMH of three bond angles: (a) C1C2C3, (b) C2C1C5, and (c) C2C3N21 for the *trans*-to-*cis* isomerization. All labels are defined in Figure 1.

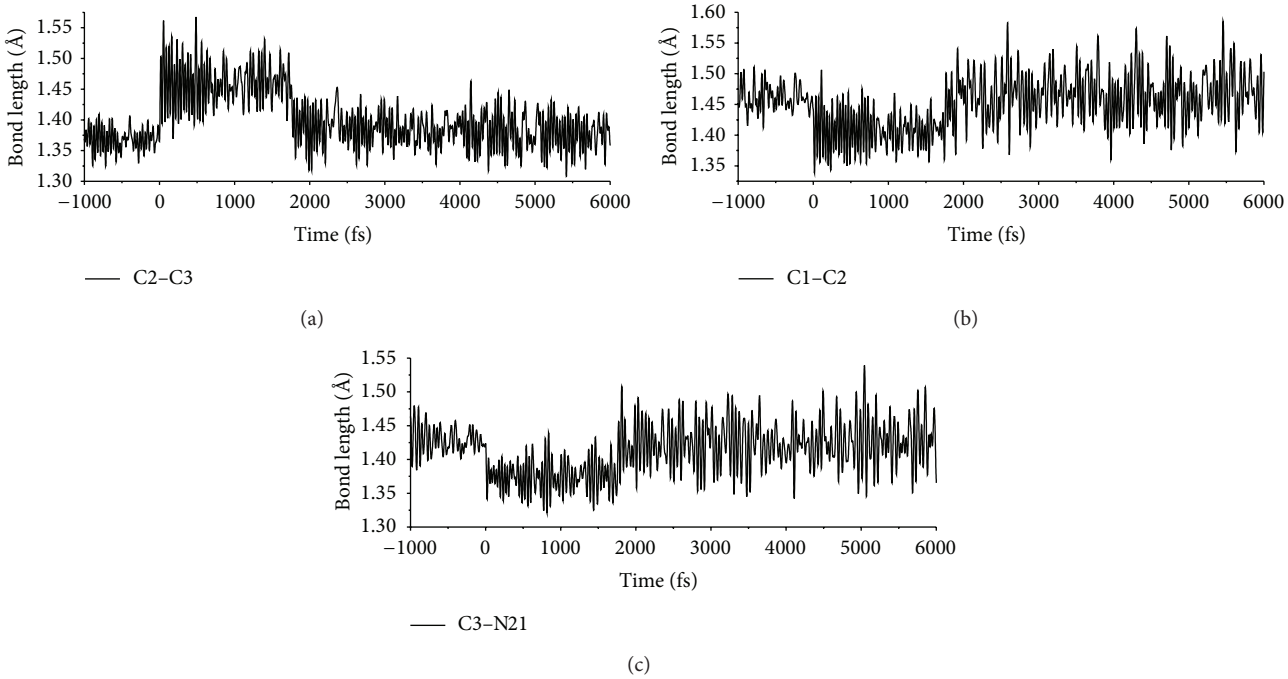

Figure 6: Time dependence in BMH of (a) bond length C2–C3, (b) bond length C1–C2, and (c) bond length C3–N21 for the *trans*-to-*cis* isomerization. All labels are defined in Figure 1.

C2=C3 and C1–C4, respectively, are displayed in Figure 7. As we can see, after the excitation at 0 fs, C3–C6 was also shortened, decreasing from 1.46 Å to 1.43 Å, and returning to 1.46 Å after the deexcitation at 1740 fs. The C1–C4 bond length increases from 1.41 Å to 1.45 Å at 0 fs and comes back to 1.41 Å after 1740 fs.

For the representative *trans*-to-*cis* isomerization of BMH discussed above, lifetime of the S_1 excited state in

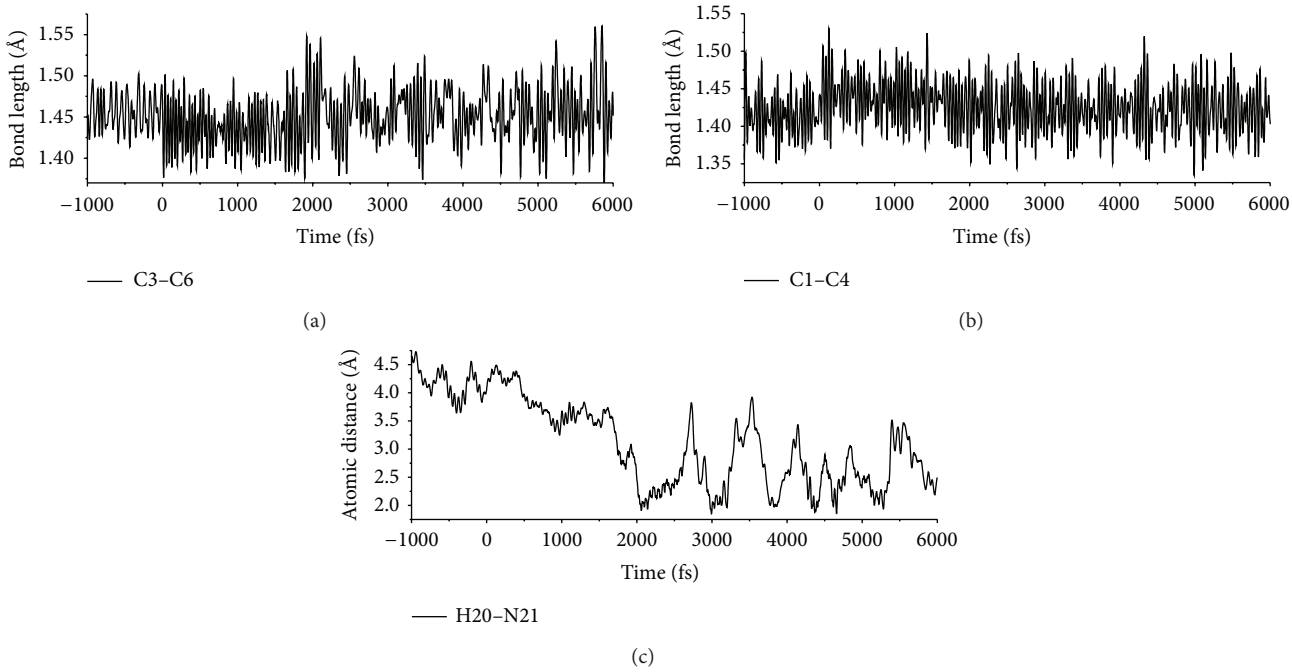

Figure 7: Time dependence in BMH of (a) bond length C3–C6, (b) bond length C1–C4, and (c) atomic distance H20–N21 for the *trans*-to-*cis* isomerization. All labels are defined in Figure 1.

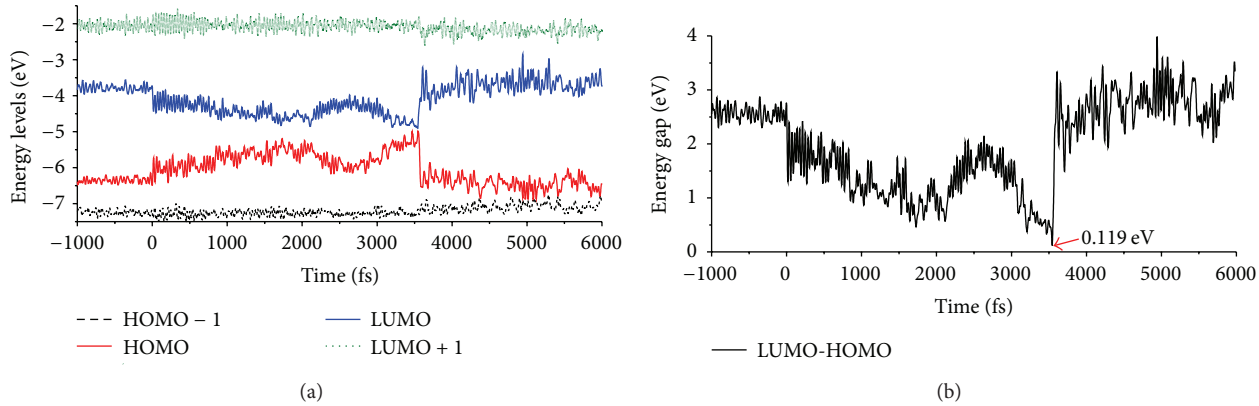

Figure 8: (a) Orbital energies from HOMO − 1 to LUMO + 1 and (b) LUMO-HOMO energy gap in BMH as a function of time for the *cis*-to-*trans* isomerization.

trans-BMH is about 1740 fs, while the *cis* geometry is arrived in about 2040 fs. Rotation around C2=C3 bond is the dominant reaction mechanism. Deexcitation occurs near the midpoint of the rotation, due to an avoided crossing near the S_1/S_0 conical intersection.

3.2. cis-to-trans Photoisomerization of BMH. On the basis of 60 simulations, 20 of which did produce *cis*-to-*trans* isomerization, we find a quantum yield of 33% for *cis*-to-*trans* isomerization of BMH induced by the excitation to its S_1 excited state, which is only a little larger than that of *trans*-to-*cis* isomerization of BMH. For the 20 simulations which did produce *cis*-to-*trans* isomerization, the average S_1 lifetime of *cis*-BMH is about 3100 fs. In order to provide the detailed *cis*-to-*trans* reaction mechanism, a single representative simulation with a 3545 fs S_1 lifetime is discussed below.

Time dependence of orbital energies from HOMO − 1 to LUMO + 1 and energy gap between LUMO and HOMO in BMH during the *cis*-to-*trans* photoisomerization are shown in Figure 8. For comparison, the results of ortibal energies and LUMO-HOMO energy gap before the excitation are also displayed in this figure. As we can see, after the excitation at 0 fs, only HOMO and LUMO energies are strongly affected by the nuclear motion. The LUMO-HOMO energy gap decreases from 2.7 eV to about 0.5 eV in 2000 fs, increases to about 2.0 eV at about 2500 fs, and decreases again to the minimum value of 0.119 eV in this simulation at 3543 fs. After 3600 fs, the LUMO-HOMO energy gap increases to about

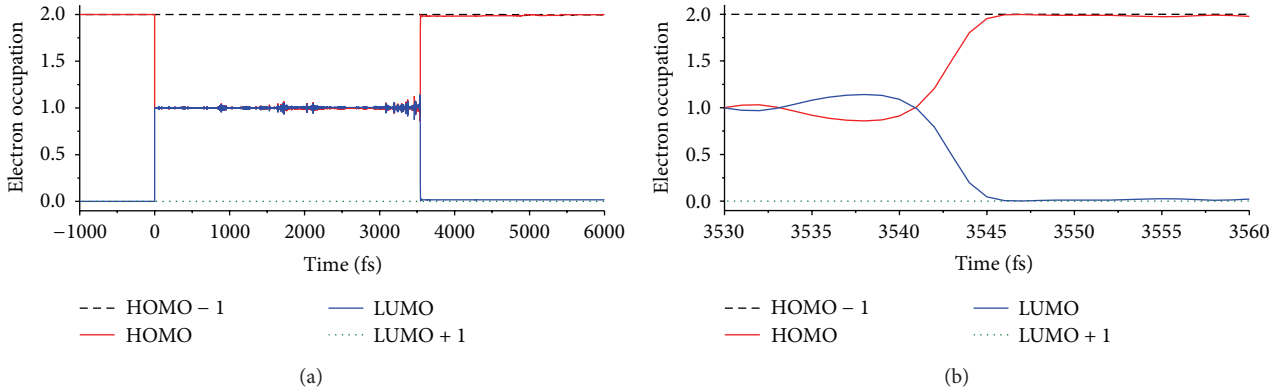

Figure 9: (a) Electron occupancies in BMH from HOMO − 1 to LUMO + 1 for the *cis*-to-*trans* isomerization. (b) Details of Figure 9(a) from 3530 to 3560 fs.

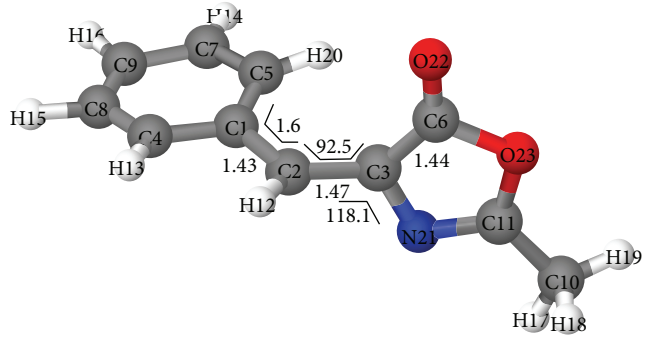

Figure 10: Geometry of BMH at 3543 fs in our *cis*-to-*trans* isomerization simulation, which is near a S_1/S_0 conical intersection. Bond lengths are in angstroms, and bond angles and dihedral angles are in degrees.

2.7 eV and vibrates around this value until the end of this simulation.

Variations of electron occupancies in the orbitals from HOMO − 1 to LUMO + 1 during the *cis*-to-*trans* photoisomerization are displayed in Figure 9. Details of the electron occupancies between 3530 and 3560 fs are also shown in this figure. As we can see, after the excitation at 0 fs, BMH stays in the first excited state until the deexcitation occurring at 3543 fs, which is corresponding to an avoided crossing near the S_1/S_0 conical intersection, as shown in Figure 8.

The geometry of BMH at 3543 fs is displayed in Figure 10. At this point, C1C2C3C6 dihedral angle is equal to 92.5°, near the midpoint of the rotation. Bond length C2=C3 is equal to 1.47 Å, much longer than the ordinary C=C bond length. Other geometrical values, such as bond lengths and bond angles, are also presented in this figure.

Variations of geometry during the *cis*-to-*trans* photoisomerization of BMH are presented in Figures 11–14. Time dependence of three dihedral angles in BMH, C1C2C3C6, C3C2C1C5, and C1C2H12C3, is shown in Figure 11. As shown in this figure, after the excitation at 0 fs, dihedral angle C1C2C3C6 increases from 180° to about 240° in 900 fs, stays around 240° between 900 fs and 2100 fs and then changes the rotation direction, and decreases dramatically from 240° to 0°. When BMH arrives at an avoided crossing near the S_1/S_0 conical intersection at 3543 fs, the value of C1C2C3C6 reaches 92.5°, as shown in Figure 10. C1C2C3C6 arrives at 0° (the optimized C1C2C3C6 value in *trans*-BMH) at 3623 fs and then vibrates around this new value until the end of our simulation. This new C1C2C3C6 value (0°) can be a demonstration that the molecule arrives at its *trans* geometry in about 3623 fs. Atomic distance between H20 and N21 presented in Figure 14(c) can be another confirmation for the final *trans* geometry, which does not vary evidently before 3000 fs but increases continuously from about 2.2 Å to 4.4 Å (the optimized distance between H20 and N21 in *trans*-BMH) in subsequent 600 fs and then vibrates around this value until the end of our simulation. As can be seen in Figure 11(b), dihedral angle C3C2C1C5 stays around 180° before BMH returns to its ground state at 3545 fs. But due to the energy redistribution among the molecule after deexcitation, BMH starts and keeps on rotating around C1–C2 bond until the end of our simulation. Similar results have been found in photoisomerization of stilbene and azobenzene [14, 40]. C1C2H12C3 also does not vary evidently during the whole simulation and keeps on vibrating around 180°, which can demonstrate that H12 atom stays nearly in a plane with atoms C1,C2, and C3 all the time.

Time variations of three bond angles, C1C2C3, C2C1C5, and C2C3N21, are shown in Figure 12. As we can see, C1C2C3 keeps on vibrating around 125° during the whole simulation, while C2C1C5 stays around 120°. For C2C3N21, it vibrates

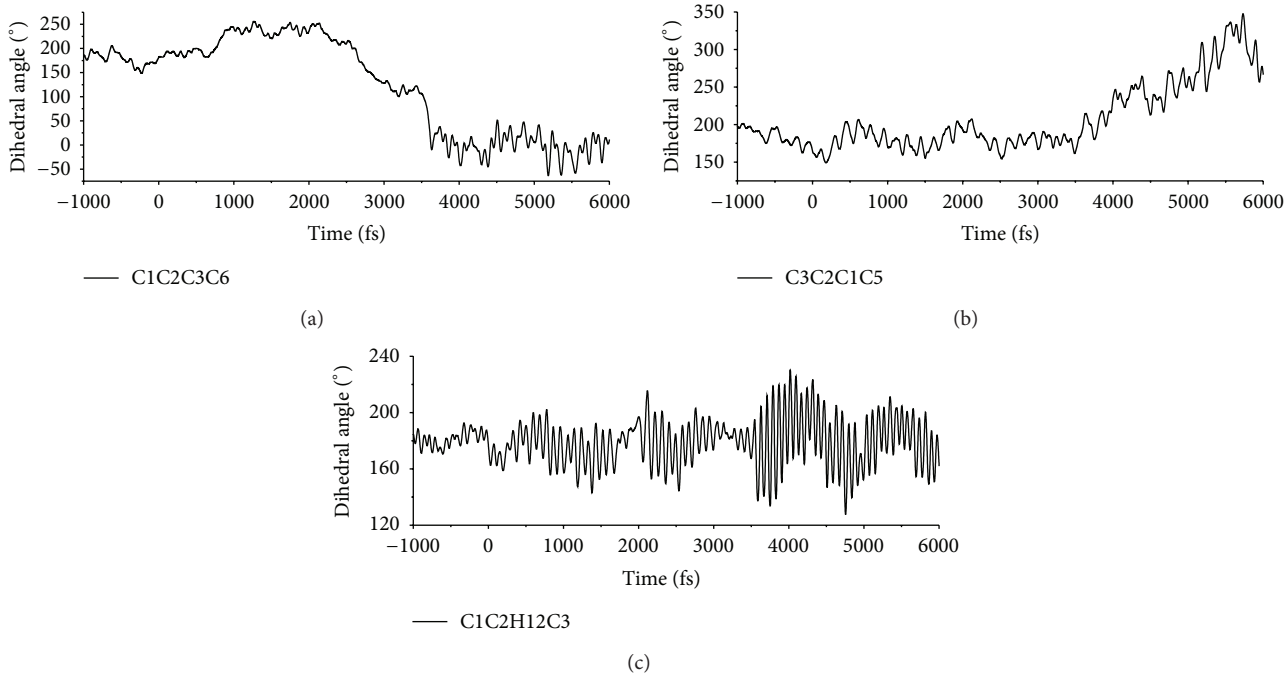

Figure 11: Time dependence in BMH of (a) C1C2C3C6 dihedral angle, (b) C3C2C1C5 dihedral angle, and (c) C1C2H12C3 dihedral angle for the *cis*-to-*trans* isomerization. All labels are defined in Figure 1.

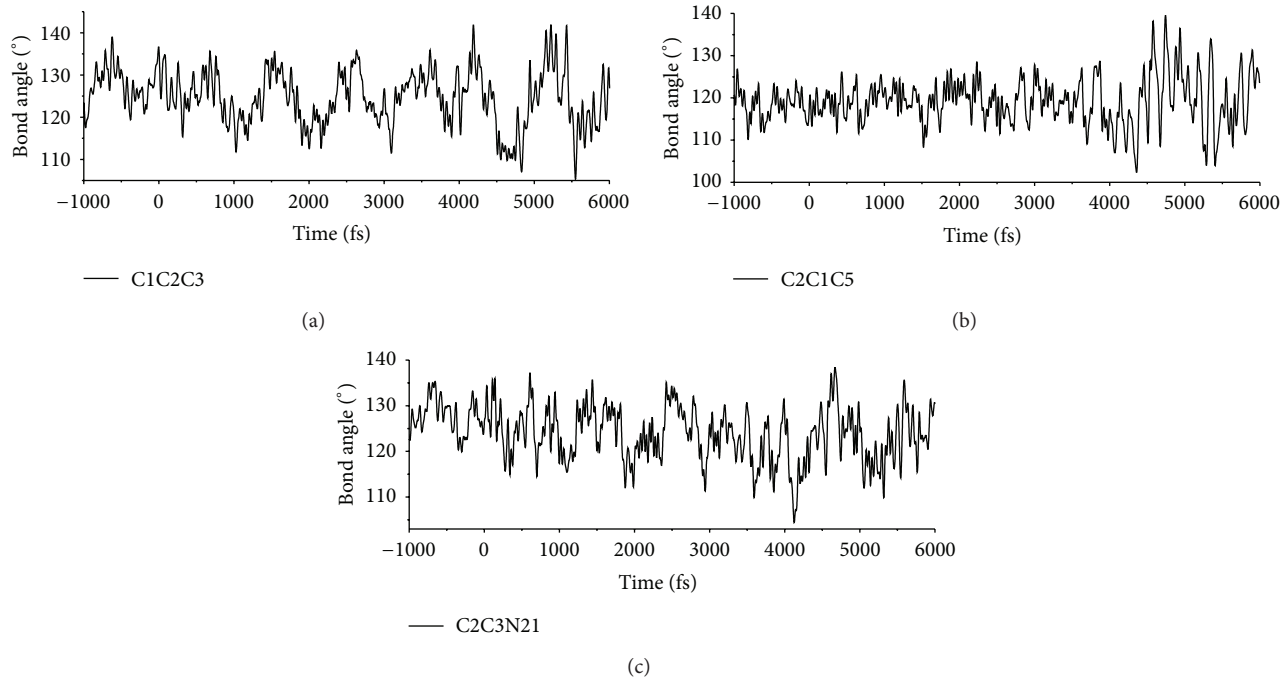

Figure 12: Time dependence in BMH of three bond angles (a) C1C2C3, (b) C2C1C5, and (c) C2C3N21 for the *cis*-to-*trans* isomerization. All labels are defined in Figure 1.

around 128° before the excitation at 0 fs and decreases slowly to about 119° (the optimized value of C2C3N21 in *trans*-BMH) when deexcitation occurs at 3543 fs.

Figure 13 displays the time dependence of three bond lengths in BMH. After the excitation at 0 fs, C2=C3 is weakened, increasing from 1.35 Å to 1.46 Å and returning to 1.35 Å after the deexcitation at 3545 fs. Two other bonds shown in Figures 12(a) and 12(b), on the other hand, are shortened after the excitation at 0 fs. C1–C2 decreases from 1.46 Å to 1.40 Å after 0 fs and goes back to 1.46 Å after 3545 fs.

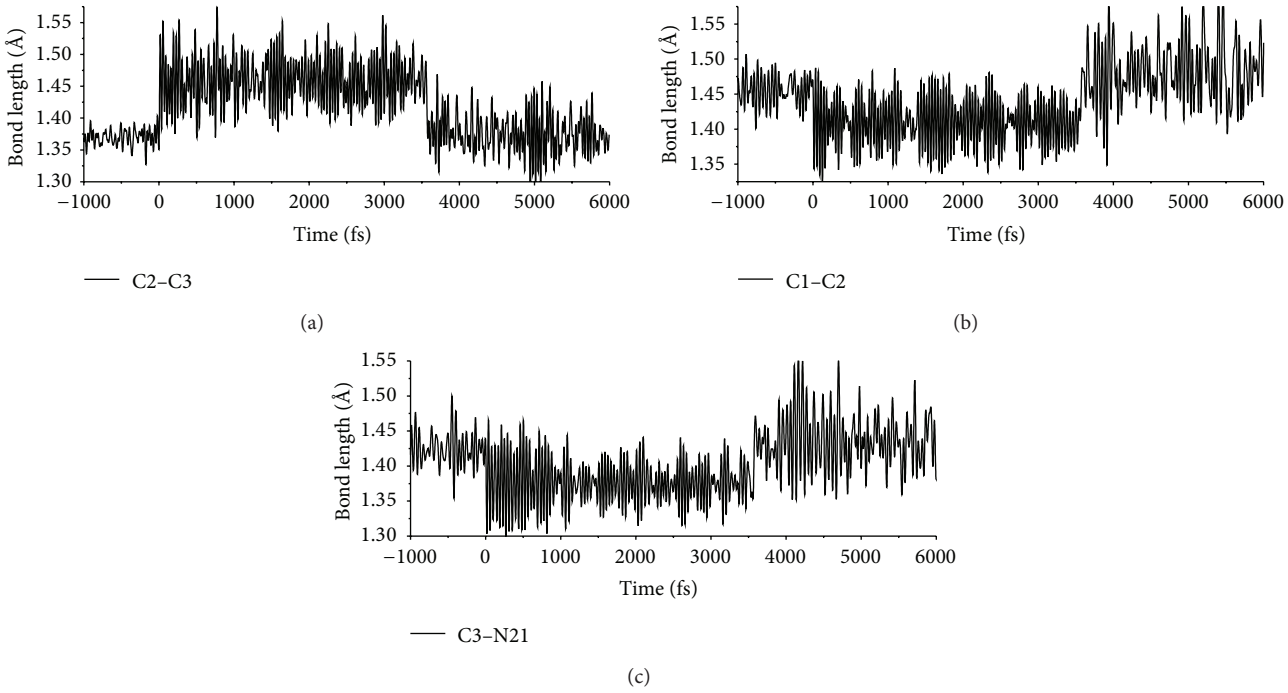

Figure 13: Time dependence in BMH of bond lengths (a) C2–C3, (b) C1–C2, and (c) C3–N21 for the *cis*-to-*trans* isomerization. All labels are defined in Figure 1.

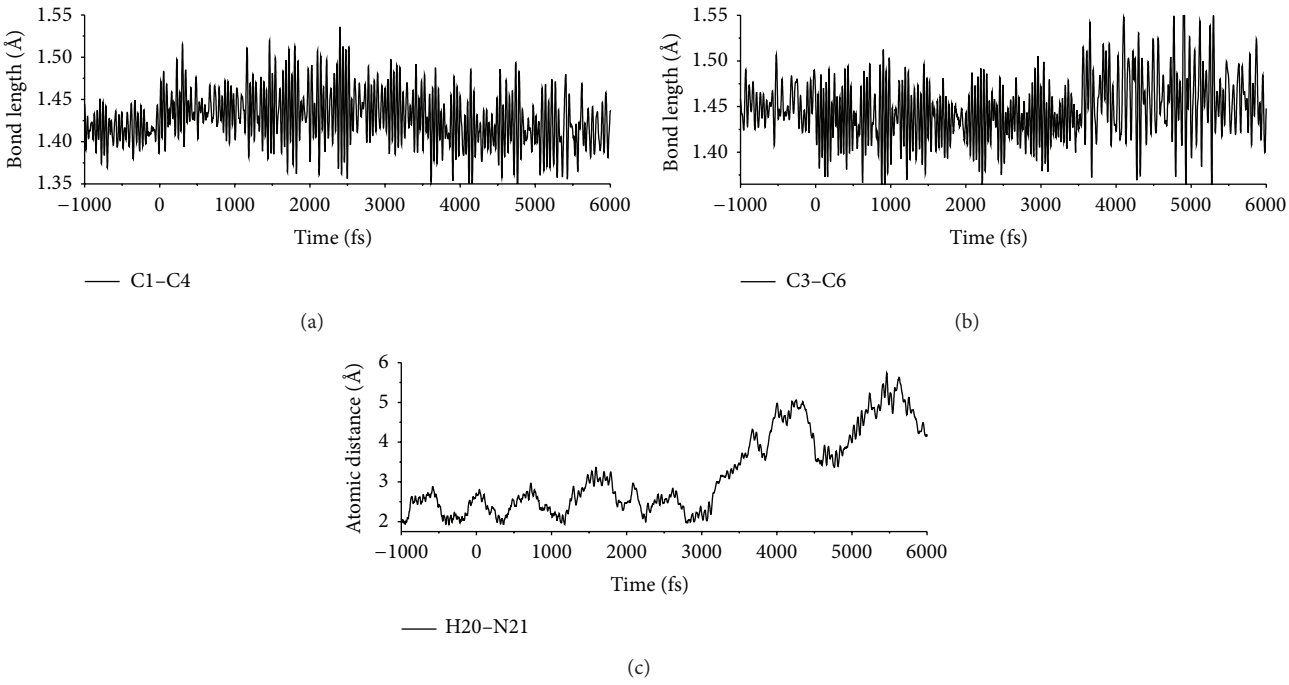

Figure 14: Time dependence in BMH of (a) bond length C3–C6, (b) bond length C1–C4, and (c) atomic distance H20–N21 for the *cis*-to-*trans* isomerization. All labels are defined in Figure 1.

C3-N21 decreases from 1.43 Å to 1.38 Å after the excitation and returns to its initial value after the deexcitation. Bond lengths C1-C4 and C3–C6, as shown in Figure 14, are also affected by the excitation and deexcitation. C1–C4 increases from 1.41 Å to 1.45 Å after 0 fs and returns to its initial value after deexcitation. Bond length of C3–C6 decreases from 1.46 Å to 1.43 Å after the excitation and then returns to its initial value 1.46 Å after the deexcitation at 3545 fs.

4. Conclusions

With density-functional-based nonadiabatic molecular dynamics simulations, *trans*-to-*cis* and *cis*-to-*trans* photoisomerizations of a green fluorescent protein chromophore based molecule 4-benzylidene-2-methyloxazol-5(4H)-one (BMH) induced by the excitation to its S_1 excited state were performed. We find a quantum yield of 32% for the *trans*-to-*cis* photoisomerization of BMH and a quantum yield of 33% for its *cis*-to-*trans* photoisomerization. In those simulations that did produce *trans*-to-*cis* isomerization, the range of calculated S_1 lifetimes was 700–4000 fs, with a mean value of 1450 fs. For the finished *cis*-to-*trans* isomerization, the range of calculated S_1 lifetimes was 1200–7000 fs, with a mean value of 3100 fs. The S_1 lifetime of *cis*-BMH is much larger than that of *trans*-BMH, agreeing well with the experimental result [27].

For the simulation shown in detail, lifetimes of the *trans*-BMH and *cis*-BMH are 1740 fs and 3545 fs, respectively. The whole *trans*-to-*cis* isomerization is finished in about 2040 fs, while whole time needed for *cis*-to-*trans* isomerization is about 3623 fs. For both photoisomerizations, rotation around the central C2=C3 bond is the dominant reaction mechanism; deexcitation occurs at an avoided crossing near the S_1/S_0 conical intersection, which is near the midpoint of the rotation.

Conflict of Interests

The authors declare that there is no conflict of interests regarding the publication of this paper.

Acknowledgments

This work was supported by the Natural Science Foundation of China (Grants 21203144, 11074199, and 11174233), Doctoral Fund of Ministry of Education of China (Grant 20120201120056), and the Fundamental Research Funds for the Central Universities.

References

[1] D. H. Waldeck, "Photoisomerization dynamics of stilbenes," *Chemical Reviews*, vol. 91, no. 3, pp. 415–438, 1991.

[2] T. Baumert, T. Frohnmeyer, B. Kiefer et al., "Femtosecond transition state dynamics of cis-stilbene," *Applied Physics B: Lasers and Optics*, vol. 72, no. 1, pp. 105–108, 2001.

[3] W. Fuß, C. Kosmidis, W. E. Schmid, and S. A. Trushin, "The photochemical cis-trans isomerization of free stilbene molecules follows a hula-twist pathway," *Angewandte Chemie*, vol. 43, no. 32, pp. 4178–4182, 2004.

[4] Y. Ishibashi, M. Murakami, H. Miyasaka, S. Kobatake, M. Irie, and Y. Yokoyama, "Laser multiphoton-gated photochromic reaction of a fulgide derivative," *Journal of Physical Chemistry C*, vol. 111, no. 6, pp. 2730–2737, 2007.

[5] T. Cordes, S. Malkmus, J. A. DiGirolamo et al., "Accelerated and efficient photochemistry from higher excited electronic states in fulgide molecules," *The Journal of Physical Chemistry A*, vol. 112, no. 51, pp. 13364–13371, 2008.

[6] F. Renth, R. Siewertsen, and F. Temps, "Enhanced photoswitching and ultrafast dynamics in structurally modified photochromic fulgides," *International Reviews in Physical Chemistry*, vol. 32, no. 1, pp. 1–38, 2013.

[7] M. Takeshita and M. Irie, "Photoresponsive tweezers for alkali metal ions. Photochromic diarylethenes having two crown ether moieties," *Journal of Organic Chemistry*, vol. 63, no. 19, pp. 6643–6649, 1998.

[8] S. F. Yan, V. N. Belov, M. L. Bossi, and S. W. Hell, "Switchable fluorescent and solvatochromic molecular probes based on 4-amino-N-methylphthalimide and a photochromic diarylethene," *European Journal of Organic Chemistry*, vol. 2008, no. 15, pp. 2531–2538, 2008.

[9] Y. Li and Q. Li, "Photochemically reversible and thermally stable axially chiral diarylethene switches," *Organic Letters*, vol. 14, no. 17, pp. 4362–4365, 2012.

[10] I. K. Lednev, T.-Q. Ye, L. C. Abbott, R. E. Hester, and J. N. Moore, "Photoisomerization of a capped azobenzene in solution probed by ultrafast time-resolved electronic absorption spectroscopy," *The Journal of Physical Chemistry A*, vol. 102, no. 46, pp. 9161–9166, 1998.

[11] T. Fujino and T. Tahara, "Picosecond time-resolved Raman study of trans-azobenzene," *Journal of Physical Chemistry A*, vol. 104, no. 18, pp. 4203–4210, 2000.

[12] H. Satzger, S. Spörlein, C. Root, J. Wachtveitl, W. Zinth, and P. Gilch, "Fluorescence spectra of trans- and cis-azobenzene: emission from the Franck-Condon state," *Chemical Physics Letters*, vol. 372, no. 1-2, pp. 216–223, 2003.

[13] I. Conti, M. Garavelli, and G. Orlandi, "The different photoisomerization efficiency of azobenzene in the lowest $n\pi^*$ and $\pi\pi^*$ singlets: the role of a phantom state," *Journal of the American Chemical Society*, vol. 130, no. 15, pp. 5216–5230, 2008.

[14] C.-W. Jiang, R.-H. Xie, F.-L. Li, and R. E. Allen, "Comparative studies of the trans—Cis photoisomerizations of azobenzene and a bridged azobenzene," *Journal of Physical Chemistry A*, vol. 115, no. 3, pp. 244–249, 2011.

[15] H.-H. Liu, X. Zhang, Z. Gao, and Y. Chen, "Photoconversion of a protonated diarylethene derivative," *Journal of Physical Chemistry A*, vol. 116, no. 40, pp. 9900–9903, 2012.

[16] G. Haberhauer and C. Kaliweit, "A bridged azobenzene derivative as a reversible, light-induced chirality switch," *Angewandte Chemie*, vol. 49, no. 13, pp. 2418–2421, 2010.

[17] I. K. Lednev, T.-Q. Ye, P. Matousek et al., "Femtosecond time-resolved UV-visible absorption spectroscopy of trans-azobenzene: dependence on excitation wavelength," *Chemical Physics Letters*, vol. 290, no. 1–3, pp. 68–74, 1998.

[18] T. Pancur, F. Renth, F. Temps et al., "Femtosecond fluorescence up-conversion spectroscopy of a rotation-restricted azobenzene after excitation to the S1 state," *Physical Chemistry Chemical Physics*, vol. 7, no. 9, pp. 1985–1989, 2005.

[19] R. Siewertsen, H. Neumann, B. Buchheim-Stehn et al., "Highly efficient reversible Z-E photoisomerization of a bridged azobenzene with visible light through resolved S1(npi∗) absorption bands," *Journal of the American Chemical Society*, vol. 131, no. 43, pp. 15594–15595, 2009.

[20] M. Chalfie, Y. Tu, G. Euskirchen, W. W. Ward, and D. C. Prasher, "Green fluorescent protein as a marker for gene expression," *Science*, vol. 263, no. 5148, pp. 802–805, 1994.

[21] V. Voliani, R. Bizzarri, R. Nifosì et al., "*Cis-trans* photoisomerization of fluorescent-protein chromophores," *The Journal of Physical Chemistry B*, vol. 112, no. 34, pp. 10714–10722, 2008.

[22] S. Rafiq, B. K. Rajbongshi, N. N. Nair, P. Sen, and G. Ramanathan, "Excited state relaxation dynamics of model green fluorescent protein chromophore analogs: Evidence for cis-trans isomerism," *Journal of Physical Chemistry A*, vol. 115, no. 47, pp. 13733–13742, 2011.

[23] J.-S. Yang, G.-J. Huang, Y.-H. Liu, and S.-M. Peng, "Photoisomerization of the green fluorescence protein chromophore and the meta- and para-amino analogues," *Chemical Communications*, vol. 2008, no. 11, pp. 1344–1346, 2008.

[24] P. Naumov, J. Kowalik, K. M. Solntsev et al., "Topochemistry and photomechanical effects in crystals of green fluorescent protein-like chromophores: Effects of hydrogen bonding and crystal packing," *Journal of the American Chemical Society*, vol. 132, no. 16, pp. 5845–5857, 2010.

[25] X. He, A. F. Bell, and P. J. Tonge, "Synthesis and spectroscopic studies of model red fluorescent protein chromophores," *Organic Letters*, vol. 4, no. 9, pp. 1523–1526, 2002.

[26] A. Kikuchi, E. Fukumura, S. Karasawa, H. Mizuno, A. Miyawaki, and Y. Shiro, "Structural characterization of a thiazoline-containing chromophore in an orange fluorescent protein, monomeric kusabira orange," *Biochemistry*, vol. 47, no. 44, pp. 11573–11580, 2008.

[27] M. Blanco-Lomas, P. J. Campos, and D. Sampedro, "Benzylidene-oxazolones as molecular photoswitches," *Organic Letters*, vol. 14, no. 17, pp. 4334–4337, 2012.

[28] Y. Dou, B. R. Torralva, and R. E. Allen, "Semiclassical electron-radiation-ion dynamics (SERID) and cis-trans photoisomerization of butadiene," *Journal of Modern Optics*, vol. 50, no. 15–17, pp. 2615–2643, 2003.

[29] R. E. Allen, T. Dumitrica, and B. Torralva, "Electronic and structural response of materials to fast intense laser pulses," in *Ultrafast Physical Processes in Semiconductors*, K. T. Tsen, Ed., chapter 7, Academic Press, New York, NY, USA, 2001.

[30] R. E. Allen, "Electron-ion dynamics: a technique for simulating both electronic transitions and ionic motion in molecules and materials," *Physical Review B*, vol. 50, no. 24, pp. 18629–18632, 1994.

[31] R. E. Allen, "Coupling of electrons to the electromagnetic field in a localized basis," *Physical Review B*, vol. 78, no. 6, Article ID 064305, 2008.

[32] R. E. Allen, T. Dumitrică, and B. Torralva, *Ultrafast Physical Processes in Semiconductors*, chapter 7, Academic Press, New York, NY, USA, 2001, edited by K. T. Tsen.

[33] D. Porezag, T. Frauenheim, T. Köhler, G. Seifert, and R. Kaschner, "Construction of tight-binding-like potentials on the basis of density-functional theory: application to carbon," *Physical Review B*, vol. 51, no. 19, pp. 12947–12957, 1995.

[34] G. Seifert, D. Porezag, and T. Frauenheim, "Calculations of molecules, clusters, and solids with a simplified LCAO-DFT-LDA scheme," *International Journal of Quantum Chemistry*, vol. 58, no. 2, pp. 185–192, 1996.

[35] Y. Dou and R. E. Allen, "Detailed dynamics of a complex photochemical reaction: Cis-trans photoisomerization of stilbene," *The Journal of Chemical Physics*, vol. 119, no. 20, pp. 10658–10666, 2003.

[36] Y. Dou, B. R. Torralva, and R. E. Allen, "Interplay of electronic and nuclear degrees of freedom in a femtosecond-scale photochemical reaction," *Chemical Physics Letters*, vol. 392, no. 4–6, pp. 352–357, 2004.

[37] P. Sauer and R. E. Allen, "Dynamics of the photoinduced ring-opening of stilbene, a prototypical diarylethene," *Chemical Physics Letters*, vol. 434, no. 4-6, pp. 260–264, 2007.

[38] P. Sauer and R. E. Allen, "Influence of laser pulse parameters on dynamical processes during azobenzene photoisomerization," *Journal of Physical Chemistry A*, vol. 112, no. 44, pp. 11142–11152, 2008.

[39] C.-W. Jiang, R.-H. Xie, F.-L. Li, and R. E. Allen, "Photocyclization of trans-stilbene induced by an ultrafast laser pulse," *Chemical Physics Letters*, vol. 487, no. 4–6, pp. 177–182, 2010.

[40] C. Jiang, R. Xie, F. Li, and R. E. Allen, "Trans-to-cis isomerization of stilbene following an ultrafast laser pulse," *Chemical Physics Letters*, vol. 474, no. 4–6, pp. 263–267, 2009.

[41] C.-W. Jiang, R.-H. Xie, F.-L. Li, and R. E. Allen, "Ultrafast cis-to-trans photoisomerization of a bridged azobenzene through $n\pi$ excitation: rotational pathway is not restricted," *Chemical Physics Letters*, vol. 521, pp. 107–112, 2012.

[42] Y. Dou, Y. Lei, A. Li et al., "Detailed dynamics of the photodissociation of cyclobutane," *The Journal of Physical Chemistry A*, vol. 111, no. 6, pp. 1133–1137, 2007.

[43] W. Zhang, S. Yuan, A. Li, Y. Dou, J. Zhao, and W. Fang, "Photoinduced thymine dimerization studied by semiclassical dynamics simulation," *Journal of Physical Chemistry C*, vol. 114, no. 12, pp. 5594–5601, 2010.

[44] S. Yuan, W. Zhang, L. Liu, Y. Dou, W. Fang, and G. V. Lo, "Detailed mechanism for photoinduced cytosine dimerization: a semiclassical dynamics simulation," *Journal of Physical Chemistry A*, vol. 115, no. 46, pp. 13291–13297, 2011.

[45] E. Teller, "The crossing of potential surfaces," *The Journal of Physical Chemistry*, vol. 41, no. 1, pp. 109–116, 1937.

[46] M. Baer, *Beyond Born-Oppenheimer: Electronic Nonadiabatic Coupling Terms and Conical Intersections*, Wiley-Interscience, Hoboken, NJ, USA, 2006.

[47] C. Nonnenberg, H. Gaub, and I. Frank, "First-principles simulation of the photoreaction of a capped azobenzene: the rotational pathway is feasible," *ChemPhysChem*, vol. 7, no. 7, pp. 1455–1461, 2006.

[48] Y. Norikane and N. Tamaoki, "Photochemical and thermal cis/trans isomerization of cyclic and noncyclic azobenzene dimers: effect of a cyclic structure on isomerization," *European Journal of Organic Chemistry*, no. 5, pp. 1296–1302, 2006.

[49] M. J. Frisch, G. W. Trucks, H. B. Schlegel et al., GAUSSIAN, Inc., Wallingford, CT, 2004.

Hindawi Publishing Corporation
International Journal of Photoenergy
Volume 2014, Article ID 158523, 9 pages
http://dx.doi.org/10.1155/2014/158523

Research Article

Competing Deactivation Channels for Excited π-Stacked Cytosines

Shuai Yuan,[1] Huiling Hong,[1] Gang Wang,[1] Wenying Zhang,[1] Yusheng Dou,[1,2] and Glenn V. Lo[2]

[1] *College of Bio-information, Chongqing University of Posts and Telecommunications, Chongqing 400065, China*
[2] *Department of Physical Sciences, Nicholls State University, P.O. Box 2022, Thibodaux, LA 70310, USA*

Correspondence should be addressed to Yusheng Dou; yusheng.dou@nicholls.edu

Received 13 April 2014; Accepted 30 May 2014; Published 3 August 2014

Academic Editor: Fuli Li

The deactivation of π-stacked cytosine molecules following excitation by ultrashort laser pulses was studied using semiclassical dynamics simulations. Another deactivation channel was found to compete with a previously reported path that led to dimerization. For both pathways, the initial excited state was found to form a charge-separated neutral exciton state, which forms an excimer state by charge transfer. When the interbase distance becomes less than 3 Å, charge recombination occurs due to strong intermolecular interaction, ultimately leading to an avoided crossing. Results indicate that the C_2–N_1–C_6–C_5 and C_2'–N_1'–C_6'–C_5' dihedral angles play a significant role in the vibronic coupling between the highest occupied molecular orbital (HOMO) and the lowest unoccupied molecular orbital (LUMO). Vibrational energy distribution determines the fate of the excimer at the avoided crossing. Higher-amplitude vibration of C_5 or C_6 atoms leads to a nonadiabatic transition to the electronic ground state (a photophysical pathway); otherwise, a chemical reaction leading to the formation of cyclobutane type dimer occurs as found in earlier studies. The S_1 and S_0 potential energy surfaces calculated at TD-DFT level and the simulated trajectories were found to be consistent with CASPT2 results.

1. Introduction

Electronic excitation of DNA nucleobases induced by solar ultraviolet light has been extensively studied since the 1960s because it can lead to the formation of harmful photoproducts such as cyclobutane pyrimidine dimers (CPDs) between adjacent pyrimidine bases within the same DNA strand [1–3]. The formation of CPDs is considered as the main cause of cell death, mutagenesis, and development of skin cancers [4]. However, the quantum yield of photolesion formation is very low, suggesting a highly efficient nonradiative deactivation of excited DNA to the ground state consistent with the photostability of nucleobases [3].

Electronically excited single nucleobases decay to the ground state primarily by ultrafast internal conversion in less than 1 picosecond. However, in oligo- and polynucleotides the decay of excited nucleobases is more complicated, (showing multiexponential processes with different time constants [5–14]) because of interbase interactions, including base stacking and base pairing, and base-solvent interactions [15–18]. Longer-time decay observed in single-stranded oligonucleotides, where base paring is absent, is attributed to an intrastrand excimer/exciplex state resulting from π-stacking of two adjacent nucleobases [13, 19–24].

The formation of a delocalized excimer state slows down ultrafast nonradiative decay [19–24]. The *ab initio* calculations at CASPT2/CASSCF level [25] for two stacked adenines of different arrangements favor a mechanism involving two possible decay pathways. In this mechanism, unstacked or poorly stacked pairs of bases relax to the ground state by an ultrafast internal conversion through the conical intersection (CI) between the lowest excited state and ground state of the monomer. On the other hand, an excimer state formed between intrastrand stacked bases exhibits a longer decay time to the ground state because of an energy barrier along the path toward the CI of the monomer. It has been suggested

[23] that the excimer state has a charge-transfer character and the state lifetime is correlated with the energy required to transfer an electron from one base to its stacked neighbor.

The formation of excimers is important not only to understand the distinct photophysics of oligonucleotides and DNA but also to account for the intrinsic and distinct photoinduced reaction of cytosine and thymine, which form CPDs. It has been proposed [14] that the singlet excimer state is a precursor to the photodimerization of DNA bases and the excited state dimerization reaction occurs in competition with an internal conversion to the electronic ground state of nucleobases. A recent theoretical calculation [26, 27] for cytosine photodimer formation at the CASSCF/CASPT2 level suggests that the nonadiabatic photodimerization of two stacked cytosine molecules proceeds through a CI involving the lowest singlet excited state and the ground state. This conical intersection, $(S_1/S_0)_{CI}$, occurs below the energy of excimer $^1(C{*}C)$. In order to reach $(S_1/S_0)_{CI}$ from $^1(C{*}C)$, the system has to surmount an energy barrier of about 0.2 eV. The formation of the stable excimer along the lowest singlet excited-state for stacked cytosine molecules may make the formation of cyclobutane cytosine dimer (C⟨⟩C) less efficient compared to the formation of cyclobutane thymine dimer (T⟨⟩T) from a stacked pair of thymine molecules, which do not form a stable excimer. For the latter, the favored mechanism involves a barrierless nonadiabatic mechanism for the photodimerization along a singlet excited-state through a $(S_1/S_0)_{CI}$, which is the funnel for ultrafast nonadiabatic decay leading the formation of cyclobutane thymine dimer (T⟨⟩T). The $(S_1/S_0)_{CI}$ leads to two possible processes of ultrafast internal conversion to the ground state. One pathway involves essentially a chemical change (dimerization), the other (photophysical) leads to two separated monomer bases.

In this paper we present a semiclassical dynamics simulation study for the laser-induced excitation and deactivation of two π-stacked cytosine molecules. The simulation results provide detailed information on the dynamics from photon excitation to deactivation and are expected to be helpful in understanding this process.

2. Methodology

The SERID method is used to carry out dynamics simulations. This technique is described in detail elsewhere [28, 29]. In this methodology, the valence electrons are calculated by the time-dependent Schrödinger equation while both the radiation field and the motion of the nuclei are treated classically. The one-electron states are obtained for each time step by solving the time-dependent Schrödinger equation in a nonorthogonal basis:

$$i\hbar\frac{\partial\Psi_j}{\partial t} = \mathbf{S}^{-1}\cdot\mathbf{H}\cdot\Psi_j, \tag{1}$$

where $\mathbf{S}$ is the overlap matrix of the atomic orbitals. The laser pulse is characterized by the vector potential $\mathbf{A}$, which is coupled to the Hamiltonian via the time-dependent Peierls substitution [30]. Consider

$$\mathbf{H}_{ab}\left(X-X'\right) = \mathbf{H}^0_{ab}\left(X-X'\right)\exp\left\{\frac{iq}{\hbar c}\mathbf{A}\cdot\left(X-X'\right)\right\}, \tag{2}$$

where $\mathbf{H}_{ab}(X-X')$ is the Hamiltonian matrix element for basis functions a and b on atoms at X and X', respectively, and $q=-e$ is the charge of the electron.

In SERID, forces acting on nuclei or ions are computed by the Ehrenfest equation:

$$M_l\frac{d^2X_{l\alpha}}{dt^2} = -\frac{1}{2}\sum_j\Psi_j^+\cdot\left\{\frac{\partial\mathbf{H}}{\partial X_{l\alpha}} - i\hbar\frac{\partial\mathbf{S}}{\partial X_{l\alpha}}\cdot\frac{\partial}{\partial t}\right\}\cdot\Psi_j - \frac{\partial U_{\text{rep}}}{\partial X_{l\alpha}}, \tag{3}$$

where U_{rep} is effective nuclear-nuclear repulsive potential and $X_{l\alpha} = \langle\widehat{X}_{l\alpha}\rangle$ is the expectation value of the time-dependent Heisenberg operator for the α coordinate of the nucleus labeled by l (with $\alpha = x, y, z$). Equation (3) is obtained by neglecting the second and higher order terms of the quantum fluctuations $\widehat{X} - \langle\widehat{X}_{l\alpha}\rangle$ in the exact Ehrenfest theorem.

The time-dependent Schrödinger equation (1) is solved by using a unitary algorithm obtained from the equation for the time evolution operator [31]. Equation (3) is numerically integrated with the velocity Verlet algorithm. A time step of 0.05 femtoseconds is used for this study and energy conservation was then found to hold better than 1 part in 10^6 in a one picosecond simulation at 298 K.

The present "Ehrenfest" principle is complementary to other methods based on different approximations, such as the full multiple spawning model developed by the Martínez group [32]. The limitation of this method is that the simulation trajectory moves along a path dominated by averaging over all the terms in the Born-Oppenheimer expansion:

$$\Psi^{\text{total}}\left(X_n, x_e, t\right) = \sum_i\Psi_i^n\left(X_n, t\right)\Psi_i^e\left(x_e, t\right), \tag{4}$$

rather than following the time evolution of a single potential energy surface, which is approximately decoupled from all the others. (Here, X_n and x_e represent the sets of nuclear and electronic coordinates, resp., and the Ψ_i^e are eigenstates of the electronic Hamiltonian at fixed X_n.) The strengths of the present approach include the retention of all of the $3N$ nuclear degrees of freedom and incorporation of both the excitation due to a laser pulse and the subsequent deexcitation at an avoided crossing near a CI.

3. Results and Discussions

In a recent paper [33], we described simulations that suggest the formation of cyclobutane cytosine dimer (C⟨⟩C) from a π-stacked pair of cytosine molecules irradiated by an ultrashort laser pulse (4.1 eV, fluence = 83.62 J·m^{-2}, fwhm = 25 fs). Formation of an exciton intermediate upon excitation, followed by excimer formation, was involved in this dimerization channel. This paper describes another deactivation

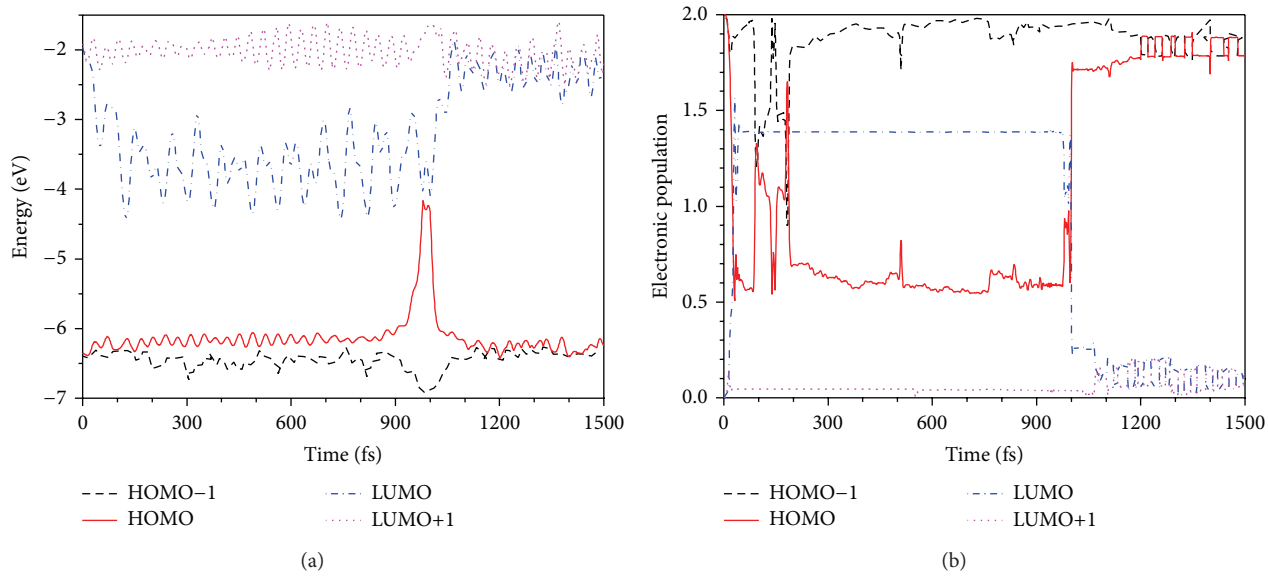

FIGURE 1: (a) The variations with time (b) the time-dependent populations of the HOMO-1, HOMO LUMO, and LUMO+1 energies of two stacked cytosine molecules.

pathway found from additional simulations involving the same initial configuration. A typical trajectory (frequency of 4.1 eV, laser duration of 50 fs and fluence of 77.19 J·m^2) is detailed below.

The variations with time of the HOMO-1, HOMO, LUMO, and LUMO+1 energies and the time-dependent population of these four orbitals are shown in Figures 1(a) and 1(b), respectively. Figure 1(a) shows that there is an abrupt fall in the LUMO energy soon after the application of the laser pulse. An intersection, which named avoided crossing, between the HOMO and LUMO levels is induced by coupling of orbitals, with an energy gap of 0.02 eV, is found at 976 fs. Figure 1(b) shows that by the end of the laser pulse (at 50 fs), about 1.4 electrons are excited from the HOMO to the LUMO, implying electronic excitation of one cytosine molecule. The coupling between the HOMO and LUMO, observed at 976 fs in Figure 1(a), suggests electronic transition from the LUMO to the HOMO. This deexcitation ultimately brings the molecules to the electronic ground state. It can be seen from Figure 1(a) that, shortly after the coupling, both the LUMO and HOMO levels move toward their initial values. After the electronic transition, these two energy levels slightly fluctuate about constants values which are essentially the same as their initial values. The excited state lifetime of 920 fs is about 3~4 times that which is for nonadiabatic deactivation of cytosine monomer [34] and is consistent with dimerization [33].

The variations with time of the lengths of the C_5–C_6, C_5'–C_6', C_5–C_5' and C_6–C_5' bonds are shown in Figure 2. Both C_5–C_6 and C_5'–C_6' are double bonds at the beginning of simulation. Starting at 1.38 Å, which is the length of a typical C–C double bond in a conjugated aromatic system, the C_5–C_6 bond length rapidly elongates to about 1.5 Å after the laser pulse is applied while the C_5'–C_6' bond length remains essentially constant. This suggests excitation of the **C** molecule, but not the **C**′ molecule. After 1000 fs, both C_5–C_6 and C_5'–C_6' bond lengths shorten to their initial values and remain at this length until the end of the simulation. In Figure 2(b), both C_5–C_5' and C_6–C_6' distances are more or less constant up to 600 fs. The C_5–C_5' and C_6–C_6' distances sharply fall at around 700 fs, both reaching a minimum value of 2.0 Å at about 1000 fs. The minima suggest that the C⟨⟩C is not formed in this trajectory. The structures inserted in Figure 2(b) represent the average geometries at different stages of the trajectory. The timescale from 100 to 700 fs is defined as stage I. In this stage, weaker intermolecular interaction is observed because of the relatively large distance (>3 Å) between the **C** and **C**′ molecules. Excitation distorts the **C** molecule (bottom); note that the unexcited molecule (**C**′) remains planar. With the shortening intermolecular distance, the **C**′ molecule deforms as the excimer evolves to stage II (900–1000 fs). After 1000 fs (stage III), the two cytosine molecules move far apart due to deactivation.

Figure 2(a), stage I, shows previously unobserved variations in the C_5–C_6 and C_5'–C_6' bond lengths. The C_5–C_6 bond length shortens from 1.53 Å to 1.48 Å; the C_5'–C_6' bond length stretches from 1.38 Å to 1.42 Å. These variations correlate with intermolecular charge transfer, as seen in Figure 3. Before 100 fs (Figure 3(b)), the relatively flat curve for the net charge on **C** molecule suggests no intermolecular charge transfer. Thereafter, about 1.4 electrons transfer from **C**′ to **C** (Figure 3(a)), after about 900 fs (when interbase distance is 3.1 Å), charge recombination drives electrons back **C**′ and the two molecules return to electrically neutral states at the avoided crossing (976 fs). When electrons migrate to **C**, the increasing electronic density between C_5 and C_6 results in a reduced C_5–C_6 bond length because of the increasing C_5–C_6

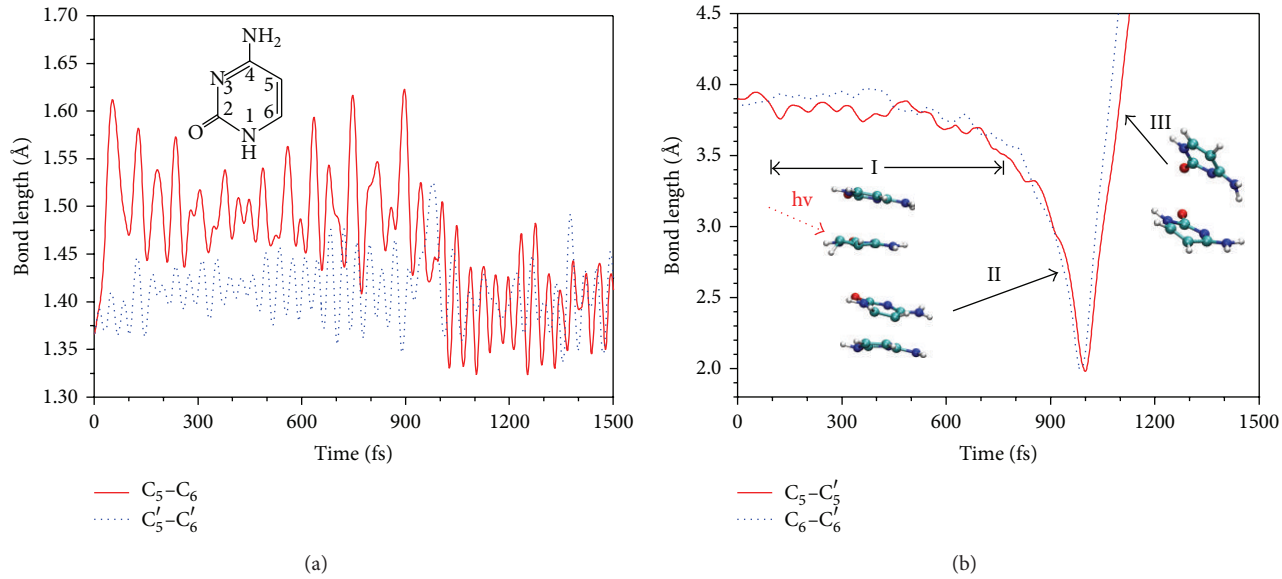

FIGURE 2: (a) The variations with time of the lengths between the C_5 and C_6 atoms and the C'_5 and C'_6 atoms. (b) The variations with time of the lengths between the C_5 and C'_5 atoms and the C_6 and C'_6 atoms in two stacked cytosines molecules.

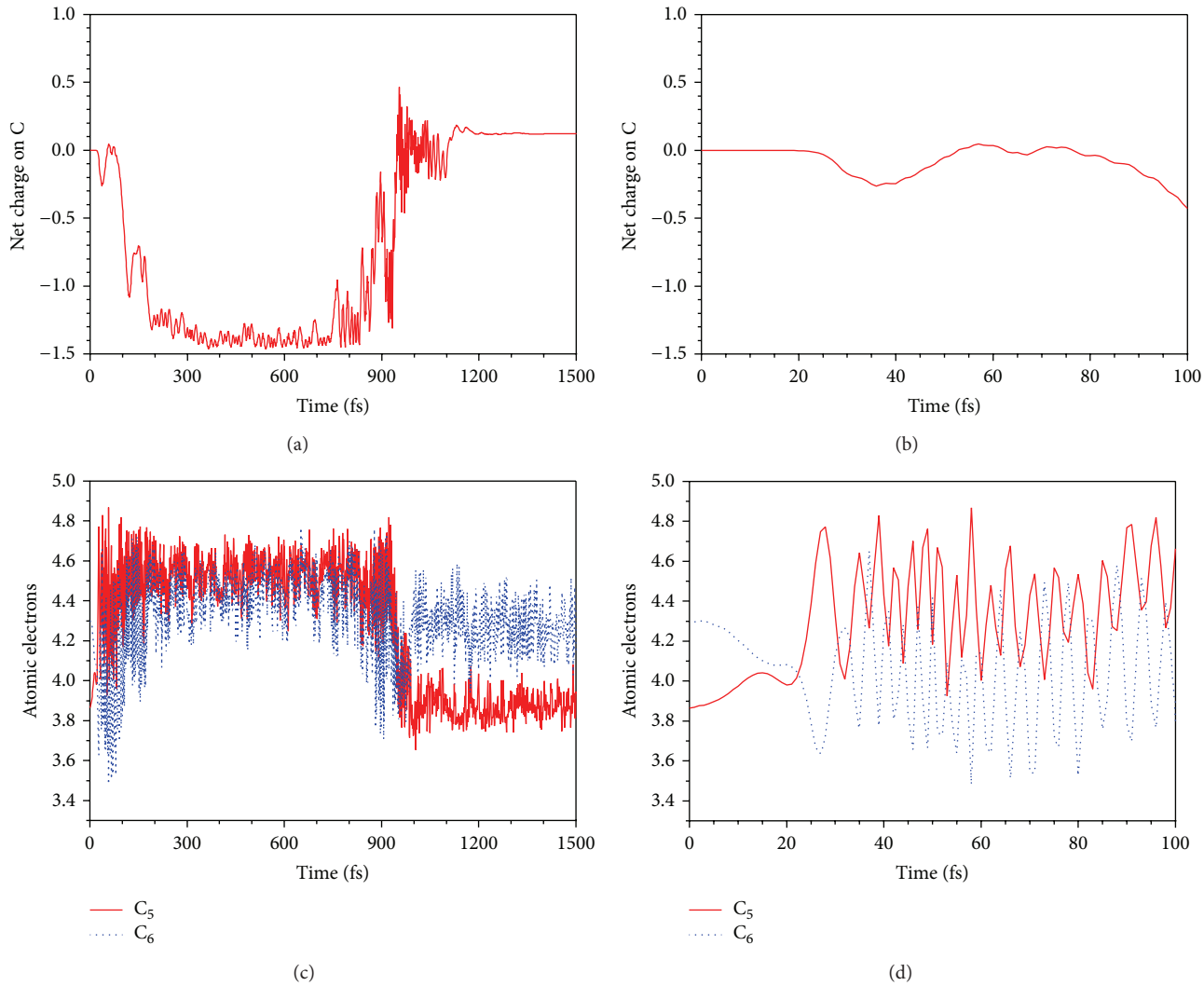

FIGURE 3: Variations with time of the net charge on **C** and the valence electron numbers of C_5 and C_6 atoms.

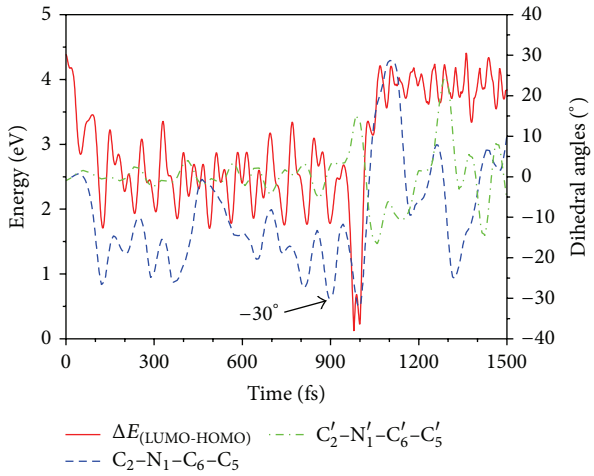

FIGURE 4: Variations with time of the dihedral angles C_2–N_1–C_6–C_5 and C_2'–N_1'–C_6'–C_5' and energy gap between HOMO and LUMO.

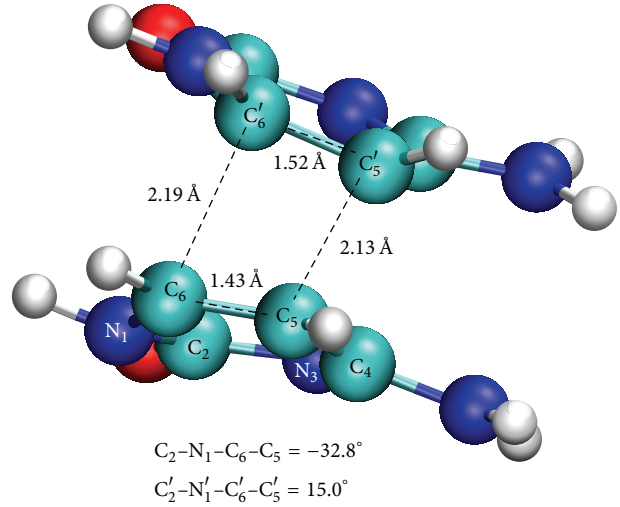

FIGURE 5: Geometries taken from trajectory at time of 976 fs, when avoided crossing occur.

bond order. Conversely, decreasing electronic density in $\mathbf{C}'$ due to the weakening of C_5'–$C_6'\pi$ bond is manifested by an increase in the C_5'–C_6' bond length.

The variations in the valence electrons of the C_5 and C_6 atoms, which are most actively involved in the excitation-deactivation process of pyridines, are also shown in Figure 3; Figure 3(d) zooms in on the 0 to 100 fs region of Figure 3(c). The valence electrons on the atoms are calculated by projection of single electronic wave functions to the orbitals of these atoms. Because of bond polarities due heteroatoms in the aromatic nucleus, valence electrons number of carbon atoms usually fluctuate about the 4 instead of being exactly equal to 4. For example, the valence electrons number of C_5 and C_6 are 4.31 and 3.86, respectively. Excitation by laser results in redistribution of π electrons. Consequently, the covalence number for the C_5 atom drops from 4.31 to 3.9, while increasing to an average of about 4.5 for the C_6 atom during the first 100 fs. Since there is minimal electron transfer between the two cytosine molecules during this time period (Figure 3(b)), this indicates a charge separation within the excited **C** molecule. The charge separated neutral excited state with a lifetime of 100 fs is very similar to the "Frenkel exciton states" [14] formed by the coupling of $^1\pi\pi^*$ states (which are localized on single bases) of proximal nucleobases proposed by Gustavsson and Markovitsi and coworkers [15–18]. According to some experimental and theoretical research [23, 35–37], exciton formation tends to precede the formation of an excimer/exciplex. The shortening of C_5–C_6 and elongation of C_5'–C_6', as shown in Figure 2(a), suggest an exciton state evolving to a charge transfer state (i.e., excimer) after 100 fs.

The variation of dihedral angles, C_2–N_1–C_6–C_5 and C_2'–N_1'–C_6'–C_5', which describe the twisting of the C_5–C_6 and C_5'–C_6' bonds, respectively, is compared to the HOMO-LUMO energy gap in Figure 4. The dihedral C_2–N_1–C_6–C_5 decreases from 0° to −27° within 120 fs, then fluctuates around an average value of −20°. It indicates that the **C** molecule has been deformed due to excitation. Greater

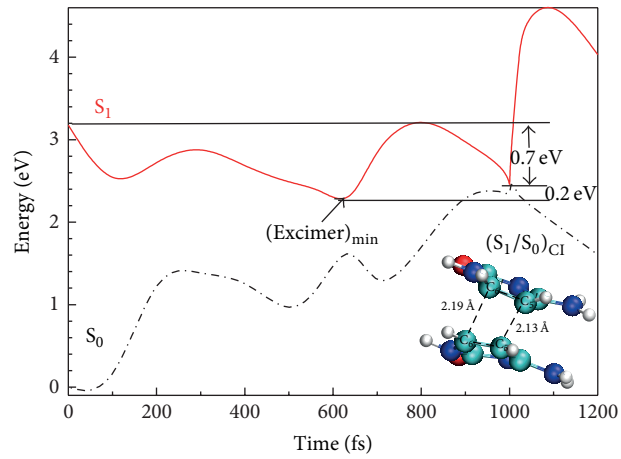

FIGURE 6: PES of stacked cytosines system at Cam-B3LYP/6-311+g* level. Geometry of conical intersection is inserted.

torsion results in a smaller HOMO-LUMO energy gap and a higher electron affinity for **C**, leading to an electron transfer from $\mathbf{C}'$ to **C**. The C_2–N_1–C_6–C_5 angle reaches a maximum of −35° at 986 fs and returns to its initial value after that time. On the other hand, the dihedral C_2'–N_1'–C_6'–C_5' varies little until 900 fs, then sharply rises to 15° at 986 fs. The variation of the C_2'–N_1'–C_6'–C_5' dihedral angle suggests that interbase interaction leads to deformation of $\mathbf{C}'$ after 900 fs. The strong torsion of $\mathbf{C}'$ gives rise to nonadiabatic transition, which leads to the electronic ground state.

The geometry at the avoided crossing is shown in Figure 5. The C_2–N_1–C_6–C_5 and C_2'–N_1'–C_6'–C_5' dihedral angles reach their maximum values at 976 fs. This strong torsion causes a nonadiabatic transition to electronic ground state. For the molecular geometry taken at 976 fs, the C_5–C_5' and C_6–C_6' distances are 2.13 and 2.19 Å, respectively. These compare favorably with 2.27 and 2.17 Å obtained by CASSCF/CASPT2 calculation [26] at the CI between the lowest excited singlet

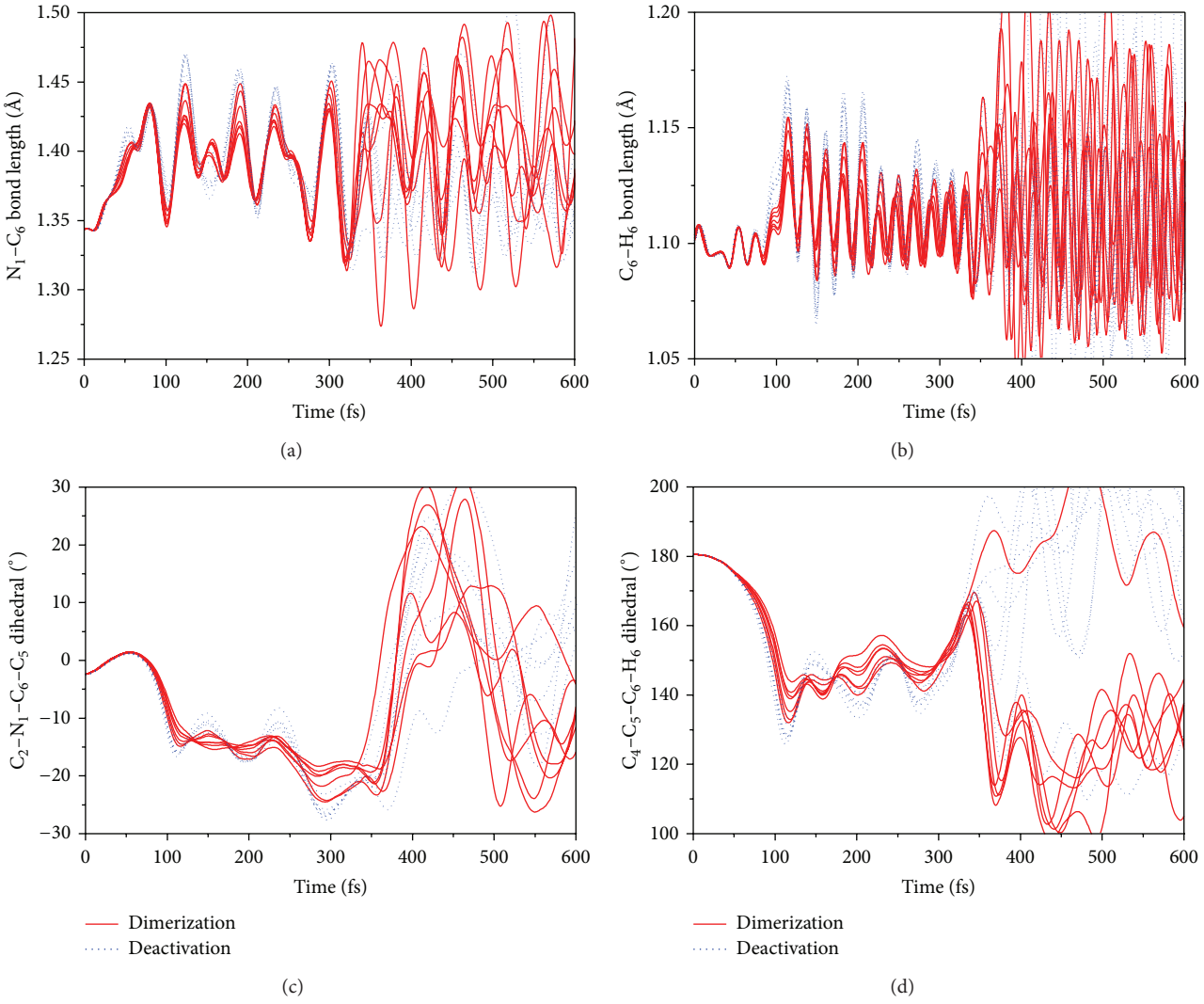

FIGURE 7: The Variations of some degrees of freedom around C_5 and C_6 atoms of dimerization channels and photophysical deactivation channels. The two channels are simplified as "dimer" and "excimer," respectively.

state and the ground state. This indicates that the avoided crossing found at 976 fs is, indeed, in close proximity to the CI. The distances are also very similar to the dimerization channel that we previously reported. We believe that the avoided crossing may be identical for both pathways.

It is worth noting that the average interbase distance is 3 Å at 900 fs as the C_2'–N_1'–C_6'–C_5' dihedral angle reaches −30° and electrons transfer back. We obtained the same result in our previous work [33]. This suggests that 3 Å is a minimum value for both deactivation pathways. At larger distances, the excited system evolves to an excimer characterized by charge transfer; at shorter distances, the strong intermolecular interaction may change the redox potential of bases and result in charge recombination, which leads to two neutral molecules. We have previously studied the effect of interbase distance (from 3.4 to 4.4 Å) using SERID [38]. The results suggest that 4.2 Å is the upper limit for the deactivation pathways associated with π stacking.

Due to the substantial defects of the mean field theory used in SERID, the electronic states are not explicit. The potential energy surfaces for the S_1 and S_0 states were calculated by using long-range corrected time-dependent density functional (LRC-TD-DFT) theory [39–42] for comparison and the results are summarized in Figure 6. The Cam-B3LYP function, which was reported to describe charge transfer state well [43–45], was used in this research. In this calculation, energies of serial single points taken along the simulation trajectory were calculated. A CI with energy value of 2.5 eV was observed at 990 fs in the TDDFT potential energy surface, which is very close to avoided crossing in our simulation. The non-optimized initial ground state geometry results in a "quasi vertical excited energy" of 3.2 eV, which is much lower than CASPT2 result of 4.41 eV [26]. However, the TD-DFT and CASPT2 calculations still yield comparable values for the energy gap between the Frank-Condon point and CI (0.7 eV and 0.9 eV, resp.). Based on

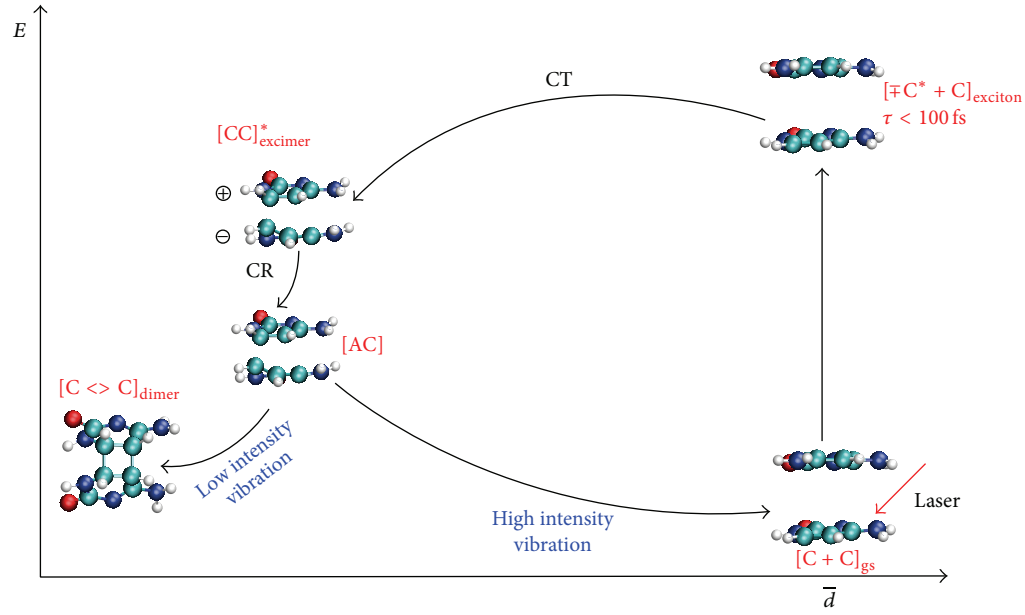

FIGURE 8: Mechanism of photodimerization reaction of π-stacked cytosines system. The abbreviations are interpreted as follows: CT, charge transfer; CR, charge recombination; AC, avoided crossing; gs, ground state.

[26], we believe that an optimized ground state will be located at −1.21 eV level in the current coordinate system. Therefore, the energy of the CI will be 3.71 eV, which agrees well with 3.5 eV from CASPT2. In [26], the CASPT2 calculation also yields a minimum in S_1 that is lower than the CI by 0.2 eV, as same as our TD-DFT results. Our simulation indicates that from the minimum, the (C∗C) excimer has to overcome a barrier of 0.9 eV to reach the funnel. The stability of the excimer may decrease the effectiveness of internal conversion in the singlet manifold compared to the thymine excimer. This explains why stacked thymines have lifetime of (about 600 fs [38]) which is shorter than stacked cytosine; internal conversion of the thymine excimer goes through a barrierless pathway. The geometry of the CI is shown in Figure 5. The C_5–C_5' and C_6–C_6' are 2.13 and 2.19 Å respectively, compare to 2.27 and 2.17 Å respectively in results of CASPT2. The similar geometries suggest that this semiclassical dynamics simulation is credible.

In our previous study [33], π-stacked cytosines could form CPD by laser pulse irradiation. In the dimerization mechanism, an evolution of "ultrafast exciton" to "charge transfer excimer" and ultimately leading to formation of CPD was reported. It is hard to understand that the almost identical approach in this work follows a photophysical deactivation mechanism. In order to distinguish dimerization and photophysical deactivation mechanism of π-stacked cytosines, we counted multiple trajectories simulations results. Different initial stacking orientations, with average intermolecular distance of 3.4 Å and dihedral C_5–C_6–C_6'–C_5' of 36°, were used in multiple trajectories simulations. Simulations gave rise to both dimerization and photophysical deactivation pathway. To compare the vibrational degree of freedom, seven dimerization pathways and seven excimer pathways were chosen and several geometrical parameters with respect to central C_5–C_6 bond, namely, the distance of C_6–N_1 and C_6–H_6 and dihedral angles of C_2–N_1–C_6–C_5 and C_4–C_5–C_6–H_6, are presented in Figure 7. The red solid lines represent dimerization channels and blue dashed lines represent the photophysical deactivations channels., respectively. Excited state lifetimes of the all fourteen trajectories are approximately 350 fs because of the relatively short intermolecular distance [38]. All of the four aforementioned degrees of freedom have larger vibrational amplitudes in the photophysical channel before nonadiabatic transition. It suggests that vibration decreases possibility of bonding between C_5 or C_6 atoms.

Obviously, through the CI in PES, both evolution forward to photoproducts and back to reactants are possible. Therefore, two competitive channels exist in π-stacked cytosines system. Figure 8 summarizes the changes in molecular geometry for representative trajectories from the competing pathways. Shortly after application of the laser pulse (<100 fs), a neutral dipolar coupling excited state with ultrashort lifetime, an exciton, is formed. After 120 fs, the twisting of dihedral angle C_2–N_1–C_6–C_5 increases the electron affinity of **C** and leads to a transfer of 1.4 electrons from **C**′ to **C**. As a result, an charge transfer excimer is formed. When two bases approach to within a distance of about 3 Å, charge recombination occurs; the stacked cytosines revert to neutral. The system evolves to an avoided crossing due to vibrational coupling of the HOMO and LUMO induced by maximal deformation of **C** and **C**′ molecules. At avoided crossing, vibrational energy distribution determines the deactivation fate.

4. Conclusion

This paper presents simulation results for the photophysical deactivation of the π-stacked cytosine system following excitation subjected by a laser pulse with 4.1 eV photon energy. Only one cytosine is excited at the beginning. Excitation initially leads to the formation of a charge separated neutral exciton state with a lifetime of 100 fs. An "excimer state" results from charge transfer that occurs when the interbase distance is 3.8 Å in this simulation. Charge recombination occurs when the interbase distance shortens to about 3 Å, leading to neutral stacked bases that evolve into an avoided crossing prior to deactivation. Geometries taken from avoided crossing are very similar to the S_1/S_0 CI obtained by CASSCT/CASPT2 [40, 41]. Torsional vibrations (C_2–N_1–C_6–C_5 and C_2'–N_1'–C_6'–C_5') play a significant role in vibronic coupling between the HOMO and LUMO and lead to nonadiabatic transition of the molecules to the ground state.

The geometries of avoided crossing are almost the same as those for dimerization channel reported previously. It indicates there are two competitive de-exciton channels at avoided crossing. Higher amplitude vibrations of C_5 or C_6 atoms favor the photophysical deactivation pathway.

To compare with other theoretical results, S_1 and S_0 PESs were calculated at TD-DFT level along with simulation trajectory. The CI was found to be very near the avoided crossing obtained by SERID method. The TD-DFT calculation yields a 0.2 eV barrier between the minimum of S_1 and CI, indicating a relatively stable excimer in π-stacked cytosines system, which lessens the effectiveness of internal conversion compared to thymine excimer, which has a barrierless pathway from S_1 to CI.

Conflict of Interests

The authors declare that there is no conflict of interests regarding the publication of this paper.

Acknowledgments

This work is supported by the Joint Funds of the National Natural Science Foundation of China (Grant No. U1330138) and the Natural Science Foundation Project of CQ CSTC (cstc2011jjA00009) and Project of the Science Technology Foundation of Chongqing Education Committee, China (no. KJ120516 and KJ120521).

References

[1] J. Cadet, E. Sage, and T. Douki, "Ultraviolet radiation-mediated damage to cellular DNA," *Mutation Research/Fundamental and Molecular Mechanisms of Mutagenesis*, vol. 571, no. 1-2, pp. 3–17, 2005.

[2] R. Beukers, A. P. M. Eker, and P. H. M. Lohman, "50 years thymine dimer," *DNA Repair*, vol. 7, no. 3, pp. 530–543, 2008.

[3] S. Mouret, C. Baudouin, M. Charveron, A. Favier, J. Cadet, and T. Douki, "Cyclobutane pyrimidine dimers are predominant DNA lesions in whole human skin exposed to UVA radiation," *Proceedings of the National Academy of Sciences of the United States of America*, vol. 103, no. 37, pp. 13765–13770, 2006.

[4] V. O. Melnikova and H. N. Ananthaswamy, "Cellular and molecular events leading to the development of skin cancer," *Mutation Research/Fundamental and Molecular Mechanisms of Mutagenesis*, vol. 571, no. 1-2, pp. 91–106, 2005.

[5] M. McCullagh, M. Hariharan, F. D. Lewis, D. Markovitsi, T. Douki, and G. C. Schatz, "Conformational control of TT dimerization in DNA conjugates: a molecular dynamics study," *Journal of Physical Chemistry B*, vol. 114, no. 15, pp. 5215–5221, 2010.

[6] L. Serrano-Andrés, M. Merchán, and A. C. Borin, "A three-state model for the photophysics of adenine," *Chemistry: A European Journal*, vol. 12, no. 25, pp. 6559–6571, 2006.

[7] J. M. Pecourt, J. Peon, and B. Kohler, "DNA excited-state dynamics: ultrafast internal conversion and vibrational cooling in a series of nucleosides," *Journal of the American Chemical Society*, vol. 123, no. 42, pp. 10370–10378, 2001.

[8] N. Ismail, L. Blancafort, M. Olivucci, B. Kohler, and M. A. Robb, "Ultrafast decay of electronically excited singlet cytosine via a π, π^* to n_0, π^* state switch," *Journal of the American Chemical Society*, vol. 124, no. 24, pp. 6818–6819, 2002.

[9] H. Langer, N. L. Doltsinis, and D. Marx, "Excited-state dynamics and coupled proton-electron transfer of guanine," *ChemPhysChem*, vol. 6, no. 9, pp. 1734–1737, 2005.

[10] M. Barbatti and H. Lischka, "Can the nonadiabatic photodynamics of aminopyrimidine be a model for the ultrafast deactivation of adenine?" *Journal of Physical Chemistry A*, vol. 111, no. 15, pp. 2852–2858, 2007.

[11] H. R. Hudock, B. G. Levine, A. L. Thompson et al., "Ab Initio molecular dynamics and time-resolved photoelectron spectroscopy of electronically excited uracil and thymine," *Journal of Physical Chemistry A*, vol. 111, no. 34, pp. 8500–8508, 2007.

[12] W. Kwok, C. Ma, and D. L. Phillips, "Femtosecond time- and wavelength-resolved fluorescence and absorption spectroscopic study of the excited states of adenosine and an adenine oligomer," *Journal of the American Chemical Society*, vol. 128, no. 36, pp. 11894–11905, 2006.

[13] C. E. Crespo-Hernández and B. Kohler, "Influence of secondary structure on electronic energy relaxation in adenine homopolymers," *Journal of Physical Chemistry B*, vol. 108, no. 30, pp. 11182–11188, 2004.

[14] C. T. Middleton, K. de La Harpe, C. Su, Y. K. Law, C. E. Crespo-Hernández, and B. Kohler, "DNA excited-state dynamics: from single bases to the double helix," *Annual Review of Physical Chemistry*, vol. 60, pp. 217–239, 2009.

[15] B. Bouvier, J. P. Dognon, R. Lavery et al., "Influence of conformational dynamics on the exciton states of DNA oligomers," *Journal of Physical Chemistry B*, vol. 107, no. 48, pp. 13512–13522, 2003.

[16] E. Emanuele, D. Markovitsi, P. Millié, and K. Zakrzewska, "UV spectra and excitation delocalization in DNA: influence of the spectral width," *ChemPhysChem*, vol. 6, no. 7, pp. 1387–1392, 2005.

[17] D. Onidas, T. Gustavsson, E. Lazzarotto, and D. Markovitsi, "Fluorescence of the DNA double helices (dAdT)n·(dAdT) n studied by femtosecond spectroscopy," *Physical Chemistry Chemical Physics*, vol. 9, no. 37, pp. 5143–5148, 2007.

[18] I. Buchvarov, Q. Wang, M. Raytchev, A. Trifonov, and T. Fiebig, "Electronic energy delocalization and dissipation in single- and

double-stranded DNA," *Proceedings of the National Academy of Sciences of the United States of America*, vol. 104, no. 12, pp. 4794–4797, 2007.

[19] Z. Z. Pan, M. McCullagh, G. C. Schatz, and F. D. Lewis, "Conformational control of thymine photodimerization in purine-containing trinucleotides," *The Journal of Physical Chemistry Letters*, vol. 2, no. 12, pp. 1432–1438, 2011.

[20] M. Z. Zgierski, T. Fujiwara, and E. C. Lim, "Conical intersections and ultrafast intramolecular excited-state dynamics in nucleic acid bases and electron donor-acceptor molecules," *Chemical Physics Letters*, vol. 463, no. 4-6, pp. 289–299, 2008.

[21] C. E. Crespo-Hernández, B. Cohen, and B. Kohler, "Molecular spectroscopy: complexity of excited-state dynamics in DNA (Reply)," *Nature*, vol. 441, artcile E8, 2006.

[22] B. Cohen, P. M. Hare, and B. Kohler, "Ultrafast excited-state dynamics of adenine and monomethylated adenines in solution: implications for the nonradiative decay mechanism," *Journal of the American Chemical Society*, vol. 125, no. 44, pp. 13594–13601, 2003.

[23] T. Takaya, C. Su, K. de la Harpe, C. E. Crespo-Hernández, and B. Kohler, "UV excitation of single DNA and RNA strands produces high yields of exciplex states between two stacked bases," *Proceedings of the National Academy of Sciences of the United States of America*, vol. 105, no. 30, pp. 10285–10290, 2008.

[24] C. E. Crespo-Hernández, B. Cohen, and B. Kohler, "Base stacking controls excited-state dynamics in A·T DNA," *Nature*, vol. 436, no. 7054, pp. 1141–1144, 2005.

[25] G. Olaso-González, M. Merchán, and L. Serrano-Andrés, "The role of adenine excimers in the photophysics of oligonucleotides," *Journal of the American Chemical Society*, vol. 131, no. 12, pp. 4368–4377, 2009.

[26] D. Roca-Sanjuán, G. Olaso-González, I. González-Ramírez, L. Serrano-Andrés, and M. Merchán, "Molecular basis of DNA photodimerization: intrinsic production of cyclobutane cytosine dimers," *Journal of the American Chemical Society*, vol. 130, no. 32, pp. 10768–10779, 2008.

[27] J. J. Serrano-Pérez, I. González-Ramírez, P. B. Coto, M. Merchán, and L. Serrano-Andrés, "Theoretical insight into the intrinsic ultrafast formation of cyclobutane pyrimidine dimers in UV-irradiated DNA: thymine versus cytosine," *Journal of Physical Chemistry B*, vol. 112, no. 45, pp. 14096–14098, 2008.

[28] Y. Dou, B. R. Torralva, and R. E. Allen, "Semiclassical electron-radiation-ion dynamics (SERID) and cis-trans photoisomerization of butadiene," *Journal of Modern Optics*, vol. 50, no. 15–17, pp. 2615–2643, 2003.

[29] Y. Dou, B. R. Torralva, and R. E. Allen, "Interplay of electronic and nuclear degrees of freedom in a femtosecond-scale photochemical reaction," *Chemical Physics Letters*, vol. 392, no. 4–6, pp. 352–357, 2004.

[30] M. Graf and P. Vogl, "Electromagnetic fields and dielectric response in empirical tight-binding theory," *Physical Review B*, vol. 51, no. 8, pp. 4940–4949, 1995.

[31] R. E. Allen, T. Dumitrica, and B. R. Torralva, "Electronic and structural response of materials to fast, intense laser pulses," in *Ultrafast Physical Processes in Semiconductors, Tsen*, K. T. Tsen, Ed., chapter 7, Academic Press, New York, NY, USA, 2001.

[32] M. Ben-Nun and T. J. Martínez, "AB initio quantum molecular dynamics," *Advances in Chemical Physics*, vol. 121, pp. 439–512, 2002.

[33] S. Yuan, W. Zhang, L. Liu, Y. Dou, W. Fang, and G. V. Lo, "Detailed mechanism for photoinduced cytosine dimerization: a semiclassical dynamics simulation," *Journal of Physical Chemistry A*, vol. 115, no. 46, pp. 13291–13297, 2011.

[34] A. Sharonov, T. Gustavsson, V. Carré, E. Renault, and D. Markovitsi, "Cytosine excited state dynamics studied by femtosecond fluorescence upconversion and transient absorption spectroscopy," *Chemical Physics Letters*, vol. 380, no. 1-2, pp. 173–180, 2003.

[35] B. Kohler, "Nonradiative decay mechanisms in DNA model systems," *Journal of Physical Chemistry Letters*, vol. 1, no. 13, pp. 2047–2053, 2010.

[36] E. R. Bittner, "Lattice theory of ultrafast excitonic and charge-transfer dynamics in DNA," *Journal of Chemical Physics*, vol. 125, no. 9, Article ID 094909, 12 pages, 2006.

[37] R. Improta, F. Santoro, V. Barone, and A. Lami, "Vibronic model for the quantum dynamical study of the competition between bright and charge-transfer excited states in single-strand polynucleotides: the adenine dimer case," *The Journal of Physical Chemistry A*, vol. 113, no. 52, pp. 15346–15354, 2009.

[38] W. Zhang, *Semiclassical dynamics Simulation for deactivation of stacked bases of DNA [Ph.D. dissertation]*, Northwest University, Xi'an, China, 2011.

[39] H. Iikura, T. Tsuneda, T. Yanai, and K. Hirao, "A long-range correction scheme for generalized-gradient-approximation exchange functionals," *Journal of Chemical Physics*, vol. 115, no. 8, pp. 3540–3544, 2001.

[40] J. W. Song, T. Hirosawa, T. Tsuneda, and K. Hirao, "Long-range corrected density functional calculations of chemical reactions: redetermination of parameter," *Journal of Chemical Physics*, vol. 126, no. 15, Article ID 154105, 2007.

[41] O. A. Vydrov and G. E. Scuseria, "Intermittent search process and teleportation," *Journal of Chemical Physics*, vol. 126, no. 23, Article ID 234109, 2007.

[42] T. M. Henderson, B. G. Janesko, and G. E. Scuseria, "Generalized gradient approximation model exchange holes for range-separated hybrids," *Journal of Chemical Physics*, vol. 128, no. 19, Article ID 194105, 2008.

[43] F. Santoro, V. Barone, and R. Improta, "Can TD-DFT calculations accurately describe the excited states behavior of stacked nucleobases? The cytosine dimer as a test case," *Journal of Computational Chemistry*, vol. 29, no. 6, pp. 957–964, 2008.

[44] F. Santoro, V. Barone, and R. Improta, "Excited states decay of the A-T DNA: a PCM/TD-DFT study in aqueous solution of the (9-methyl-adenine)$_2$·(1-methyl-thymine)$_2$ stacked tetramer," *Journal of the American Chemical Society*, vol. 131, no. 42, pp. 15232–15245, 2009.

[45] A. W. Lange and J. M. Herbert, "Both intra- And interstrand charge-transfer excited states in aqueous B-DNA are present at energies comparable to, or just above, the $1\pi\pi*$ excitonic bright states," *Journal of the American Chemical Society*, vol. 131, no. 11, pp. 3913–3922, 2009.

Hindawi Publishing Corporation
International Journal of Photoenergy
Volume 2014, Article ID 346272, 6 pages
http://dx.doi.org/10.1155/2014/346272

Research Article

Electron Correlation Effects on the Longitudinal Polarizabilities and Second Hyperpolarizabilities of Polyenes: A Finite Field Study

Qingxu Li,[1] Xianju Zhou,[1] and Shiwei Yin[2]

[1] *College of Sciences, Chongqing University of Posts and Telecommunications, Chongqing 400065, China*
[2] *School of Chemistry & Chemical Engineering, Shaanxi Normal University, Xi'an 710062, China*

Correspondence should be addressed to Qingxu Li; liqx@cqupt.edu.cn

Received 16 April 2014; Revised 11 June 2014; Accepted 11 July 2014; Published 23 July 2014

Academic Editor: Yusheng Dou

We carry out ab initio calculations, based on finite-field scheme, of the longitudinal polarizabilities (α_L) and second hyperpolarizabilities (γ_L) of conjugated polyenes, and study the effects of electron correlation, with second-order Moller-Plesset perturbation theory and coupled cluster with singles and doubles method. Calculations with density functional theory are also made to compare with wave-function based methods. Our study shows that electron correlation reduces linear longitudinal polarizability and enhances longitudinal second hyperpolarizability for short polyenes, but the effects decrease as the chain increases; choosing appropriate basis sets is important when quantitative results are required.

1. Introduction

The linear and nonlinear optical properties of conjugated polymers have been intensely investigated in recent decades due to their great potentials in industry. The polarizability and second hyperpolarizability of linear polyenes, the simplest conjugated polymer, have attracted research interests of many scientists. Ab initio calculations of linear α_L and γ_L are severely restricted to short polyenes due to the formidable computational costs. Hurst et al. reported ab initio coupled-perturbed HF (CPHF) calculations up to $C_{22}H_{24}$ more than 20 years ago [1]. Since then, researchers have showed that electron correlation effects play a key role in correctly describing the linear and nonlinear optical properties of conjugated systems [2–21]. And thus, proper treatment of electron correlation in electronic structure calculations is very important. However, accurate correlated electronic structure calculations for long polyenes require immense computational resources and thus are now impractical.

DFT method becomes more popular in recent years for its excellent balance between the accuracy and computational costs [22, 23]. Unfortunately, researches showed that DFT with commonly used xc-functionals always fails to offer a reasonable description of nonlinear optical properties for conjugated polymers, including polyenes [12–15]. In a recent work, Sekino et al. reported their efforts on developing new xc-functional to overcome this problem [15]. They also reported their calculations based on by MP2 (second-order Moller-Plesset perturbation theory) and CCSD (coupled cluster with singles and doubles method). Eventually, MP2 is the only practical choice for long polyenes till now. CCSD is more expensive and thus more restricted when used for evaluation of α_L and γ_L, even for the 6-31G basis set, the smallest basis set of practical use. Champagne et al. used MP2 method to invalidate DFT in evaluating α_L and γ_L of conjugated chains [12].

We found recently that, based on the semiempirical Pariser-Parr-Pople (PPP) model, CCSD predicts electron correlation results in a reduction on γ_L for long polyenes, while MP2 predicts electron correlation always enhances γ_L and thus gives wrong predictions for electron correlation contributions to the γ_L of long polyenes [9]. The primary ab initio CCSD calculations we made with 6-31G basis set lead to same conclusions to semiempirical PPP model.

Hurst et al. showed that basis sets of quasi-double zeta quality are good enough, particularly for the longitudinal component. Since their conclusion were based on CPHF calculations, we wonder if more reliable basis sets will still support this point. Calculations with various basis sets are thus performed and reported in this paper. Results obtained by three commonly-used DFT schemes are also presented for the sake of completeness.

2. Computational Details

The geometries of polyenes used in this study were taken from [12] (Figure 1(a) in [12]). Electronic energies for the system in different electric fields are calculated with Gaussian 03 package [24]. After that, the finite field method is used to evaluate the longitudinal polarizability (α_L) and second hyperpolarizability (γ_L) with the following numerical formulae:

$$\alpha_L = -\frac{E(\delta F) + E(-\delta F) - 2E(0)}{(\delta F)^2},$$
$$\gamma_L = -\frac{E(2\delta F) - 4E(\delta F) + 6E(0) - 4E(-\delta F) + E(-2\delta F)}{(\delta F)^4}. \quad (1)$$

The electric fields used are 0, 8, 16×10^{-4} a.u. (i.e., $\delta F = 8 \times 10^{-4}$ a.u). As is known, large electric field will result in troubles in convergence and small electric field will require more significant figures for numerical derivatives and consequently is more computationally expensive. We found $\delta F = 8 \times 10^{-4}$ a.u can work well for systems studied in this work. The electric field is applied along the direction of chain, as is chosen as x axis direction. Only longitudinal components $\alpha_{xx}(\alpha_L)$ and $\gamma_{xxxx}(\gamma_L)$ are calculated.

3. Results and Discussions

The results of longitudinal polarizabilities per unit cell α_L/N (N is number of unit cells or double bonds in the system) are gathered in Table 1. And the data obtained with 6-31G basis set are plotted in Figure 1. Champagne et al. reported their calculations in [12] for $C_{12}H_{14}$ and $C_{20}H_{22}$ with same geometries (double zeta basis set used for $C_{12}H_{14}$ and 6-31G used for the other, see details in [12]). DFT data reported here for $C_{20}H_{22}$ are exactly the same as those in [12] (all data mentioned here and after can be found in Tables 1–4 in [12]) as expected. Small differences (SVWN: 94.8, B3LYP: 87.0, reported in [12]) for $C_{12}H_{14}$ can attribute to different basis set used in calculations. This can also explain the difference between HF and MP2 results; besides, that coupled HF (CHF) was used in [12]. In Figure 1, all curves obtained by DFT schemes are above HF; however, MP2 and CCSD curves are below that of HF. One can easily see the failure of commonly used xc-fuctionals here, as was shown before by others [12–14]. SVWN and BLYP predict nearly identical results. Another point worth to mention is the difference between CCSD and MP2 increases as the chain grows. It becomes more important while quantitative or semiquantitative results

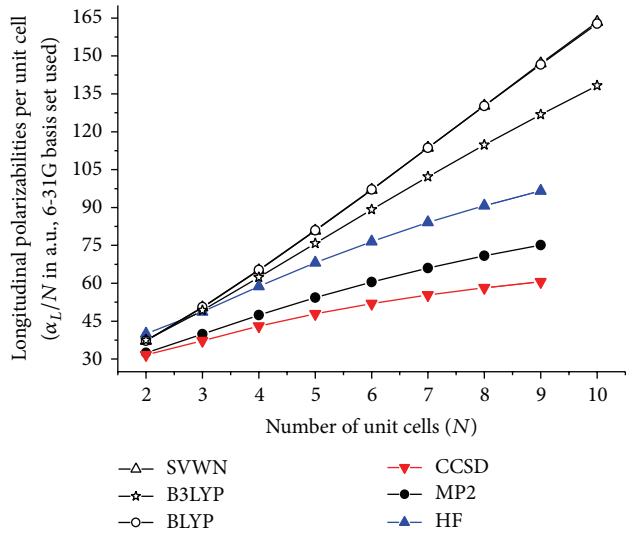

Figure 1: Longitudinal polarizabilities per unit cell (α_L/N) of polyenes (in a.u.) obtained by various quantum chemical methods with 6-31G basis set.

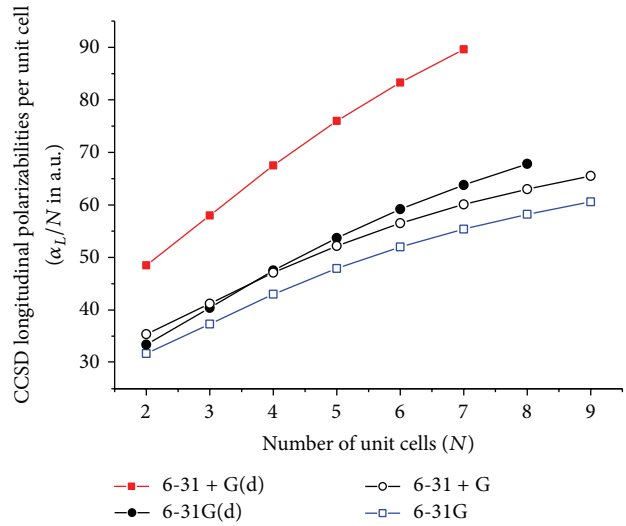

Figure 2: Longitudinal polarizabilities per unit cell (α_L/N) of polyenes (in a.u.) obtained by CCSD with various basis sets.

are required for long polyenes. Similar conclusions can be made for other basis sets from Table 1.

From Table 1, we conclude that basis set effects are unimportant for all DFT methods used here. Things are different for HF, MP2, and CCSD methods. We plot the CCSD results with various basis sets in Figure 2. The largest and also the most reliable basis set 6-31+G(d) is steeper than the other three ones. The differences between 6-31+G(d) basis set and other basis sets range from 27% to 38%. There are no essential difference between 6-31G, 6-31+G, and 6-31G(d) basis sets.

We now come to γ_L. The results are listed in Table 2, and the data obtained with 6-31G basis set are plotted in Figure 3. We first discuss results for 6-31G basis set. For DFT methods with 6-31G basis set, negligible differences

Table 1: Longitudinal polarizabilities per unit cell α_L/N of polyenes obtained by various chemical models (in a.u., N is the number of unit cells or double bonds in the system).

N	2	3	4	5	6	7	8	9	10
6-31G									
HF	40.0	48.7	58.8	68.1	76.5	84.1	90.7	96.6	
MP2	32.5	39.9	47.4	54.3	60.5	66.0	70.9	75.1	
CCSD	31.7	37.3	43.0	47.9	52.0	55.4	58.2	60.6	
SVWN	37.2	50.4	65.1	80.8	97.0	114	130	147	163
BLYP	37.3	50.6	65.3	81.0	97.1	114	130	147	163
B3LYP	37.4	49.3	62.4	75.8	89.2	102	115	127	138
6-31G(d)									
HF	39.4	48.4	58.4	67.7	76.1	83.5	90.1		
MP2	33.5	42.0	50.6	58.7	66.1	72.8	78.7		
CCSD	33.4	40.4	47.5	53.7	59.2	63.8	67.8		
SVWN	37.4	51.1	66.0	82.0	98.6	116	133	150	167
BLYP	37.5	51.2	66.1	82.0	98.5	115	132	149	166
B3LYP	37.5	49.8	63.1	76.8	90.4	104	117	129	141
6-31+G									
HF	43.7	52.6	62.8	72.2	80.7	88.3	94.9	101	
MP2	36.8	44.5	52.3	59.5	65.9	71.7	76.7	81.1	
CCSD	35.4	41.2	47.1	52.2	56.5	60.1	63.0	65.5	
SVWN	41.6	55.3	70.4	86.5	103	120	137	154	171
BLYP	42.4	56.3	71.5	87.6	104	121	138	155	171
B3LYP	41.8	54.2	67.6	81.3	94.9	108	121	133	145
6-31+G(d)									
HF	56.4	68.4	81.8	94.1	105	115			
MP2	49.3	61.0	72.7	83.6	93.6	103			
CCSD	48.5	58.0	67.5	76.0	83.3	89.6			
SVWN	41.9	56.1	71.6	87.9	105	122	140	157	174
BLYP	42.7	57.1	72.6	89.0	106	123	140	157	174
B3LYP	42.1	54.9	68.6	82.6	96.5	110	123	135	147

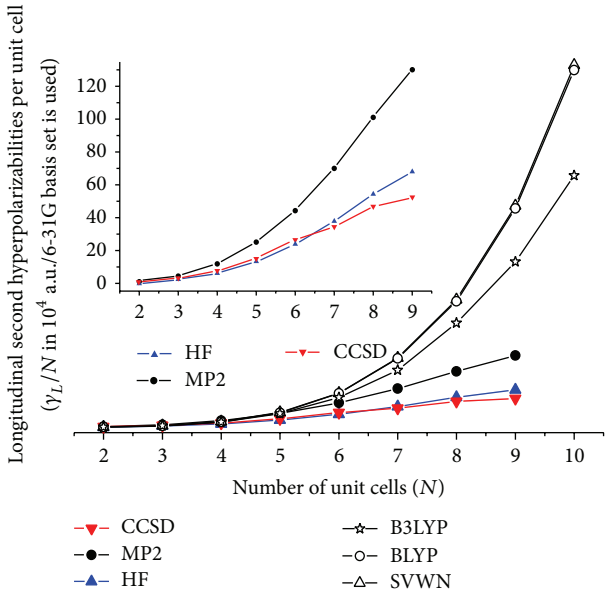

Figure 3: Longitudinal second hyperpolarizabilities per unit cell (γ_L/N) of polyenes (in 10^4 a.u.) obtained by various quantum chemical methods with 6-31G basis set.

appear when compared to those reported in [12]. One more thing to be mentioned here is that electric fields and numerical derivatives formulae will result in some differences on digitals. It is very interesting, seen from Figure 3, that CCSD calculations predict electron correlation will reduce γ_L while $N > 6$, fully contrary to those predicted by MP2, but the question is whether this point can be also confirmed by more reliable basis sets. Similar results can be found for calculations with 6-31+G basis set and now the sign inversion of correlation contribution occurs at $C_{18}H_{20}$, while, for 6-31G(d) and 6-31+G(d), this sign inversion has not been observed. One interesting problem then appears whether this sign inversion will occur or not for those two basis sets. If the answer is yes (we believe so), the commonly used MP2 (due to its moderate computational costs) makes qualitatively wrong predictions for correlation contribution on γ_L for long polyenes. Undoubtedly, further work is necessary to completely confirm this. The local CCSD method developed recently may be helpful to investigate the longer polyenes [10, 25–32].

In Figure 4, we plotted γ_L/N calculated by CCSD with various basis sets. Again, 6-31+G(d) basis set performs

Table 2: Longitudinal second hyperpolarizabilities per unit cell γ_L/N of polyenes obtained by various chemical models (in 10^4 a.u., N is the number of unit cells or double bonds in the system).

N	2	3	4	5	6	7	8	9	10
6-31G									
HF	−0.12	1.93	5.85	12.9	23. 6	37.6	54.5	67.8	
MP2	0.84	4.33	11. 8	24. 9	44.4	70.2	101	131	
CCSD	0.80	3.11	7.44	15.3	26.5	34.5	46.7	52.3	
SVWN	0.15	2.80	9.91	26.9	61.8	126	232	403	659
BLYP	0.15	2.09	9.30	26.1	61.4	125	229	398	650
B3LYP	0.14	2.29	9.25	24.5	54.2	104	190	301	458
6-31G(d)									
HF	−0.11	1.79	5.38	11.9	21.4	33.9	49.3		
MP2	0.67	3.83	10.8	23.4	42.2	67.4	98.8		
CCSD	0.60	4.04	8.71	16.6	27.2	40.3	56.3		
SVWN	0.14	2.59	9.26	22.6	63.9	116	232	392	644
BLYP	0.13	2.57	9.25	23.1	60.0	121	231	384	637
B3LYP	0.12	2.63	9.07	23.5	51.6	99.2	173	278	422
6-31+G									
HF	0.42	3.56	8.78	17.4	30.0	45.5	62.3	85.2	
MP2	1.92	7.08	16.9	33.0	56.1	85.6	125	161	
CCSD	1.59	5.39	11.7	21.0	31.8	45.5	63.2	70.8	
SVWN	1.07	5.45	15.4	37.2	79.3	158	285	433	711
BLYP	1.18	5.71	16.9	40.0	83.2	159	357	468	728
B3LYP	0.98	5.30	15.2	35.1	69.0	148	216	335	497
6-31+G(d)									
HF	0.75	5.80	14.1	26.4	46.7	71.5			
MP2	2.88	11.1	26.8	51.5	91.5	141			
CCSD	2.70	9.01	19.5	35.3	59.3	89.0			
SVWN	1.08	5.26	14.76	35.5	76.0	148	269	450	709
BLYP	1.19	5.76	15.2	36.1	78.8	154	280	468	782
B3LYP	0.99	5.27	13.9	31.0	66.6	117	209	342	485

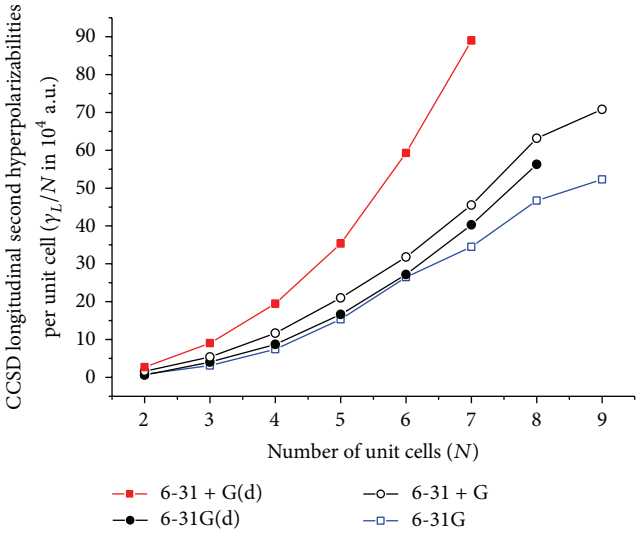

Figure 4: Longitudinal second hyperpolarizabilities per unit cell (γ_L/N, in 10^4 a.u.) obtained by CCSD with various basis sets.

obviously different from the other three. The difference for γ_L/N between 6-31+G(d) basis set and other basis sets ranges from 41% to 61%. And the 6-31G, 6-31+G, and 6-31G(d) basis sets perform similarly.

Sekino et al. reported their results based on CCSD calculations with cc-pVDZ basis set for polyenes up to $C_{12}H_{14}$ with a very different geometry (in the sense of bond length alternation) [15]. In their results, both CCSD and MP2 predict a positive correlation contribution for γ_L up to $N = 6$. Limacher et al. reported similar results based on calculations with response theory methods [33].

4. Conclusions

We have calculated the longitudinal polarizabilities and second hyperpolarizabilities of polyenes using HF, MP2, and CCSD methods and 6-31G, 6-31+G, 6-31G(d), and 6-31+G(d) basis sets. Both MP2 and CCSD predict a negative correlation contribution for longitudinal polarizability, while DFT calculations using SVWN, BLYP, and B3LYP schemes all

predicts positive correlation contributions. For second hyperpolarizability, a sign inversion of correlation contribution is observed for CCSD calculations with 6-31G and 6-31+G basis sets. This sign inversion is yet to be further confirmed by more reliable basis set in the future. Contrary to CCSD, MP2 predicts a positive correlation contribution and thus should be used with much caution for evaluation of second hyperpolarizabilities of long conjugated chains. Addition of diffuse and polarization functions will enhance γ_L obviously, but addition of polarization functions or addition of diffuse functions makes no essential difference.

Conflict of Interests

The authors declare that there is no conflict of interests regarding the publication of this paper.

Acknowledgments

This work is supported by National Natural Science Foundation of China (NSFC: 20903123), Natural Science Foundation Project of CQ CSTC (2010BB4116), and The Research Station Funding for Doctorial Faculty Members of Chongqing University of Posts and Telecommunications (A2008-16).

References

[1] G. Hurst, M. Dupuis, and E. Clementi, "Ab initio analytic polarizability, first and second hyperpolarizabilities of large conjugated organic molecules: applications to polyenes C_4H_6 to $C_{22}H_{24}$," *The Journal of Chemical Physics*, vol. 89, no. 1, pp. 385–395, 1988.

[2] B. Kirtman and B. Champagne, "Nonlinear optical properties of quasilinear conjugated oligomers, polymers and organic molecules," *International Reviews in Physical Chemistry*, vol. 16, no. 4, pp. 389–420, 1997.

[3] B. M. Pierce, "A theoretical analysis of third-order nonlinear optical properties of linear polyenes and benzene," *The Journal of Chemical Physics*, vol. 91, no. 2, pp. 791–811, 1989.

[4] D. R. Kanis, M. A. Ratner, and T. J. Marks, "Third-order nonlinear optical response in organic materials: theoretical and experimental aspects," *Chemical Reviews*, vol. 94, no. 1, pp. 195–242, 1994.

[5] C. Adant, J. L. Brédas, and M. Dupuis, "An ab initio and semiempirical study of the first- and third-order polarizabilities in benzene and thiophene derivatives: electron correlation effects," *Journal of Physical Chemistry A*, vol. 101, no. 16, pp. 3025–3031, 1997.

[6] D. Jacquemin, J. M. André, and E. A. Perpète, "Geometry, dipole moment, polarizability and first hyperpolarizability of polymethineimlne: an assessment of electron correlation contributions," *Journal of Chemical Physics*, vol. 121, no. 9, pp. 4389–4396, 2004.

[7] D. Jacquemin, E. A. Perpète, and J. André, "NLO response of polymethineimine and polymethineimine/polyacetylene conformers: assessment of electron correlation effects," *International Journal of Quantum Chemistry*, vol. 105, no. 6, pp. 553–563, 2005.

[8] H. Sekino and R. J. Bartlett, "Hyperpolarizabilities of molecules with frequency dependence and electron correlation," *The Journal of Chemical Physics*, vol. 94, no. 5, pp. 3665–3670, 1991.

[9] Q. X. Li, L. P. Chen, and Z. G. Shuai, "Electron correlation effects on the nonlinear optical properties of conjugated polyenes," *Chemical Physics Letters*, vol. 457, no. 1–3, pp. 276–278, 2008.

[10] Q. X. Li, Y. P. Yi, and Z. G. Shuai, "Local approach to coupled cluster evaluation of polarizabilities for long conjugated molecules," *Journal of Computational Chemistry*, vol. 29, no. 10, pp. 1650–1655, 2008.

[11] M. Torrent-Sucarrat, M. Solà, M. Duran, J. M. Luis, and B. Kirtman, "Basis set and electron correlation effects on ab initio electronic and vibrational nonlinear optical properties of conjugated organic molecules," *Journal of Chemical Physics*, vol. 118, no. 2, pp. 711–718, 2003.

[12] B. Champagne, E. A. Perpète, S. J. A. Van Gisbergen et al., "Assessment of conventional density functional schemes for computing the polarizabilities and hyperpolarizabilities of conjugated oligomers: an ab initio investigation of polyacetylene chains," *Journal of Chemical Physics*, vol. 109, no. 23, pp. 10489–10498, 1998.

[13] S. J. A. Van Gisbergen, P. R. T. Schipper, O. V. Gritsenko et al., "Electric field dependence of the exchange-correlation potential in molecular chains," *Physical Review Letters*, vol. 83, no. 4, pp. 694–697, 1999.

[14] B. Champagne, E. A. Perpète, D. Jacquemin et al., "Assessment of conventional density functional schemes for computing the dipole moment and (hyper)polarizabilities of push-pull π-conjugated systems," *Journal of Physical Chemistry A*, vol. 104, no. 20, pp. 4755–4763, 2000.

[15] H. Sekino, Y. Maeda, M. Kamiya, and K. Hirao, "Polarizability and second hyperpolarizability evaluation of long molecules by the density functional theory with long-range correction," *Journal of Chemical Physics*, vol. 126, no. 1, Article ID 014107, 6 pages, 2007.

[16] Z. G. Shuai and J. L. Brédas, "Coupled-cluster approach for studying the electronic and nonlinear optical properties of conjugated molecules," *Physical Review B*, vol. 62, no. 23, pp. 15452–15460, 2000.

[17] H. Sekino and R. J. Bartlett, "Molecular hyperpolarizabilities," *The Journal of Chemical Physics*, vol. 98, no. 4, pp. 3022–3037, 1993.

[18] G. Maroulis, "A systematic study of basis set, electron correlation, and geometry effects on the electric multipole moments, polarizability, and hyperpolarizability of HCl," *The Journal of Chemical Physics*, vol. 108, no. 13, pp. 5432–5448, 1998.

[19] G. Maroulis, "On the accurate theoretical determination of the static hyperpolarizability of trans-butadiene," *The Journal of Chemical Physics*, vol. 111, no. 2, pp. 583–591, 1999.

[20] S. Nénon, B. Champagne, and M. I. Spassova, "Assessing long-range corrected functionals with physically-adjusted range-separated parameters for calculating the polarizability and the second hyperpolarizability of polydiacetylene and polybutatriene chains," *Physical Chemistry Chemical Physics*, vol. 16, no. 15, pp. 7083–7088, 2014.

[21] M. de Wergifosse and B. Champagne, "Electron correlation effects on the first hyperpolarizability of push-pull-π-conjugated systems," *The Journal of Chemical Physics*, vol. 134, no. 7, Article ID 074113, 2011.

[22] R. G. Parr and W. T. Yang, *Density-Functional Theory of Atoms and Molecules*, Oxford University Press, New York, NY, USA, 1989.

[23] W. Koch and M. C. Holthausen, *A Chemist's Guide to Density Functional Theory*, Wiley-VCH, New York, NY, USA, 2000.

[24] C. Revision, M. J. Frisch, G. W. Trucks et al., "Gaussian 03, Revision C.02," Gaussian, Wallingford, Conn, USA, 2004.

[25] C. Hampel and H. Werner, "Local treatment of electron correlation in coupled cluster theory," *Journal of Chemical Physics*, vol. 104, no. 16, pp. 6286–6297, 1996.

[26] M. Schütz and H. Werner, "Low-order scaling local electron correlation methods. IV. Linear scaling local coupled-cluster (LCCSD)," *The Journal of Chemical Physics*, vol. 114, no. 2, pp. 661–681, 2001.

[27] M. Schütz and H. Werner, "Local perturbative triples correction (T) with linear cost scaling," *Chemical Physics Letters*, vol. 318, no. 4-5, pp. 370–378, 2000.

[28] S. H. Li, J. Ma, and Y. S. Jiang, "Linear scaling local correlation approach for solving the coupled cluster equations of large systems," *Journal of Computational Chemistry*, vol. 23, no. 2, pp. 237–244, 2002.

[29] S. H. Li, J. Shen, W. Li, and Y. Jiang, "An efficient implementation of the "cluster-in-molecule" approach for local electron correlation calculations," *The Journal of Chemical Physics*, vol. 125, no. 7, Article ID 074109, 10 pages, 2006.

[30] N. Flocke and R. J. Bartlett, "Localized correlation treatment using natural bond orbitals," *Chemical Physics Letters*, vol. 367, no. 1-2, pp. 80–89, 2003.

[31] N. Flocke and R. J. Bartlett, "A natural linear scaling coupled-cluster method," *Journal of Chemical Physics*, vol. 121, no. 22, article no. 10, pp. 10935–10944, 2004.

[32] G. E. Scuseria and P. Y. Ayala, "Linear scaling coupled cluster and perturbation theories in the atomic orbital basis," *The Journal of Chemical Physics*, vol. 111, no. 18, pp. 8330–8343, 1999.

[33] P. A. Limacher, Q. X. Li, and H. P. Lüthi, "On the effect of electron correlation on the static second hyperpolarizability of conjugated oligomer chains," *Journal of Chemical Physics*, vol. 135, no. 1, Article ID 014111, pp. 1–4, 2011.

Hindawi Publishing Corporation
International Journal of Photoenergy
Volume 2014, Article ID 132149, 18 pages
http://dx.doi.org/10.1155/2014/132149

Research Article

Constraint Trajectory Surface-Hopping Molecular Dynamics Simulation of the Photoisomerization of Stilbene

Yibo Lei,[1,2] Shaomei Wu,[1] Chaoyuan Zhu,[2] Zhenyi Wen,[1] and Sheng-Hsien Lin[2]

[1] *Key Laboratory of Synthetic and Natural Functional Molecule Chemistry of Ministry of Education, College of Chemistry & Materials Science, Shaanxi Key Laboratory of Physico-Inorganic Chemistry, Northwest University, Xi'an 710069, China*

[2] *Department of Applied Chemistry, Institute of Molecular Science and Center for Interdisciplinary Molecular Science, National Chiao-Tung University, Hsinchu 300, Taiwan*

Correspondence should be addressed to Yibo Lei; leiyb@nwu.edu.cn and Chaoyuan Zhu; cyzhu@mail.nctu.edu.tw

Received 3 March 2014; Revised 15 April 2014; Accepted 16 April 2014; Published 7 July 2014

Academic Editor: Yusheng Dou

Combining trajectory surface hopping (TSH) method with constraint molecular dynamics, we have extended TSH method from full to flexible dimensional potential energy surfaces. Classical trajectories are carried out in Cartesian coordinates with constraints in internal coordinates, while nonadiabatic switching probabilities are calculated separately in free internal coordinates by Landau-Zener and Zhu-Nakamura formulas along the seam. Two-dimensional potential energy surfaces of ground S_0 and excited S_1 states are constructed analytically in terms of torsion angle and one dihedral angle around the central ethylenic C=C bond, and the other internal coordinates are all fixed at configuration of the conical intersection. At this conical intersection, the branching ratio from the present simulation is 48 : 52 (33 : 67) initially starting from trans(cis)-Stilbene in comparison with experimental value 50 : 50. Quantum yield for trans-to-cis isomerization is estimated as 49% in very good agreement with experimental value of 55%, while quantum yield for cis-to-trans isomerization is estimated as 47% in comparison with experimental value of 35%.

1. Introduction

Nonadiabatic dynamic based on on-the-fly trajectory surface hopping (TSH) approach is a powerful tool for investigation of the photochemical and photophysical processes involving electronically excited states with conical intersections. Trajectories are run on on-the-fly electronically adiabatic potential energy surfaces while nonadiabatic transitions are treated by mixing quantum/classical or semiclassical methods. In year 1971, the TSH method was already utilized for studying the DH_2^+ nonadiabatic reactions by Tully and Pkeston [1] in which nonadiabatic transition probabilities were calculated by the Landau-Zener (LZ) formula along the seam. Later in year 1990, Tully [2] proposed the fewest switches (FS) algorithm in which nonadiabatic transition probabilities were calculated by the time-dependent first-order coupled equations along running trajectory. By extending LZ theory, Zhu and Nakamura (ZN) [3] developed the better nonadiabatic transition formula that was applied to the DH_2^+ nonadiabatic reactions [4]. Nonadiabatic transition probability calculated by ZN formula is generally larger than that calculated by LZ formula. Extensive studies in comparison of LZ formula with Tully's FS algorithm were carried out for photochemical ring opening in oxirane [5], in which FS transitions were taking place in a wide range of the conic zone while LZ transitions occurred locally around the conic zone. The other theoretical approaches such as Liouville dynamics [6], Bohmian dynamics [7], path integrals [8, 9], and multiple spawning [10] have been proposed. Nonadiabatic dynamic based on Tully's FS algorithm has been widely applied for photochemistry of large molecular and biomolecular systems [11–19] and it has been well documented in the recent review paper [20].

Nonadiabatic transition probabilities calculated from Tully's FS method require calculation of nonadiabatic coupling vectors while the transition probabilities calculated from LZ and ZN formulas require information only from two adiabatic potential energy surfaces around the crossing

seam. The LZ and ZN methods are less expensive than the FS method for TSH. A nuclear motion can be treated separately from electronically nonadiabatic transitions in LZ or ZN method so that a step size of trajectory can be much longer than that of FS method where nuclear motion has to be integrated coupled with electronic motion. Trajectory switching in LZ or ZN method occurs at place very close to crossing seam while trajectory switching in FS method can happen at place far from crossing seam. As a result, number of on-the-fly trajectories can be quite demanding for convergent accuracy in FS method. However, LZ and ZN methods cannot take into account nonadiabatic transitions from noncrossing case. ZN method was successfully applied to nonadiabatic dynamics of two models of protonated Schiff base retinal up to 100 on-the-fly trajectories [21] and photoisomerization of bridged azobenzene [22, 23]. If nonadiabatic transitions are dominated by the crossing seam, LZ and ZN formulas can be applied.

It is a quite successful approach that the potential energies, energy gradients, and nonadiabatic coupling vectors are calculated on-the-fly for trajectories with full degree of freedoms for large systems. However, it can run limited number of on-the-fly trajectories with full-dimensional calculation if high level ab. initio quantum chemistry calculation is performed for potential energy surfaces and nonadiabatic coupling vectors. Although low level ab. initio calculation can increase number of running trajectories, it has limited accuracy for potential energy surfaces. An on-the-fly trajectory with reduced dimension for large systems provides an alternative way for studying nonadiabatic molecular dynamics. Especially when nonadiabatic transitions occur locally involving few degrees of freedom, trajectories can be run on reduced-dimensional either on-the-fly or analytical potential energy surfaces depending on how many degrees of freedom are taken into account. As reduced-dimensional degrees of freedom are usually happening on internal coordinates such as bond lengths, bond angles, and dihedral angles while trajectories are running on Cartesian coordinate systems, we need coordinate transformation between internal and Cartesian coordinates for solving constrained classical Hamiltonian equations. Thus, we need to solve coordinates, momentums, and the Lagrange multipliers simultaneously for which various numerical methods are available [24–30].

The purpose of the present study is to combine TSH method with constraint classical Hamiltonian equations to study nonadiabatic molecular dynamics. LZ or ZN methods are mostly suitable incorporated with TSH for constraint molecular dynamics because nonadiabatic transitions can be treated separately with nuclear motion [31, 32]. The present method provides an alternative way in on-the-fly TSH category for simulating large system with increasing number of trajectories and probes simulation in the nonadiabatic transition zone. It is useful complementary to full-dimensional on-the-fly TSH method. In order to apply the present method, we must investigate detail structure and degrees of freedom of conical intersections before deciding which degrees of freedom can be constrained for interesting photochemical processes. Nonadiabatic dynamics of Stilbene has only been studied by employing the ZN method in a short report [33] and the TSH method on FS algorithm within time-dependent DFT local orbital framework [34, 35]. In contrast, there are many publications on on-the-fly TSH method for nonadiabatic dynamics of azobenzene [22, 23, 34–38]. Therefore, we apply the present method to study photoisomerization of Stilbene in detail.

The isomerization of cis- and trans-Stilbene has been extensively studied for more than forty years and the quantum yields of the photoisomerization were measured experimentally [39, 40]. Three mechanisms were characterized for the isomerization; they are the conventional one-bond flip (OBF) [41], Hula-Twist (HT) [42], and the aborted HT mechanisms [43]. The OBF mechanism involves a 180° rotation around the central ethylenic C=C bond. The HT mechanism is considered as the concerted torsion around the adjacent vinyl-phenyl bond and a remarkable bend of in plane C=C−C angle in accompanying the central ethylenic C=C bond rotation. The aborted HT mechanism is explained as that the rotation of one of two phenyl rings in Stilbene is aborted and turned back. The cis-to-trans and trans-to-cis isomerizations are taken place by going through pathway of conical intersections which are named as OBF-CI [44, 45] and HT-CI [46], respectively.

The Stilbene has cis- and trans-isomers that can be photoinduced and transferred from one to another in accompanying electronically nonadiabatic transition among various electronic states. Traditionally, the isomerization of cis- and trans-conformations has been investigated by computing the ground state S_0 and the lowest excited state S_1. The dominant excitation from the highest occupied molecular orbital (HOMO) to the lowest unoccupied molecular orbital (LUMO) corresponds to the S_1 $\pi\pi^*$ transition which was confirmed to be a bright state [45]. In the recent years, the photoisomerization involving the conical intersections plus fluorescence spectra has been extensively investigated by both experimentalists and theoreticians [34, 35, 44–65]. The OBF mechanism describes isomerization mainly depending on phenyl rotation in which two phenyl rings twist around the central ethylenic C=C bond, but some other torsions might be also included [44–51]. The conical intersection OBF-CI associated with the OBF mechanism was calculated to be the lowest in energy, so that the photoisomerization reactions were predicted to be in favor of this mechanism [45]. The further dynamical simulations were done by calculating evolution of HOMO and LUMO orbitals along with the nuclear motions including all nuclear coordinates [52, 53]. The vibrational normal-mode analysis with specified PES involving the steep route indicated that the vibrational mode with frequency 240 cm^{-1} also strengthens the OBF mechanism [54]. Fuß and coworkers [43, 55, 56] suggested that the HT and the aborted HT mechanisms were deduced from the systematic features of the cis- and trans-photoisomerizations of nonpolar conjugated molecules and these were investigated by the experimental measurements as well [58–60].

Starting from the Franck-Condon (FC) regions, PESs along the reaction coordinate (curved one-dimension) were also investigated [54, 62, 65]. It was analyzed that one-dimensional PESs with respect to the main twist of phenyl

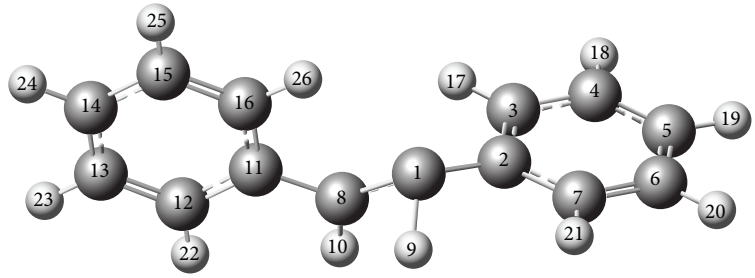

D1: C11-C8-C1-C2
D2: H10-C8-C1-H9

Figure 1: Atom numbering of Stilbene at the S_1/S_0 conical intersection (OBF-CI) configuration in terms of two dihedral angles D1 and D2 at which D10 = −146.6° and D20 = −60.0°.

groups around the central C=C bond reflect the main dynamical effect for isomerization at OBF-CI as mentioned above. The two torsion angles in terms phenyl rotation and the pyramidalization coordinate were utilized for constructing two-dimensional PESs around the OBF-CI [45]. These studies told that at the OBF-CI the two-dimensional PESs can well describe trans-cis nonadiabatic dynamics for Stilbene. The branching ratio is basically determined by potential energy surfaces near the OBF-CI. The one torsion angle around the central ethylenic C=C bond plus one dihedral angle was a suitable choice for isomerization via the OBF-CI (called as D1 and D2 in the present paper as shown in Figure 1). The potential energy surfaces of ground-state S_0 and the first excited state S_1 are constructed in terms of the D1 and D2 angles, and the other internal coordinates are fixed at the OBF-CI configuration.

The rest of this paper is organized as follows. Section 2 first summarizes constrained molecular dynamics method and constructs two-dimensional potential energy surfaces analytically for Stilbene. Trajectory surface hopping with one-passage nonadiabatic transition probability is carried out by LZ and ZN formula. Section 3 presents the implementations of the methods mentioned in Section 2, and results and discussions about branching ratio of isomerization and picture of evolution trajectory are also given therein. Concluding remarks are mentioned in Section 4 followed by three Appendices A, B, and C in which the detailed constraint relations, nonadiabatic transition probability, and hopping scheme are presented.

2. Constraint TSH Molecular Dynamics with LZ and ZN Formulas for Nonadiabatic Transitions

We first introduce constraint molecular dynamics for system with N_c constraints, and then we construct two-dimensional potential energy surfaces (PESs) for Stilbene molecule. Finally, we discuss how LZ and ZN formulas can be applied to TSH for calculating nonadiabatic transition probability along the seam. Of course, we can do on-the-fly nonadiabatic dynamics with four or more dimensional potential energy surfaces. However, it was well studied that two-dimensional PESs are suitable for describing isomerization of Stilbene at OBF-CI. Moreover, for two dimensions we can construct analytical PESs easily and can demonstrate how trajectories run around the seam.

2.1. Constraint Molecular Dynamics. We review constraint molecular dynamics for system with N_c constraints in which the canonical Hamiltonian equations can be written as [24–30]

$$\dot{q}_i = \frac{\partial H(q,p,\lambda)}{\partial p_i} = \frac{p_i}{m_i}, \quad i = 1, 2, \ldots, 3N, \tag{1}$$

$$\dot{p}_i = -\frac{\partial H(q,p,\lambda)}{\partial q_i} = f_i^{\mathrm{uc}} + f_i^{c} = -\frac{\partial V(q)}{\partial q_i} - \sum_k^{N_c} \lambda_k \frac{\partial g_k(q)}{\partial q_i}, \tag{2}$$

where m_i, q_i, and p_i are the mass, the Cartesian coordinate, and conjugate momentum for each atom in molecule, respectively. The $g_k(q) = (k = 1, 2, \ldots, N_c)$ are constraint equations determined by N_c internal coordinates that are fixed at the certain structures of nuclear configuration all the time. The f_i^{uc} and f_i^{c} in (2) stand for unconstraint and constraint force acting on the corresponding atom, respectively. The Hamiltonian with N_c Lagrange multipliers $\lambda_k(t)$ is given as

$$H(q,p,\lambda) = \sum_i^{3N} \frac{p_i^2}{2m_i} + V(q) + \sum_k^{N_c} \lambda_k g_k(q), \tag{3}$$

where $\lambda_k(t)$ are to be determined. As $g_k(q)$ in (3) are zero all the time, the energy conversation is satisfied.

The Lagrange multipliers are solved iteratively. With the given initial Lagrange multipliers, we solve q_i and p_i by the numerical integration of (1) and (2), and then the q_i is inserted into the constraint equations (including bond lengths, bond angles, and dihedral angles) to get the Lagrange multipliers. This iterative process is eventually convergent. The technique to implement this iterative procedure is starting from the classical (Newtonian) equations [27]:

$$m_i \ddot{q}_i(t) = -\frac{\partial}{\partial q_i}\left[V(q) + \sum_{k=1}^{N_c} \lambda_k(t)\, g_k(q)\right]. \tag{4}$$

Integrating both sides of (4) twice in time yields the constraint Cartesian coordinates at the time $t + \Delta t$:

$$q_i(t+\Delta t) = q_i^{\mathrm{uc}}(t+\Delta t) + m_i^{-1}(\Delta t)^2 f_i^c(t) = q_i^{\mathrm{uc}}(t+\Delta t) - m_i^{-1}(\Delta t)^2 \sum_k^{N_c} \lambda_k \frac{\partial g_k(q)}{\partial q_i}, \quad (5)$$

where $q_i^{\mathrm{uc}}(t+\Delta t)$ is solved by unconstrained force. The above $q_i(t+\Delta t)$ can be inserted to every type of the constraint equations to derive N_c nonlinear equations with respect to the corresponding N_c Lagrange multipliers. Although there are a number of algorithms to solve $\lambda_k(t)$, they only differ on how to solve these nonlinear equations. The SETTLE algorithm [28, 29] obtained the solutions of these nonlinear equations analytically for $N_c = 3$ constraints, but it cannot be extended to the large system. The originally simple SHAKE algorithm [24, 25] was developed to solve bond length constraints which are converged linearly. Later advanced M-SHAKE Newton method [24, 25, 30] and quasi-Newton method [30] were straight-forward and fast to solve the nonlinear equations. All of these methods involved the calculations of the Jacobian determinant about the constraint equations $g_k = 0$:

$$J_g = \begin{bmatrix} \frac{\partial g_1}{\partial \lambda_1} & \frac{\partial g_1}{\partial \lambda_2} & \cdots & \frac{\partial g_1}{\partial \lambda_{N_c}} \\ \frac{\partial g_2}{\partial \lambda_1} & \frac{\partial g_2}{\partial \lambda_2} & \cdots & \frac{\partial g_2}{\partial \lambda_{N_c}} \\ \vdots & \vdots & \vdots & \vdots \\ \frac{\partial g_{N_c}}{\partial \lambda_1} & \frac{\partial g_{N_c}}{\partial \lambda_2} & \cdots & \frac{\partial g_{N_c}}{\partial \lambda_{N_c}} \end{bmatrix}, \quad (6)$$

where λ_k are then updated repeatedly by solving the system of linear equations iteratively:

$$\left(J_g\big|_{\lambda_k=0}\right)\lambda = -g\big|_{\lambda_k=0} \quad (7)$$

until the $\max|g_k| < \tau$ $(k = 1, \ldots, N_c)$ in which τ is small number with the prescribed tolerance of the constraints. The Jacobian determinant for the quasi-Newton method is only computed once in the first iteration with the linear convergence, while the Jacobian determinant Newton's method presents quadratic convergence. In the present work, the direct M-SHAKE algorithm is employed and this method is not only to keep the quadratic convergence but also to simplify the derivation and implementation of the nonlinear equations. Detailed derivation of Jacobian determinant is given in Appendix A.

2.2. Two-Dimensional Potential Energy Surfaces for Stilbene. Quenneville and Martínez [45] have done extensive calculation for the critical S_1/S_0 conical intersection OBF-CI and potential energy surfaces in terms of two internal angles: phenyl rotation and the pyramidalization coordinates. They have done detailed comparison for the results calculated by complete active space self-consistent field (CASSCF) and multireference perturbation theory (CASPT2) methods with basis sets of 6-31G., 6-31G*, and 6-31G**. Following their conclusion, we can safely utilize state-averaged CASSCF method abbreviated as SA-N-CAS(n/m), where N refers to the number of states included in the average, while N(=2), n(=2), and m(=2) are the number of active electrons and orbitals, respectively. This means that just π and π^* orbitals corresponding to HOMO and LUMO are involved in CASSCF calculation. Molcas 7.5 [66] program packages were employed for all calculations.

We have first used SA-2-CAS(2/2)/6-31G method to reproduce geometries of conical intersection OBF-CI, the local minima on S_0 and S_1 potential energy surfaces given by [45]. Then, we concentrate on configuration of conical intersection at which the torsion angle D1 (C11-C8-C1-C2) and dihedral angle D2 (H10-C8-C1-H9) are −146.6° and −60.0°, respectively, as shown in Figure 1. We have carried out a preliminary test calculation for two-dimensional potential energy surfaces with variables D1 and D2 (all bond lengths, all bond angles, and the other dihedral angles are fixed at OBF-CI configuration). We found that DD1 = (D1 + D2)/2 and DD2 = (D2 − D1)/2 are better variables to describe the isomerization. If we set up interesting region for potential energy surface S_1 with energy not higher than 5 eV above OBF-CI (where it is considered as zero point of potential energy), DD2 can be chosen as in [−20°, 90°] and DD1 is chosen as in [0°, −180°] that is sufficient to describe the present isomerization process. We use equal spacing 5° for grid points: DD1 is 0, −5, . . . , −180 (37 grid points) and DD2 is −20, −15, . . . , 90 (23 grid points). Total configurations are 851 plus OBF-CI which all are computed by SA-2-CAS(2/2)/6-31G method, and then all *ab. initio* data are fitted into analytical function of potential energy surfaces by the least square method from Matlab 7.5 package [67]. Finally, we have adiabatic potential energy surfaces in the analytical form:

$$\begin{aligned} W(x,y) = {} & c_0 \exp\left[-a_1(x-x_0)^2 - b_1(y-y_0)^2\right] \\ & + c_1 \cos\left(\frac{x}{2}\right) + c_2 \cos\left(\frac{y}{2}\right) + c_3 \cos(x) \\ & + c_4 \cos(y) + c_5 \cos(2x) + c_6 \cos(2y) \\ & + c_7 \cos(3x) + c_8 \cos(3y) + c_9 \sin\left[\frac{x+y}{2}\right] \\ & + c_{10} \sin\left[\frac{2x+y}{2}\right] + c_{11} \sin\left[\frac{x+2y}{2}\right] \\ & + c_{12} \sin(x+y) + c_{13} \sin(2x+y) \\ & + c_{14} \sin(x+2y) + c_{15} \sin(2x+2y) \\ & + c_{16} \sin(3x+y) + c_{17} \sin(x+3y) \\ & + c_{18} \sin(3x+2y) + c_{19} \sin(2x+3y) \\ & + c_{20} \sin(3x+3y) + c_{21} \cos\left[\frac{x+y}{2}\right] \\ & + c_{22} \cos\left[\frac{2x+y}{2}\right] + c_{23} \cos\left[\frac{x+2y}{2}\right] \end{aligned}$$

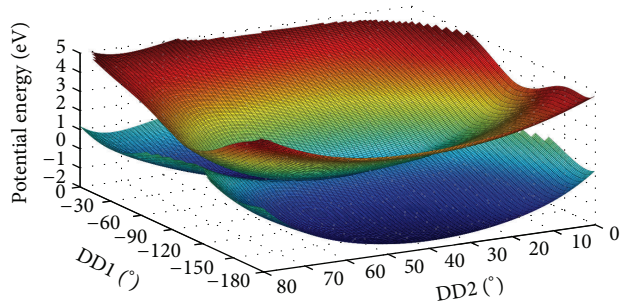

Figure 2: Analytical two-dimensional PESs for the ground state S_0 and the first excited state S_1 with respect to the combined internal angles DD1 and DD2 [33].

$$
\begin{aligned}
&+ c_{24}\cos(x+y) + c_{25}\cos(2x+y)\\
&+ c_{26}\cos(x+2y) + c_{27}\cos(2x+2y)\\
&+ c_{28}\cos(3x+y) + c_{29}\cos(x+3y)\\
&+ c_{30}\cos(3x+2y) + c_{31}\cos(2x+3y)\\
&+ c_{32}\cos(3x+3y),
\end{aligned}
\tag{8}
$$

where x = DD1 and y = DD2, $x_0 = -103.3^\circ$ and $y_0 = 43.3^\circ$ are angles at OBF-CI. The fitting parameters a_1, b_1, and c_0 to c_{32} are all given in Table 1. Potential energy surfaces of S_0 and S_1 calculated from (8) are plotted in Figure 2 with zero point of potential energy at $W(x_0, y_0) = 0$ in a unit of electron volt. We computed the mean absolute error between calculated results from (8) and numerical data computed from method SA-2-CAS(2/2)/6-31G for about 100 randomly picked up configuration points and we found that this error is about 2.4 kcal/mol for the both potential energy surfaces, and less than 1.0 kcal/mol around OBF-CI region. From analytical PES in (8), we have estimated local trans-isomer at DD1 = -164.3° and DD2 = 36.7° with energy 1.72 eV below OBF-CI, and local cis-isomer at DD1 = -39.2° and DD2 = 50.9° with energy 1.28 eV below OBF-CI. Furthermore, the vertical excitation energies have been calculated to be 4.11 eV and 4.45 eV at local trans- and cis-minima, respectively, which are accidently in consistence with the experimental measurement 4.13 eV and 4.59 eV [68]. We confirmed that a global minimum of S_1 state is just right at conical intersection for the present two-dimensional potential energy surface.

2.3. TSH Scheme for LZ and ZN Methods. Section 2.1 implements classical trajectory simulation on a single potential energy within the Cartesian coordinate system plus constraints in internal coordinate systems. This not only simplified numerical calculation for integration of classical trajectory in molecular Hamiltonian but also avoided searching complicated form of kinetic operators in internal coordinates. However, nonadiabatic transition between two PESs is completely quantum effects, and it requires explicit form of the kinetic operators to calculate nonadiabatic coupling vector between two PESs. We focus on the torsion angle D1 and

Table 1: The coefficients in (1) for two-dimensional S_0 and S_1 PESs around one-bond flip conical intersection (OBF-CI) ($c_0 \sim c_{32}$ in units of eV) [33].

Index	a_1	b_1	c_0	c_1	c_2
S_0	35	3.5	0.495231	364.2436	166.2537
S_1	39	3.9	−0.52219	256.2847	−18.8715
Index	c_3	c_4	c_5	c_6	c_7
S_0	−63.2233	−228.305	−12.7773	25.79321	−3.78713
S_1	−74.255	−85.6398	−4.51131	16.61385	−1.65933
Index	c_8	c_9	c_{10}	c_{11}	c_{12}
S_0	−3.97288	9.467412	106.3829	−36.167	−72.9472
S_1	−2.44485	−219.158	171.3529	98.32809	−110.789
Index	c_{13}	c_{14}	c_{15}	c_{16}	c_{17}
S_0	5.205437	−0.08421	−4.58729	5.134825	3.857498
S_1	9.156298	−4.96308	−1.1299	0.059523	4.654567
Index	c_{18}	c_{19}	c_{20}	c_{21}	c_{22}
S_0	−6.20916	0.171133	2.090849	−538.156	−56.4412
S_1	−1.20414	−1.73863	0.658395	−277.529	87.56788
Index	c_{23}	c_{24}	c_{25}	c_{26}	c_{27}
S_0	254.7531	157.3086	17.19558	−58.19	−8.161
S_1	112.7934	47.53832	−7.42468	−41.5302	7.965267
Index	c_{28}	c_{29}	c_{30}	c_{31}	c_{32}
S_0	7.267131	4.132838	−3.08607	1.734321	0.088946
S_1	1.25399	3.375719	−0.42815	−0.71119	−0.09718

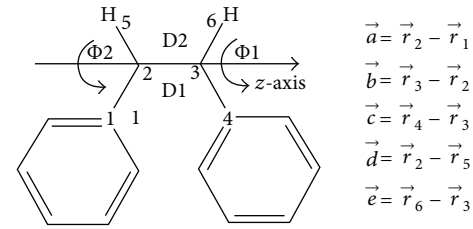

Scheme 1

dihedral angles D2 (transferred into DD1 and DD2 for PESs depicted in Figure 2) and also present the following regular form of kinetic operators explained in Scheme 1, with

$$
T = -\frac{\hbar^2}{2I_{\mathrm{D1}}}\frac{\partial^2}{\partial \mathrm{D1}^2} - \frac{\hbar^2}{2I_{\mathrm{D2}}}\frac{\partial^2}{\partial \mathrm{D2}^2},
\tag{9}
$$

where the dihedral angle D1 represents the relative torsion motion between two phenyl rings and the D2 represents the relative torsion motion between two hydrogen atoms. We assume that atoms 2 and 3 are fixed and two phenyl rings and two hydrogen atoms rotate on the circles around z-axis as shown in Scheme 1. For instance, we can think that $\Phi 1$ and $\Phi 2$ are rotation angles around z-axis for two phenyl rings, respectively. Thus, the moment of inertia I_{D1} is the reduced inertia from two phenyl rings

$$
I_{\mathrm{D1}} = \frac{I_{\Phi 1} I_{\Phi 2}}{I_{\Phi 1} + I_{\Phi 2}},
\tag{10}
$$

where $I_{\Phi 1} = \sum_i m_i \rho_i^2$ (m_i is atom mass in the one phenyl ring and ρ_i is distance from atom i to z-axis) and $I_{\Phi 2}$ is estimated

from the other phenyl ring. The same analysis can be applied for the moment of inertia I_{D2} with two hydrogen atoms:

$$I_{D2} = \frac{I_{H1} I_{H2}}{I_{H1} + I_{H2}}, \tag{11}$$

where $I_{H1} = m_H \rho_H^2$ (m_H is hydrogen atom mass and ρ_H is distance from hydrogen atom H to z-axis) and I_{H2} is estimated from the other hydrogen atom.

One-passage semiclassical nonadiabatic transition probability (LZ and ZN formulas) can be calculated just from two adiabatic potential energy surfaces along the seam if we have the regular kinetic form of (9):

$$p_{LZ} = \exp\left(-\frac{\pi}{4\sqrt{a^2 |b^2|}}\right), \tag{12}$$

$$p_{ZN} = \exp\left(-\frac{\pi}{4\sqrt{a^2 |b^2|}} \sqrt{\frac{2}{1 + \sqrt{1 + (0.4a^2 + 0.7) b^{-4}}}}\right), \tag{13}$$

where calculation of two parameters a^2 and b^2 is given in Appendix B.

We can simply look at the present two-dimensional PESs in Figure 2 to find that the seam line is appearing at the DD1 = −103.3°. Seam line is defined as the trace of local minimum gap between two adiabatic PESs [69]. However, in the present work we propose to calculate the local maxima of the effective coupling parameter a^2 as introduced in Appendix C. Once the seam line is found, the nonadiabatic coupling vector is assumed to be perpendicular to the seam line and it appears in DD1 direction in the present case. Therefore, the effective collision energy parameter b^2 is calculated along the DD1 direction and it means that only angular momentum related to DD1 is changed during the trajectory surface hopping. After trajectory hopping from one potential energy surface to another, we need to redistribute this angular momentum change into six atoms (see Scheme 1) in the Cartesian coordinate systems and the detailed procedure is given in Appendix C.

The calculation shows that the seam line appears at DD1 = −103.3° with negligible dependence of DD2 angle. The effective coupling parameter a^2 along the seam line is calculated and depicted in Figure 3. Figure 3 shows that the diabatic region (where the one-passage transition probability is almost unity) is located in between 41° and 49° for angle DD2. The other region of DD2 belongs to effective nonadiabatic transition zone, especially for DD2 in between [9°, 39°] and [57°, 80°] where it is a strong nonadiabatic transition zone with $0.1 \leq a^2 \leq 10$.

3. Results and Discussions

Experimental measurement starts from global cis-minimum and trans-minimum in which photoisomerization processes involve dynamics on full-dimensional potential energy surfaces. We construct the reduced two-dimensional (2D)

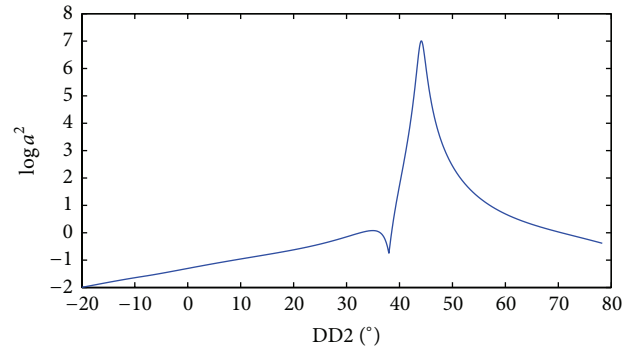

Figure 3: The effective coupling parameter a^2 along the seam line with DD1 = −103.3°.

potential energy surfaces at OBF-CI, and S_0 potential energy surface shows clear local cis-minimum and trans-minimum separated by the seam line. We assume that trajectory starts from global cis (trans)-minimum with photo-excitation from S_0 to S_1 PES and then reaches the certain area of the present local cis (trans)-minimum on the 2D S_1 PES, from where trajectories start isomerization. Then, question is how to determine such area for both local cis- and trans-isomers. Let us start with the test local cis-area and local trans-area in rectangular region of [−19.2° < DD1 < −59.2°, 30.9° < DD2 < 70.9°] and [−180.0° < DD1 < −144.3°, 16.7° < DD2 < 56.7°], respectively, for both initial and final conditions of trajectories. Total energy for cis-to-trans isomerization is defined by the excitation energy 4.45 eV from S_0 to S_1 state estimated at local cis-minimum (DD1 = −39.2°, DD2 = 50.9°). The initial conditions of DD1 and DD2 for trajectories are randomly picked up in the local cis-area vertically excited from S_0 to S_1 state; if this trajectory has vertical excitation energy which is larger than 4.45 eV, it is abandoned, and if this trajectory has vertical excitation energy which is smaller than 4.45 eV, it can be proceeded. Then, we specify initial kinetic energy for proceeding trajectory with Scheme 1 by choosing atoms 1, 4, 5, and 6 with nonzero velocities and all atoms in molecule with zero velocities. The proceeding trajectory which starts from local cis-area on S_1 state can have three ending ways; one is that it enters local cis-area on S_0 (called cis-to-cis nonreactive trajectory), another is that it enters local-trans area on S_0 (called cis-to-trans reactive trajectory), and the third is that it enters outside of 2D PES boundary region depicted in Figure 2; for instance, DD1 is smaller than −180° or larger than 0° (called unreactive trajectory). An unreactive trajectory is due to that 2D PES has periodic properties in terms of DD1 and DD2 angles and we do count it as nonreactive trajectory.

Now we present how to distribute a given kinetic energy T_{init} to atoms 1, 4, 5, and 6 with their initial velocities analyzed in the following. As shown in Scheme 1, the z-component of velocity is assumed to be zero so that for a given kinetic energy T_{init}, we have the following relations:

$$\begin{aligned} \frac{1}{2} m_1 \left(\dot{x}_1^2 + \dot{y}_1^2 + \dot{x}_4^2 + \dot{y}_4^2\right) &= T_{init}\delta, \\ \frac{1}{2} m_5 \left(\dot{x}_5^2 + \dot{y}_5^2 + \dot{x}_6^2 + \dot{y}_6^2\right) &= T_{init}(1 - \delta), \end{aligned} \tag{14}$$

Table 2: Branching ratios (numbers in parentheses are calculated from Landau-Zener formula) for cis-to-trans and trans-to-cis isomerizations at one-bond flip conical intersection (OBF-CI).

OBF-CI[a]	Initial from cis-area		Initial from trans-area	
Number of trajectories	Cis-area (%)	Trans-area (%)	Trans-area (%)	Cis-area (%)
100	46 (45)	54 (55)	46 (46)	54 (54)
500	35.4 (35.4)	64.6 (64.6)	47 (50)	53 (50)
1000	33 (36)	67 (64)	47 (49)	52.6 (50.7)
2000	33.4 (37)	66.6 (63)	47.8 (48.4)	52.2 (51.6)
Exp.[b]	50	50	50	50

[a]Total energy of each classical trajectory is set up to the vertical excitation energy 4.45 eV at cis-area and 4.11 eV at trans-area.
[b]References [59, 61].

where δ is random number in the range of [0, 1] and m_1 (m_5) is mass of carbon (hydrogen) atom. The x and y-components of velocities in (14) must satisfy

$$x_1\dot{x}_1 + y_1\dot{y}_1 = 0, \qquad x_4\dot{x}_4 + y_4\dot{y}_4 = 0,$$
$$x_5\dot{x}_5 + y_5\dot{y}_5 = 0, \qquad x_6\dot{x}_6 + y_6\dot{y}_6 = 0, \tag{15}$$

because of constraints of bond lengths and bond angles. Moreover, we choose the angular moment along z-axis for atoms 1 and 4 and for atoms 5 and 6 as follows:

$$\left(x_1\dot{y}_1 - y_1\dot{x}_1\right) + \left(x_4\dot{y}_4 - y_4\dot{x}_4\right) = 0,$$
$$\left(x_5\dot{y}_5 - y_5\dot{x}_5\right) + \left(x_6\dot{y}_6 - y_6\dot{x}_6\right) = 0. \tag{16}$$

This means that angular momentum along z-axis for the twist of atoms 1 and 4 is cancelled out from each other, so does for atoms 5 and 6. Equations (14), (15), and (16) all together have the eight related equations for the eight velocity components to be determined. However, the above procedure slightly violates conservation of total energy because two phenyl rings associated with atoms 1 and 4 in Scheme 1 can have induced velocities through the constraints for entire molecule. We can resolve this problem by choosing smaller kinetic energy T_{init} in (14) than the previously specified one, and this can be obtained by subtracting induced kinetic energy from two phenyl rings. Of course, this has to be done iteratively with the constraint Hamiltonian equations (1) and (2) in the first step of classical trajectory integration.

We can do the same as mentioned above for trans-to-cis isomerization, and the total energy is defined by the excitation energy 4.11 eV from S_0 to S_1 state estimated at local trans-minimum (DD1 = –164.3°, DD2 = 36.7°). The initial conditions of DD1 and DD2 for trajectories are randomly picked up in the local trans-area vertically excited from S_0 to S_1 state. Three types of ending trajectories are also collected as mentioned above (trans-to-trans nonreactive, trans-to-cis reactive, and unreactive trajectories which is classified as nonreactive). All numerical calculations are performed within the atomic unit. We use our own code for solving the constraint Hamiltonian equations and integration for classical trajectory in combination with the free MINPACK code [70] which contains Powell's Dog Leg method [71] for solving the nonlinear equation solution.

For given initial coordinates and corresponding conjugate moments, we integrate (1) and (2) with initial the Lagrange multipliers $\lambda_k(t) = 0$. Then, outcome of coordinates is inserted into the Jacobian determinant $J_{kk'}$ in (7) to have the new $\lambda_k(t)$ that are inserted into (1) and (2) again. We do this iteratively until all Lagrange multipliers converge together with the update coordinates and momentums. For the second step of integration, the Lagrange multipliers are set up as the previous values, and in this way, we propagate trajectory until it ends with use of the fourth-order Runge-Kutta method (RK4) [72] by equal time step size 2.07 a.u. (about 0.05 fs).

Classical trajectory is propagated on a single adiabatic potential energy surface all the time. However, once trajectory is across the seam line, we compute effective coupling a^2 and effective collision energy b^2 according to the method given in Appendix C. Then, we can evaluate one-passage nonadiabatic transition probability by (12) and (13). We obtain the seam line by calculating local minima of effective coupling a^2 and found that they all are located at avoided crossing points. Comparing p with random number in between 0 and 1, we decide to hop trajectory from one adiabatic potential energy surface to another if p is larger than the random number; otherwise, it stays in the original potential energy surface. As trajectory hops to the other PES vertically, and it means that all coordinates are unchanged, but the moments are changed with method introduced in Appendix C.

3.1. Branching Ratios of Cis-to-Trans and Trans-to-Cis Isomerizations. By giving equal weight to all the sampling trajectories, we compute the branching ratios with initial condition starting from both local cis-area and local trans-area. We carry out trajectory surface hopping simulation with number of trajectories 100, 500, 1000, and 2000, respectively, in order to check convergence of the branching ratios. The results in Table 2 show that the results are basically converged at 500 trajectories. The branching ratio for trans-to-cis isomerization is 48 : 52 (experimental value is 50 : 50) in the present simulation. By considering a potential barrier in Frank-Condon region of global trans-minimum which is taking 5% trajectories down to global trans-minimum by fluorescence [59, 61], we can estimate the quantum fields for trans-to-cis isomerization as 0.95 × 52% = 49% which is in very good agreement with the experiment measurement 55.0%. The branching ratio for cis-to-trans isomerization is

33 : 67 (experimental value is 50 : 50) in the present simulation. There are two pathways when Stilbene is photo-excited from the global cis-isomer S_0 to S_1 state (see [59, 61] and references therein); one pathway leads to the OBF-CI with branching ratio 70% and another goes to the other conical intersection (branching ratio 30%) which is for side reaction of a ring closing to form DHP. If we take this branching ratio into consideration, we can estimate the quantum yield for cis-to-trans isomerization as $0.7 \times 67\% = 47\%$ which is larger than experimental measurement with 35%. The present simulation shows isomerization in favor of reactive trajectories regardless of initial starting from local trans-area or local cis-area and this means that branching ratio is not 50 : 50 at OBF-CI.

Potential energy surface of S_1 state as shown in Figure 2 is down to hill much faster in DD1 direction than in DD2 direction, and thus in the average, speed of trajectory is much faster in DD1 direction than in DD2 direction. This means that effective collision energy b^2 is well above the seam and this makes trajectory have a big chance to hop down S_0 state in the first time to cross the seam line. This is why the branching ratio is in favor to reactive isomerization and both LZ and ZN formulas present the same results in Table 2. Meanwhile, initial vertical excitation energy is 3.17 eV above OBF-CI at cis-area and is 2.39 eV above OBF-CI at trans-area, so that effective collision energy b^2 is higher for cis-to-trans than for trans-to-cis. This explains why branching ratio is more in favor of reactive cis-to-trans than trans-to-cis. We know that the conical intersection Hula-Twist (HT-CI) is higher in energy than in OBF-CI, and these two CIs might be in close configuration. Therefore, we suspect that there is a big chance for cis-to-trans trajectory to access HT-CI with high vertical excitation energy, but this is not the case for trans-to-cis trajectory with low vertical excitation energy.

We have also tested how branching ratios are sensitive to choice of size of trans- and cis-area, and we found that they are not so sensitive to the choice of the area size unless we define very small area for cis-area and trans-area. This smallness is not reasonable because trajectory takes quite long time to reach local cis (trans)-area from global cis (trans)-isomer; it should have a chance to distribute in relatively large area as we tested above. We check sensitivity of branching ratios with respect to the slight change of seam line with DD1 = −103.25 and DD1 = −103.35, and we found that the results in Table 2 still stand. This is because effective coupling and collision energy parameters (a^2 and b^2) are quite robust in the present formulation.

3.2. Detailed Analysis of Typical Classical Trajectories. It is interesting to look at a typical trajectory to analyze how isomerization is taking place. Figure 4 shows how a reactive trajectory for cis-to-trans isomerization varies with time by starting at local cis-area with photo-excitation energy 4.42 eV and total evolution time is 115 fs. Four snapshots of structure varying with time are shown in Figure 4(a); it can be seen that potential energy steeply decreases on S_1 state and increases on S_0 state with crossing seam line around 52 fs first and then crossing again shortly, but no hopping occurs due to the fact that nonadiabatic transition probability is smaller than random number there. Trajectory hopping from S_1 to S_0 state occurs at 80 fs where DD1 and DD2 are almost at conical configuration (where transition probability is almost a unit). After hopping, the trajectory ends at local trans-area at 115 fs. Figure 4(b) shows that both DD1 and DD2 angles change with oscillation against time; DD1 drops considerably while DD2 keeps almost constant oscillation. It would be interesting to see original torsion angle D1 and dihedral angle D2 varying with time as shown in Figure 4(c). Figure 4(c) shows that the torsion angle D1 decreases monotonically from −100.0° (at local cis-area) to −185° (at local trans-area), and this is exactly corresponding to what it is called as one-bond flip process around the central C=C bond. Dihedral angle D2 decreases from the beginning at 7.5° to the end at −95° with three-circle oscillations. This is because light hydrogen atoms move much faster than heavy phenyl rings. The oscillation of D2 angle can be explained by its coupling with D1, when the terminal atoms of D2 are moving close to the terminal atoms of D1, leading to a large steric hindrance, and then far away from them periodically. These results provide the evidence that the electronically nonadiabatic transition would be dominated by the phenyl ring twist around the central double bond.

Figure 5 shows how a reactive trajectory for trans-to-cis isomerization varies with time by starting at local trans-area with photo-excitation energy 3.98 eV and evolution time is 133 fs. Potential energies on S_0 and S_1 states vary with time with four selected snapshots of structure as shown in Figure 5(a) for a reactive trans-to-cis trajectory. There are three-time surface hopping from one potential energy surface to another during evolution of trajectory; the first hopping from S_1 to S_0 state happened at 50 fs, the second hopping from S_0 to S_1 state at 71 fs, and the last hopping from S_1 to S_0 state at 88 fs. After that, the trajectory is propagated on S_0 state until its end at 133 fs. Figure 5(b) shows that both DD1 and DD2 angles change with oscillation against time; DD1 rises considerably while DD2 keeps almost constant oscillation. Figure 5(c) shows that the torsion angle D1 increases monotonically from −188° (at local trans-area) to −97° (at local cis-area), and this shows one-bond flip picture around the central C=C bond again. Dihedral angle D2 increases from the beginning at −128° to the end at −5° with four-circle oscillations. The reactive trans-to-cis trajectory in Figure 5 evolutes longer time period than that of reactive cis-to-trans trajectory in Figure 4.

With randomly choosing 100 initial conditions as mentioned before in both trans-area and cis-area, we have sampled 100 independent trajectories to analyze how these swarm of trajectories evolve in average. We plot DD1 and DD2 angle changes against time for these 100 trajectories in Figure 6; Figure 6(a) shows the most of trajectories started from cis-area end around 120 fs in average, while Figure 6(b) shows that the most of trajectories started from trans-area end around 200 fs in average which is twice in time compared to trajectories starting from cis-area. This is because the vertical excitation energy for initial condition is 4.45 eV in cis-area and 4.11 eV in trans-area, and thus speed of trajectory along DD1 direction on S_1 state potential energy surface is larger in cis-area than in trans-area. Trajectories starting from cis-area have larger nonadiabatic transition probability to hop than

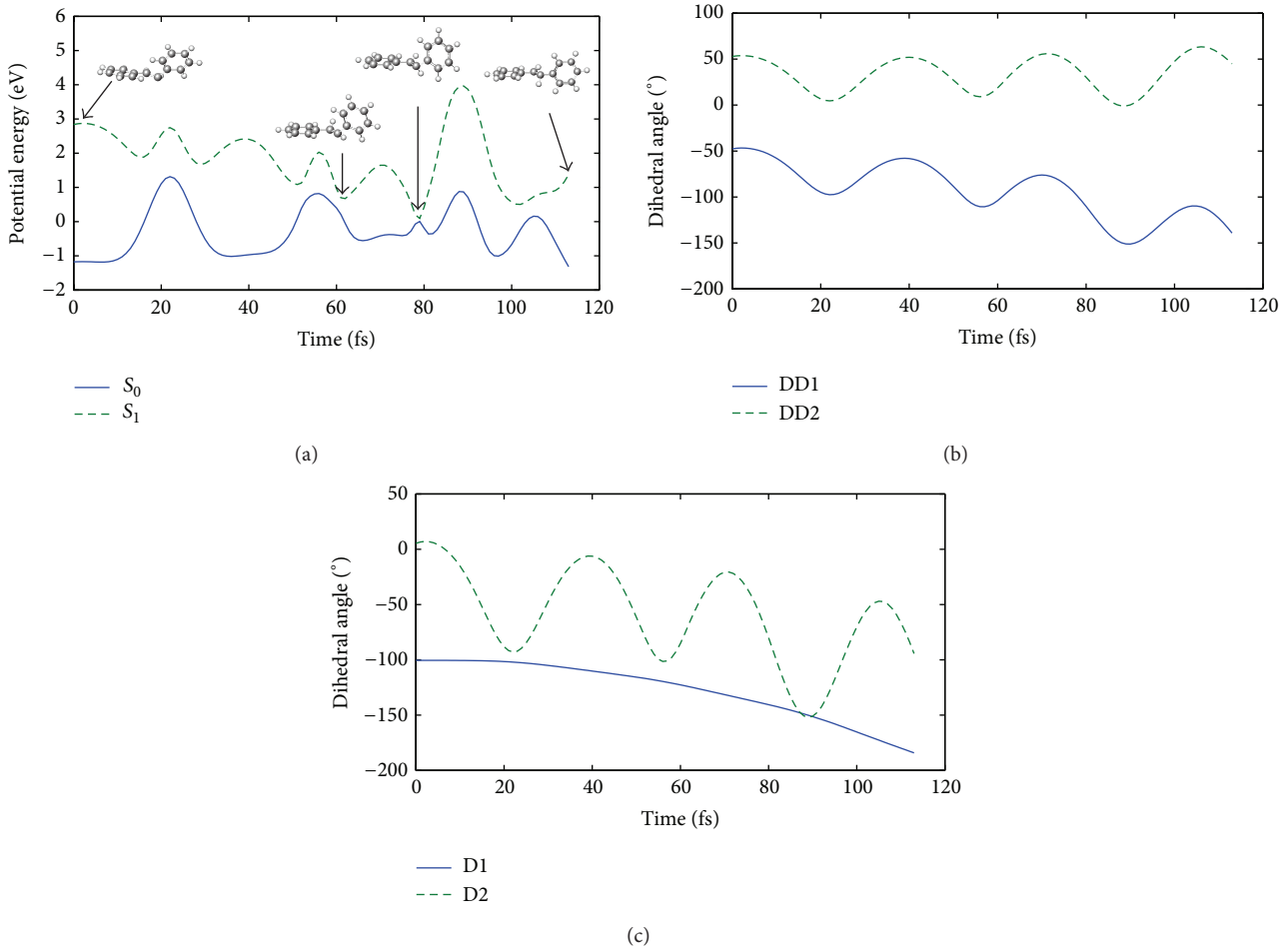

FIGURE 4: A typical reactive trajectory for cis-to-trans isomerization starts from local cis-area with photo-excitation energy 4.42 eV. (a) Snapshots of potential energy surfaces and structures varying with time, (b) DD1 and DD2, and (c) D1 and D2 varying with time.

trajectories starting from trans-area. Figure 6(a) also shows that trajectories start from cis-area hop around 20 fs, 50 fs, and 100 fs, while trajectories start from trans-area shown in Figure 6(b) hop around all times from 20 fs to 200 fs. The number of switching times from one potential energy surface to another is much greater in average for a trajectory staring from trans-area than starting from cis-area. This also explains why the branching ratio at OBF-CI is dependent on initial conditions; 33% (reactant) to 67% (product) for trajectory starting from cis-area and 48% (reactant) to 52% (product) for trajectory starting from trans-area.

4. Concluding Remarks

Trajectory surface hopping with constraint molecular dynamics is proposed to investigate nonadiabatic molecular dynamics with reduced-dimensional on-the-fly or analytical potential energy surfaces, and nonadiabatic transitions at the crossing seam are treated by LZ and ZN formulas. Since nonadiabatic transitions are taking place locally around the seam surfaces, we can probe trajectories around local region with reduced dimensional potential energy surfaces, and furthermore we can divide potential energy surfaces into different regions in which different constraints can be applied. In this way, we extend on-the-fly TSH method to deal with large system for nonadiabatic molecular dynamics. Of course, it goes back to full-dimensional on-the-fly TSH method if there is no constraint.

The present method is immediately applied to trans↔cis isomerization at OBF-CI for Stilbene. Two-dimensional PESs for the ground state and the lowest excited state can be well described by dihedral angles DD1 and DD2, in which the seam line is just right at DD1 = −103.3°. Dihedral angle D1 is corresponding to the twist of two phenyl rings around the central ethylenic C=C bond. The present simulation has shown an exact one-bond flip behaviors of reactive trajectory, in which D1 changes monotonically from reactant to product for both cis-to-trans and trans-to-cis isomerizations. Trajectory surface hopping simulation based on the present two-dimensional potential energy surfaces can present quite quantitative information for isomerization of Stilbene. We have proposed to calculate two effective parameters a^2 and b^2 along trajectory moving on adiabatic potential energy surfaces. Effective coupling parameter a^2 is not only used for determining transition probability but also for determining the seam line; in the present two-dimensional case this is

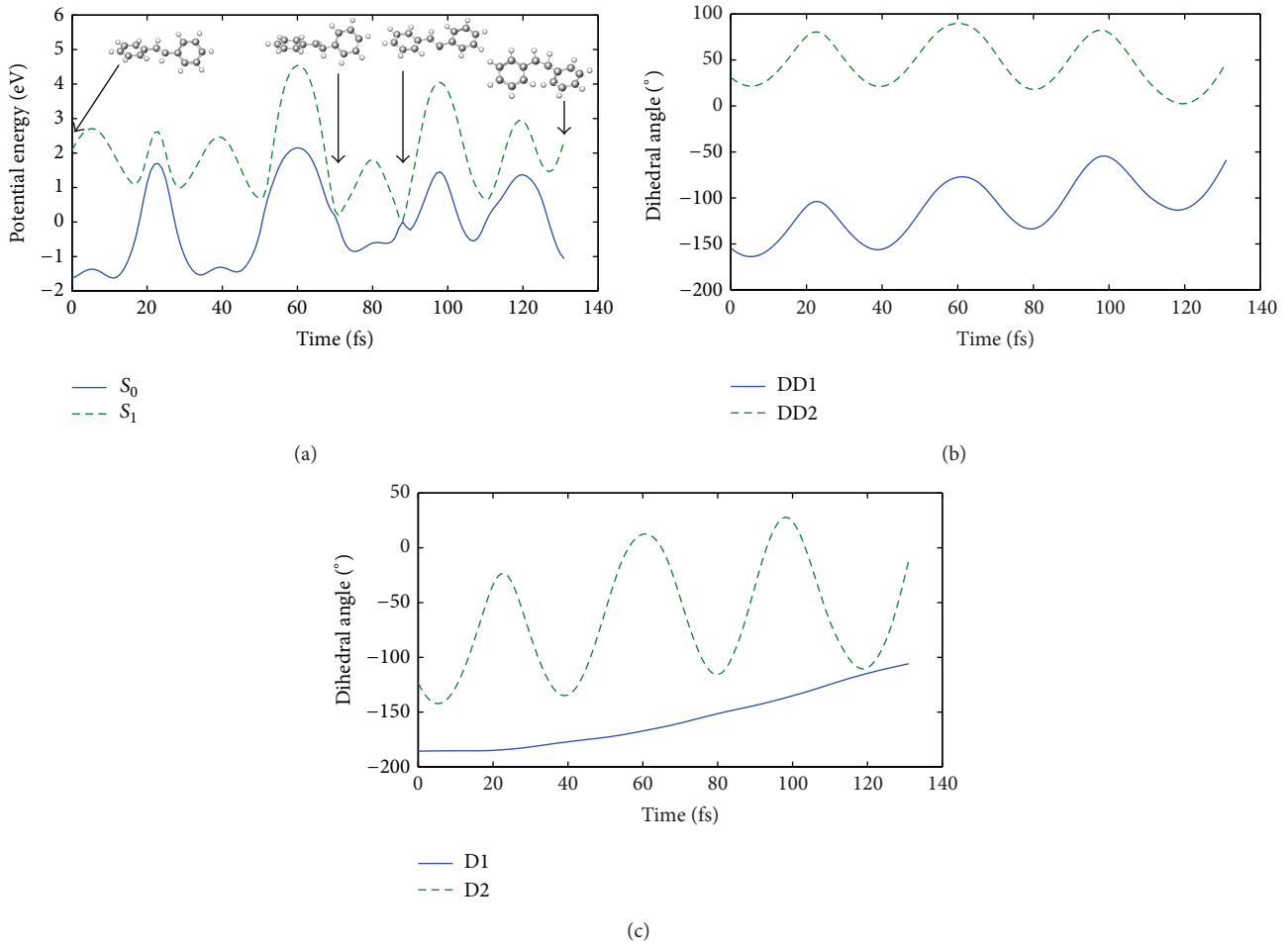

Figure 5: A typical reactive trajectory for trans-to-cis isomerization starts from local trans-area with photo-excitation energy 3.98 eV. (a) Snapshots of potential energy surfaces and structures varying with time, (b) DD1 and DD2, and (c) D1 and D2 varying with time.

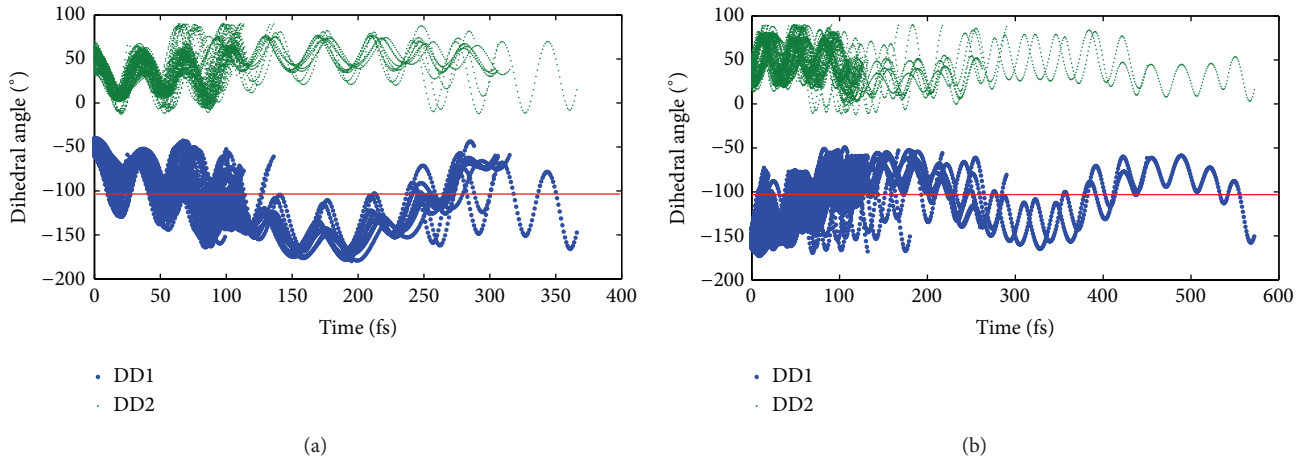

Figure 6: The dihedral angels DD1 and DD2 vary with time for 100 trajectories; (a) and (b) correspond to initially start from cis-area and trans-area, respectively.

similar to the previous work [69]. However, the present method is useful to deal with high-dimensional nonadiabatic molecular dynamics as transition point is determined by local maxima of effective coupling parameter a^2 along evolution of trajectory. We do not need to calculate the seam line which is a very difficult task for high-dimensional case.

The branching ratios of isomerization at OBF-CI have been calculated by setting up initial condition at vertical excitation energy 4.45 eV and 4.11 eV for cis-area and trans-area, respectively, and these two areas are local minima on ground state potential energy surface. Quantum yield for trans-to-cis is estimated as 49% in compare with experimental results of 55%. This means that the OBF-CI is really responsible for trans-to-cis isomerization. On the other hand, quantum yield for cis-to-trans is estimated as 47% in compare with experimental results of 35%. This means that OBF-CI may be just partly responsible for cis-to-trans isomerization. As vertical excitation energy at cis-area is 0.34 eV higher than that at trans-area based on energy at OBF-CI, we expect that there might be a great chance to access (Hula-Twist) HT-CI for cis-to-trans isomerization. In the near future, we should carry out trajectory surface hopping simulation based on potential energy surfaces connecting OBF-CI with HT-CI together. Nevertheless, we conclude that the present simulation is quite encouraged for further investigating on photoisomerization of Stilbene molecule and the present method is very useful in application to the large systems for nonadiabatic molecular dynamics with flexible dimensions of potential energy surfaces.

Appendices

A. Constraint Equations between Cartesian and Internal Coordinates

In order to calculate Jacobian determinant in (7), we need to build up relation equations between Cartesian and internal coordinates for constraint equations. For four atoms plotted in Figure 7, we have relation equations between Cartesian and internal coordinates for bond lengths $d_{k_1k_2}$, bond angles $\theta_{k_1k_2k_3}$, and dihedral angles $\phi_{k_1k_2k_3k_4}$ in the following equations, respectively:

$$g_k^b(q) = q_{k_1k_2}^2 - d_{k_1k_2}^2 = 0, \quad k = 1, \ldots, N_c^b, \tag{A.1}$$

$$g_k^a = \cos\theta_{k_1k_2k_3}\left|\vec{\mu}^a\right|\left|\vec{\nu}^a\right| - \vec{\mu}^a \cdot \vec{\nu}^a = 0, \quad k = 1, \ldots, N_c^a, \tag{A.2}$$

$$g_k^d = \cos\phi_{k_1k_2k_3k_4}\left|\vec{\mu}^d\right|\left|\vec{\nu}^d\right| - \vec{\mu}^d \cdot \vec{\nu}^d = 0, \quad k = 1, \ldots, N_c^d, \tag{A.3}$$

where Cartesian coordinates are $q_{k_1k_2}^2 = (\vec{r}_{k_2} - \vec{r}_{k_1})^2$, $\vec{\mu}^a = \vec{r}_{k_1} - \vec{r}_{k_2}$, $\vec{\nu}^a = \vec{r}_{k_2} - \vec{r}_{k_3}$, $\vec{\mu}^d = \vec{a} \times \vec{b}$, $\vec{\nu}^d = \vec{b} \times \vec{c}$, $\vec{\mu}^d \cdot \vec{\nu}^d = (\vec{a} \times \vec{b}) \cdot (\vec{b} \times \vec{c})$, $\vec{a} = \vec{r}_2 - \vec{r}_1$, $\vec{b} = \vec{r}_3 - \vec{r}_2$, and $\vec{c} = \vec{r}_4 - \vec{r}_3$ and the subscript of each variable is atom number. In terms of the Cartesian coordinate

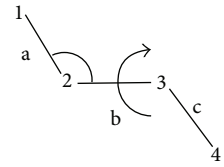

Figure 7: Schematic diagram for relations between Cartesian and internal coordinates for four atoms.

q with the derivations of the constraint equations, equation (5) can be rewritten as

$$\begin{aligned} q_{k_\beta}(t + \Delta t) &= q_{k_\beta}^{\mathrm{uc}}(t + \Delta t) - m_{k_\beta}^{-1}(\Delta t)^2 \left[\sum_{k'=1}^{N_c^b} \lambda_{k'}^b(t) \frac{\partial g_{k'}^b(t)}{\partial q_{k_\beta}(t)} \right. \\ &\quad + \sum_{k'=1}^{N_c^a} \lambda_{k'}^a(t) \frac{\partial g_{k'}^a(t)}{\partial q_{k_\beta}(t)} \\ &\quad \left. + \sum_{k'=1}^{N_c^d} \lambda_{k'}^d(t) \frac{\partial g_{k'}^d(t)}{\partial q_{k_\beta}(t)} \right] \end{aligned} \tag{A.4}$$

in which

$$\begin{aligned} \frac{\partial g_{k'}^b}{\partial q_{k_\beta}} &= \delta_{k_1'k_\beta} \frac{\partial g_{k'}^b(t)}{\partial q_{k_1'}(t)} + \delta_{k_2'k_\beta} \frac{\partial g_{k'}^b(t)}{\partial q_{k_2'}(t)} \\ &= 2\left(\delta_{k_\beta,k_1} - \delta_{k_\beta,k_2}\right)\left(q_{k_1} - q_{k_2}\right), \\ \frac{\partial g_{k'}^a}{\partial q_{k_\beta}} &= \delta_{k_1'k_\beta} \frac{\partial g_{k'}^a(t)}{\partial q_{k_1'}(t)} + \delta_{k_2'k_\beta} \frac{\partial g_{k'}^a(t)}{\partial q_{k_2'}(t)} \\ &\quad + \delta_{k_3'k_\beta} \frac{\partial g_{k'}^a(t)}{\partial q_{k_3'}(t)} \\ &= \left(\delta_{k_1'k_\beta} - \delta_{k_2'k_\beta}\right) \frac{\partial g_{k'}^a}{\partial \mu^a} + \left(\delta_{k_3'k_\beta} - \delta_{k_2'k_\beta}\right) \frac{\partial g_{k'}^a}{\partial \nu^a}, \end{aligned} \tag{A.5}$$

with

$$\begin{aligned} \frac{\partial g_{k'}^a}{\partial \mu_l^a} &= \cos\theta_{k_1k_2k_3} \frac{\left|\vec{\nu}^a\right|}{\left|\vec{\mu}^a\right|} \mu_l^a - \nu_l^a, \\ \frac{\partial g_{k'}^a}{\partial \nu_l^a} &= \cos\theta_{k_1k_2k_3} \frac{\left|\vec{\mu}^a\right|}{\left|\vec{\nu}^a\right|} \nu_l^a - \mu_l^a, \\ \frac{\partial g_{k'}^d}{\partial q_{k_\beta}} &= \delta_{k_1'k_\beta} \frac{\partial g_{k'}^d(t)}{\partial q_{k_1'}(t)} + \delta_{k_2'k_\beta} \frac{\partial g_{k'}^d(t)}{\partial q_{k_2'}(t)} \\ &\quad + \delta_{k_3'k_\beta} \frac{\partial g_{k'}^d(t)}{\partial q_{k_3'}(t)} + \delta_{k_4'k_\beta} \frac{\partial g_{k'}^d(t)}{\partial q_{k_4'}(t)} \end{aligned}$$

$$
\begin{aligned}
&= \begin{bmatrix} \dfrac{\partial g^d_{k'}}{\partial \mu^d_m} & \dfrac{\partial g^d_{k'}}{\partial \mu^d_n} \end{bmatrix} \\
&\cdot \begin{bmatrix} q_{n,k'_3k'_2} & q_{n,k'_1k'_3} & q_{n,k'_2k'_1} \\ -q_{m,k'_3k'_2} & -q_{m,k'_1k'_3} & -q_{m,k'_2k'_1} \end{bmatrix} \cdot \begin{bmatrix} \delta_{k'_1k_\beta} \\ \delta_{k'_2k_\beta} \\ \delta_{k'_3k_\beta} \end{bmatrix} \\
&+ \begin{bmatrix} \dfrac{\partial g^d_{k'}}{\partial \nu^d_m} & \dfrac{\partial g^d_{k'}}{\partial \nu^d_n} \end{bmatrix} \\
&\cdot \begin{bmatrix} q_{n,k'_4k'_3} & q_{n,k'_2k'_4} & q_{n,k'_3k'_2} \\ -q_{m,k'_4k'_3} & -q_{m,k'_2k'_4} & -q_{m,k'_3k'_2} \end{bmatrix} \cdot \begin{bmatrix} \delta_{k'_2k_\beta} \\ \delta_{k'_2k_\beta} \\ \delta_{k'_2k_\beta} \end{bmatrix}, \\
& q_{l,k'_\alpha k'_\beta} = q_{l,k'_\alpha} - q_{l,k'_\beta}, \\
& (lmn) = (123), (231), (312) \\
&\quad = (xyz), (yzx), (zxy).
\end{aligned} \tag{A.6}
$$

For dihedral angles, we have

$$
\begin{aligned}
\frac{\partial g^d_{k'}}{\partial \mu^d_l} &= \cos\phi_{k_1k_2k_3k_4} \frac{\left|\nu^d\right|}{\left|\mu^d\right|} \mu^d_l - \nu^d_l, \\
\frac{\partial g^d_{k'}}{\partial \nu^d_l} &= \cos\phi_{k_1k_2k_3k_4} \frac{\left|\mu^d\right|}{\left|\nu^d\right|} \nu^d_l - \mu^d_l.
\end{aligned} \tag{A.7}
$$

Finally, Jacobian determinants in (7) are given as

$$
\begin{aligned}
J_{kk'} = \frac{\partial g^p_k(t+\Delta t)}{\partial \lambda^p_{k'}(t)} &= \sum_{i=1}^{N}\sum_{l=1}^{3} \left[\frac{\partial g^p_k(t+\Delta t)}{\partial q_{l,i}(t+\Delta t)} \frac{\partial q_{l,i}(t+\Delta t)}{\partial \lambda^p_{k'}(t)} \right] \\
&= \sum_{i=1}^{N}\sum_{l=1}^{3} \left[\frac{\partial g^p_k(t+\Delta t)}{\partial q_{l,i}(t+\Delta t)} \frac{\partial g^p_{k'}(t)}{\partial q_{l,i}(t)} \right],
\end{aligned} \tag{A.8}
$$

where N = total atom number and $l = x, y, z$.

B. Unified One-Passage Semiclassical Nonadiabatic Transition Probability

A unified one-passage semiclassical nonadiabatic transition probability was derived analytically as [73]

$$
p = \frac{\sinh[(d-1)\delta]}{\sinh(d\delta)} \exp(-\delta), \tag{B.1}
$$

where d represents the ratio between adiabatic and diabatic potential energy gaps at transition point R_0:

$$
d = \left[\frac{W_+(R_0) - W_-(R_0)}{V_2(R_0) - V_1(R_0)} \right]^2, \tag{B.2}
$$

where W_+ and W_- correspond to the excited state (upper state) and the ground state (lower state), while V_2 and V_1 are diabatic potential energy surfaces. The adiabatic parameter δ that measures nonadiabatic transition strength is expressed in terms of the complex phase integrals:

$$
\begin{aligned}
\delta = \operatorname{Im} \frac{1}{\hbar} \int_{R_0}^{R^*} &\left[\sqrt{2m\left(E - W_-(R)\right)} \right. \\
&\left. - \sqrt{2m\left(E - W_+(R)\right)} \right] dR,
\end{aligned} \tag{B.3}
$$

in which $W_+(R^*) = W_-(R^*)$ at the complex crossing point R^* (its real part R_0 stands for transition point), m is reduced mass of system, and E is collision energy. In order to apply the above formula to multidimensional case, we generalize (B.3) in terms of adiabatic potential energy surfaces at the transition point R_0. Applying the exponential model (see (2.20) of [41]), we can convert (B.3) into

$$
\begin{aligned}
\delta = &\frac{\pi\sqrt{2m}(\Delta E_0)^2}{\hbar(\partial/\partial x)[W_+(R) + W_-(R)]\big|_{R=R_0}} \\
&\times \frac{1}{\sqrt{E - E_0}} \frac{1}{1 + \sqrt{1 + \Delta E_0/(E - E_0)\sqrt{d}}},
\end{aligned} \tag{B.4}
$$

where

$$
\begin{aligned}
\Delta E_0 &= \frac{W_+(R_0) - W_-(R_0)}{2}, \\
E_0 &= \frac{W_+(R_0) + W_-(R_0)}{2}.
\end{aligned} \tag{B.5}
$$

It should be noted that (B.4) is exact for the exponential model and it becomes an approximation when it is generalized to the general two-state system. In comparison with the Landau-Zener transition formula in (12), we can decompose the adiabatic parameter δ into the following two diabatic parameters:

$$
a^2 = \frac{\hbar^2}{16m} \frac{1}{(\Delta E_0)^3} \left[\frac{\partial}{\partial R} \left[W_+(R) + W_-(R) \right]\big|_{R=R_0} \right]^2, \tag{B.6}
$$

$$
b^2 = \frac{E - E_0}{2\Delta E_0} \left[\frac{1}{2} + \frac{1}{2} \sqrt{1 + \frac{\Delta E_0}{(E - E_0)\sqrt{d}}} \right]^2. \tag{B.7}
$$

Equations (B.6) and (B.7) are similar to the expressions derived by Zhu and Nakamura [3], but adiabatization form is much simpler. An effective coupling parameter a^2 in (B.6) is very useful to determine nonadiabatic transition zone and the seam surface for multidimensional potential energy surfaces, and an effective collision energy b^2 in (B.7) has an finite value at $E = E_0$. The parameter d defined in (B.2) which represents general type of nonadiabatic transition is only included in (B.7) for the effective collision parameter.

C. The Two Diabatic Parameters and Trajectory Surface Hopping along the Seam Surface

C.1. The Effective Coupling a^2 and the Seam Line. The effective coupling parameter a^2 in (B.6) is defined along the certain one-dimensional direction, and the best direction is represented by the nonadiabatic coupling vector. However, we know that the direction perpendicular to the seam surface can be approximately considered as the direction of the nonadiabatic coupling vector. The seam surface can be calculated from two adiabatic potential energy surfaces without knowing any information of nonadiabatic coupling [69], in which the method requires to solve the certain partial differential equation. This is not easy to be generalized to the high-multidimensional case. We propose in the present work to calculate the local maxima of the effective coupling parameter a^2, and then the collection of all the local maxima constructs the seam surface. The kinetic part of Hamiltonian in terms of two dihedral angles D1 and D2 as shown in (9) can be rewritten as

$$\begin{aligned} T &= -\frac{\hbar^2}{2I_{\mathrm{D1}}}\frac{\partial^2}{\partial \mathrm{D1}^2} - \frac{\hbar^2}{2I_{\mathrm{D2}}}\frac{\partial^2}{\partial \mathrm{D2}^2} \\ &= -\frac{\hbar^2}{2I}\left(\frac{\partial^2}{\partial x^2} + \frac{\partial^2}{\partial y^2}\right), \end{aligned} \tag{C.1}$$

where $I = \sqrt{I_{\mathrm{D1}} I_{\mathrm{D2}}}$ is the reduced moment of inertia that corresponds to the reduced mass required in (B.6). The variables x and y are given by

$$\begin{pmatrix} x \\ y \end{pmatrix} = \begin{pmatrix} c_1 & 0 \\ 0 & c_2 \end{pmatrix} \begin{pmatrix} \mathrm{D1} \\ \mathrm{D2} \end{pmatrix} = \begin{pmatrix} \sqrt{\frac{I_{\mathrm{D1}}}{I}} & 0 \\ 0 & \sqrt{\frac{I_{\mathrm{D2}}}{I}} \end{pmatrix} \begin{pmatrix} \mathrm{D1} \\ \mathrm{D2} \end{pmatrix}. \tag{C.2}$$

At conical configuration point (where D10 = −146.6° and D20 = −60.0°), we estimate from (10) and (11) that I_{D2} = 1342893.5 a.u. and I_{D1} = 3453.3 a.u. so that $I = \sqrt{I_{\mathrm{D1}} I_{\mathrm{D2}}}$ = 68098.6 a.u.

Let us start from conical configuration point (D10, D20) as reference point for the seam and they are transferred to variables x_0 and y_0 (see in Figure 8) by (C.2), and then we assume that x_1 and y_1 are a predefined point on the seam with s direction normal to distance direction between (x_0, y_0) and (x_1, y_1); thus the point (x, y) along s coordinate can be expressed as

$$\begin{aligned} x &= s\cos\left(\theta + \frac{\pi}{2}\right) + x_1, \\ y &= s\sin\left(\theta + \frac{\pi}{2}\right) + y_1. \end{aligned} \tag{C.3}$$

Derivative of potential energy surfaces defined in (B.6) with respect to s at (x_1, y_1) can be estimated as

$$\begin{aligned} \left.\frac{\partial W_{\pm}(x, y)}{\partial s}\right|_{s=0} &= \left.\frac{\partial W_{\pm}}{\partial x}\right|_{s=0} \cos\left(\theta + \frac{\pi}{2}\right) \\ &\quad + \left.\frac{\partial W_{\pm}}{\partial y}\right|_{s=0} \sin\left(\theta + \frac{\pi}{2}\right). \end{aligned} \tag{C.4}$$

This equation has to be transformed to the original variables D_1 and D_2 in terms of which the potential energy surfaces are given by

$$\begin{aligned} &\left.\frac{\partial W_{\pm}(\mathrm{D1}, \mathrm{D2})}{\partial s}\right|_{s=0} \\ &= \left.\frac{\partial W_{\pm}}{c_1 \partial \mathrm{D1}}\right|_{s=0} \cos\left(\theta + \frac{\pi}{2}\right) + \left.\frac{\partial W_{\pm}}{c_2 \partial \mathrm{D}_2}\right|_{s=0} \sin\left(\theta + \frac{\pi}{2}\right), \end{aligned} \tag{C.5}$$

where c_1 and c_2 are defined in (C.2), and θ is given as

$$tg\theta = \frac{(y_1 - y_0)}{(x_1 - x_0)} = \frac{c_2\,(\mathrm{D2} - \mathrm{D20})}{c_1\,(\mathrm{D1} - \mathrm{D10})}. \tag{C.6}$$

Finally, we can have an expression for effective coupling parameter

$$\begin{aligned} a^2 &= \left.\frac{\hbar^2}{16I}\frac{1}{(\Delta E_0)^3}\left(\frac{\partial}{\partial s}[W_+ + W_-]\right)^2\right|_{s=0} \\ &= \frac{\hbar^2}{16I}\frac{1}{(\Delta E_0)^3}\frac{1}{tg^2\theta + 1} \\ &\quad \times \left(-\frac{1}{c_1}\left(\frac{\partial W_+}{\partial \mathrm{D1}} + \frac{\partial W_-}{\partial \mathrm{D1}}\right) tg\theta + \frac{1}{c_2}\left(\frac{\partial W_+}{\partial \mathrm{D2}} + \frac{\partial W_-}{\partial \mathrm{D2}}\right)\right)^2 \end{aligned} \tag{C.7}$$

in which

$$\Delta E_0 = \frac{W_+(\mathrm{D1}, \mathrm{D2}) - W_-(\mathrm{D1}, \mathrm{D2})}{2}. \tag{C.8}$$

When θ is rotating with respect to the conic point (x_0, y_0), the local maxima a^2 can be obtained. In this way, we can determine one point on seam surface as well as a^2 at that point. Then we can use this point as reference point to search next point on seam surface. Finally, we can determine whole seam surface and a^2 distribution on seam surface simultaneously.

C.2. The Effective Collision Energy b^2 and the Momentum Changes during Hopping. Classical trajectory is running in the Cartesian coordinate system, while the surface hopping is taking place in the system of internal dihedral angles D1 and D2. We need project internal coordinates to Cartesian coordinates after hopping; besides we cannot use all kinetic energy for hopping and only part of kinetic energy along

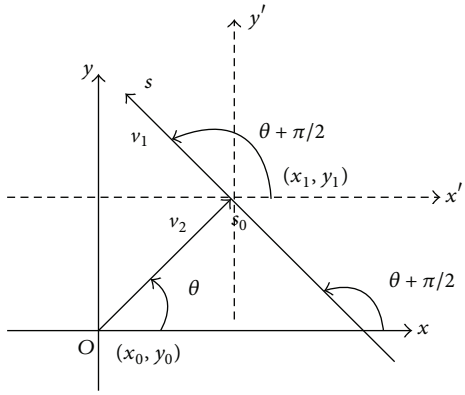

Figure 8: Schematic diagram in which s is assumed as direction of nonadiabatic coupling vector.

hopping direction can be utilized. Let us write down classical kinetic energy in terms dihedral angles D1 and D2 as

$$\begin{aligned} T &= \frac{1}{2}I_{\mathrm{D1}}\left(\dot{\mathrm{D}}1\right)^2 + \frac{1}{2}I_{\mathrm{D2}}\left(\dot{\mathrm{D}}2\right)^2 \\ &= \frac{1}{2}I\left(\dot{x}^2 + \dot{y}^2\right) = \frac{1}{2}I\left(v_1^2 + v_2^2\right), \end{aligned} \tag{C.9}$$

where dot stands for derivative with respect to time t, and relation between $(\dot{\mathrm{D}}1, \dot{\mathrm{D}}2)$ and $(\dot{x}, \dot{y})$ is given in (C.2). The last equality in (C.9) is defined as

$$\begin{pmatrix} v_1 \\ v_2 \end{pmatrix} = \begin{pmatrix} -\sin\theta & \cos\theta \\ \cos\theta & \sin\theta \end{pmatrix}\begin{pmatrix} \dot{x} \\ \dot{y} \end{pmatrix}, \tag{C.10}$$

where v_1 is angular velocity along s direction and v_2 is angular velocity along the direction normal to s as shown in Figure 8. If we assume that (v_1, v_2) change to (v_1', v_2') after hopping, then they should satisfy

$$v_1' = kv_1, \qquad v_2' = v_2, \tag{C.11}$$

where v_2 is unchanged and k can be estimated from energy conservation as

$$k = \sqrt{1 \pm \frac{4\Delta E_0}{\left(Iv_1^2\right)}} \tag{C.12}$$

with $\Delta E_0 = (W_+ - W_-)/2$, in which "+" ("−") represents hopping from upper (lower) potential to lower (upper) potential. We discuss the classical allowed vertical hop in the present system, namely, $k \geq 0$ since the collision energy is quite large. We now need to convert (v_1', v_2') to $(\dot{x}', \dot{y}')$ that represent angular velocity change after hop along x and y direction shown in Figure 8. Equations (C.10) and (C.11) lead to the following relation:

$$\begin{aligned} \dot{y}'\cos\theta - \dot{x}'\sin\theta &= k\left(\dot{y}\cos\theta - \dot{x}\sin\theta\right), \\ \dot{x}'\cos\theta + \dot{y}'\sin\theta &= \dot{x}\cos\theta + \dot{y}\sin\theta, \end{aligned} \tag{C.13}$$

from which we can obtain

$$\begin{pmatrix} \dot{x}' \\ \dot{y}' \end{pmatrix} = \begin{pmatrix} \cos^2\theta + k\sin^2\theta & (1-k)\sin\theta\cos\theta \\ (1-k)\sin\theta\cos\theta & k\cos^2\theta + \sin^2\theta \end{pmatrix}\begin{pmatrix} \dot{x} \\ \dot{y} \end{pmatrix}. \tag{C.14}$$

This can be converted to original dihedral angles D1 and D2 system as

$$\begin{aligned} \begin{pmatrix} \dot{\mathrm{D}}1' \\ \dot{\mathrm{D}}2' \end{pmatrix} &= \begin{pmatrix} T_{11} & T_{12} \\ T_{21} & T_{22} \end{pmatrix}\begin{pmatrix} \dot{\mathrm{D}}1 \\ \dot{\mathrm{D}}2 \end{pmatrix} \\ &= \begin{pmatrix} \cos^2\theta + k\sin^2\theta & c_2^2(1-k)\sin\theta\cos\theta \\ c_1^2(1-k)\sin\theta\cos\theta & k\cos^2\theta + \sin^2\theta \end{pmatrix} \\ &\quad \times \begin{pmatrix} \dot{\mathrm{D}}1 \\ \dot{\mathrm{D}}2 \end{pmatrix}, \end{aligned} \tag{C.15}$$

where $(\dot{\mathrm{D}}1', \dot{\mathrm{D}}2')$ stand for angular velocity after hop in original dihedral angle system, and c_1 and c_2 are defined in (C.2). The effective collision energy for b^2 in (B.7) is then given by collision energy

$$\begin{aligned} E &= \frac{1}{2}I\left(v_1^2\right) + W_{\pm} \\ &= \frac{1}{2}I\left(c_2\dot{\mathrm{D}}2\cos\theta - c_1\dot{\mathrm{D}}1\sin\theta\right)^2 + W_{\pm}. \end{aligned} \tag{C.16}$$

Next, we derive relation between internal angular velocities and their corresponding velocities in Cartesian coordinate system. As we analyzed in the text that dihedral angle is defined by the Cartesian coordinates of four atoms; for example, the dihedral angle D1 is given as

$$\cos\left(\mathrm{D}1\right)\left|\overrightarrow{\mu}\right|\left|\overrightarrow{\nu}\right| - \vec{\mu}\cdot\vec{\nu} = 0, \tag{C.17}$$

where $\vec{\mu} = \vec{a}\times\vec{b}$ and $\vec{\nu} = \vec{b}\times\vec{c}$ (see Scheme 1 for definition of bond vectors $\vec{a}$, $\vec{b}$, and $\vec{c}$). Taking derivative with respect to time t in (C.17) with consideration that all bond angles and bond distances are fixed, we have

$$\dot{\mathrm{D}}1 = -\frac{d\left(\vec{\mu}\cdot\vec{\nu}\right)}{dt}\left[\left|\vec{\mu}\right|\left|\overrightarrow{\nu}\right|\sin\left(\mathrm{D}1\right)\right]^{-1}, \tag{C.18}$$

where

$$\begin{aligned} \frac{d\left(\vec{\mu}\cdot\vec{\nu}\right)}{dt} &= \frac{d}{dt}\left[\left(\vec{a}\cdot\vec{b}\right)\left(\vec{b}\cdot\vec{c}\right) - \left(\vec{a}\cdot\vec{c}\right)\left(\vec{b}\cdot\vec{b}\right)\right] \\ &= -\left|\vec{b}\right|^2\frac{d\left(\vec{a}\cdot\vec{c}\right)}{dt} \\ &= -\left|\vec{b}\right|^2\left[\left(\dot{\vec{r}}_2 - \dot{\vec{r}}_1\right)\cdot\vec{c} + \vec{a}\cdot\left(\dot{\vec{r}}_4 - \dot{\vec{r}}_3\right)\right] \\ &= -\left|\vec{b}\right|^2\left(\dot{\vec{r}}_2 - \dot{\vec{r}}_1 + \dot{\vec{r}}_4 - \dot{\vec{r}}_3\right)\cdot\left(\vec{c} + \vec{a}\right) \end{aligned} \tag{C.19}$$

in which we utilized that all bond angles and bond distances are fixed again. Thus, we obtain

$$\dot{\mathrm{D}}1 = \vec{A}\cdot\left(\dot{\vec{r}}_2 - \dot{\vec{r}}_1 + \dot{\vec{r}}_4 - \dot{\vec{r}}_3\right), \tag{C.20}$$

where

$$\vec{A} = \frac{(\vec{c} + \vec{a})\left|\vec{b}\right|^2}{\left|\vec{a} \times \vec{b}\right|\left|\vec{b} \times \overrightarrow{c}\right| \sin(\mathrm{D1})}. \tag{C.21}$$

In the same way as we derived (C.20), we can have

$$\dot{\mathrm{D}}2 = \vec{B} \cdot \left(\dot{\vec{r}}_2 - \dot{\vec{r}}_5 + \dot{\vec{r}}_6 - \dot{\vec{r}}_3\right), \tag{C.22}$$

where (see Scheme 1 for definition of bond vectors $\vec{e}$ and $\vec{d}$)

$$\vec{B} = \frac{\left(\vec{e} + \vec{d}\right)\left|\vec{b}\right|^2}{\left|\vec{e} \times \vec{b}\right|\left|\vec{d} \times \vec{b}\right| \sin(\mathrm{D2})}. \tag{C.23}$$

Assume that velocities after hop in Cartesian coordinate system are $\dot{\vec{r}}_1'$, $\dot{\vec{r}}_2'$, $\dot{\vec{r}}_3'$, $\dot{\vec{r}}_4'$, $\dot{\vec{r}}_5'$, and $\dot{\vec{r}}_6'$, and then they are related to angular velocities after hop as

$$\begin{aligned} \dot{\mathrm{D}}1' &= \vec{A} \cdot \left(\dot{\vec{r}}_2' - \dot{\vec{r}}_1' + \dot{\vec{r}}_4' - \dot{\vec{r}}_3'\right), \\ \dot{\mathrm{D}}2' &= \vec{B} \cdot \left(\dot{\vec{r}}_2' - \dot{\vec{r}}_5' + \dot{\vec{r}}_6' - \dot{\vec{r}}_3'\right) \end{aligned} \tag{C.24}$$

in which $\vec{A}$ and $\vec{B}$ are the same as in (C.20) and (C.22) since we consider the vertical hop. Inserting (C.24) and (C.20) and (C.22) into (C.15) leads to

$$\begin{aligned} &\vec{A} \cdot \left(\dot{\vec{r}}_4' - \dot{\vec{r}}_1'\right) + \vec{A} \cdot \left(\dot{\vec{r}}_2' - \dot{\vec{r}}_3'\right) \\ &\quad = T_{11}\vec{A} \cdot \left[\left(\dot{\vec{r}}_2 - \dot{\vec{r}}_3\right) + \left(\dot{\vec{r}}_4 - \dot{\vec{r}}_1\right)\right] \\ &\qquad + T_{12}\vec{B} \cdot \left[\left(\dot{\vec{r}}_2 - \dot{\vec{r}}_3\right) + \left(\dot{\vec{r}}_6 - \dot{\vec{r}}_5\right)\right], \\ &\vec{B} \cdot \left(\dot{\vec{r}}_6' - \dot{\vec{r}}_5'\right) + \vec{B} \cdot \left(\dot{\vec{r}}_2' - \dot{\vec{r}}_3'\right) \\ &\quad = T_{21}\vec{A} \cdot \left[\left(\dot{\vec{r}}_2 - \dot{\vec{r}}_3\right) + \left(\dot{\vec{r}}_4 - \dot{\vec{r}}_1\right)\right] \\ &\qquad + T_{22}\vec{B} \cdot \left[\left(\dot{\vec{r}}_2 - \dot{\vec{r}}_3\right) + \left(\dot{\vec{r}}_6 - \dot{\vec{r}}_5\right)\right], \end{aligned} \tag{C.25}$$

where T_{ij} is defined in (C.15). There are only two equations for six unknown Cartesian velocities after hop so that we need to make some physical intuitions to solve this problem. Let us assume that the relative motions after hop can in general be expressed as

$$\begin{aligned} \dot{\vec{r}}_4' - \dot{\vec{r}}_1' &= \alpha_1\left(\dot{\vec{r}}_4 - \dot{\vec{r}}_1\right) \times \left(\vec{r}_4 - \vec{r}_1\right) + k_1\left(\dot{\vec{r}}_4 - \dot{\vec{r}}_1\right), \\ \dot{\vec{r}}_6' - \dot{\vec{r}}_5' &= \alpha_2\left(\dot{\vec{r}}_6 - \dot{\vec{r}}_5\right) \times \left(\vec{r}_6 - \vec{r}_5\right) + k_2\left(\dot{\vec{r}}_6 - \dot{\vec{r}}_5\right), \\ \dot{\vec{r}}_2' - \dot{\vec{r}}_3' &= \alpha_3\left(\dot{\vec{r}}_2 - \dot{\vec{r}}_3\right) \times \left(\vec{r}_2 - \vec{r}_3\right) + k_3\left(\dot{\vec{r}}_2 - \dot{\vec{r}}_3\right). \end{aligned} \tag{C.26}$$

The first assumption is that all α_i is equal to zero. Then, the relative motion $(\dot{\vec{r}}_3' - \dot{\vec{r}}_2')$ does not change after hop ($k_3 = 1$) as the rotation is around bond 2–3 as shown in Scheme 1. Therefore, we can derive

$$\begin{aligned} k_1 &= \Big(\left((T_{11} - 1)\vec{A} + T_{12}\vec{B}\right) \cdot \left(\dot{\vec{r}}_2 - \dot{\vec{r}}_3\right) \\ &\quad + T_{11}\vec{A} \cdot \left(\dot{\vec{r}}_4 - \dot{\vec{r}}_1\right) + T_{12}\vec{B} \cdot \left(\dot{\vec{r}}_6 - \dot{\vec{r}}_5\right)\Big) \\ &\quad \times \left(\vec{A} \cdot \left(\dot{\vec{r}}_4 - \dot{\vec{r}}_1\right)\right)^{-1}, \\ k_2 &= \Big(\left(T_{21}\vec{A} + (T_{22} - 1)\vec{B}\right) \cdot \left(\dot{\vec{r}}_2 - \dot{\vec{r}}_3\right) \\ &\quad + T_{21}\vec{A} \cdot \left(\dot{\vec{r}}_4 - \dot{\vec{r}}_1\right) + T_{22}\vec{B} \cdot \left(\dot{\vec{r}}_6 - \dot{\vec{r}}_5\right)\Big) \\ &\quad \times \left(\vec{B} \cdot \left(\dot{\vec{r}}_6 - \dot{\vec{r}}_5\right)\right)^{-1}. \end{aligned} \tag{C.27}$$

Finally, we can assume after hop that $\dot{\vec{r}}_1' = k_1\dot{\vec{r}}_1$, $\dot{\vec{r}}_2' = \dot{\vec{r}}_2$, $\dot{\vec{r}}_3' = \dot{\vec{r}}_3$, $\dot{\vec{r}}_4' = k_1\dot{\vec{r}}_4$, $\dot{\vec{r}}_5' = k_2\dot{\vec{r}}_5$, and $\dot{\vec{r}}_6' = k_2\dot{\vec{r}}_6$.

The moment of inertia $I = \sqrt{I_{\mathrm{D1}}I_{\mathrm{D2}}}$ is varying slowly with time as evolution of trajectory. For a convenience, we do surface hopping calculation with the constant moment of inertia at conic point. This introduces small error for energy conservation (this is actually small) because velocities in Cartesian coordinate after hopping might not satisfy constraint conditions exactly. We assume that the Cartesian velocities of atoms 2 and 3 are unchanged during hopping, so that we would do scaling for the Cartesian velocities of atoms 1, 4, 5, and 6 as $\dot{\vec{r}}_1' = \lambda k_1\dot{\vec{r}}_1$, $\dot{\vec{r}}_4' = \lambda k_1\dot{\vec{r}}_4$, $\dot{\vec{r}}_5' = \lambda k_2\dot{\vec{r}}_5$, and $\dot{\vec{r}}_6' = \lambda k_2\dot{\vec{r}}_6$ to restore energy conservation in which $\lambda = \sqrt{1 - \Delta\varepsilon/T}$, where $\Delta\varepsilon$ is energy lose and T is kinetic energy for atoms 1, 4, 5, and 6 before scaling. This can be done iteratively with constraint Hamiltonian equation. Actually, we confirm that λ is close to unity from numerical calculation during surface hopping (λ is exact unity if hopping is taking place right at conic point).

Conflict of Interests

The authors declare that there is no conflict of interests regarding the publication of this paper.

Acknowledgments

Yibo Lei would like to acknowledge the Postdoctoral Fellowship supported by National Science Council of China under Grant no. 100-2811-M-009-004. This work is supported by National Science Council of China under Grant no. 100-2113-M-009-005-MY3. Yibo Lei would also like to acknowledge the support from National Science Foundation of China (Grant nos. 21033001, 21103136, and 21173166). Chaoyuan Zhu would like to thank the MOE-ATU Project of the National Chiao Tung University for support.

References

[1] J. C. Tully and R. K. Pkeston, "Trajectory surface hopping approach to nonadiabatic molecular collisions: the reaction of H^+ with D_2," *The Journal of Chemical Physics*, vol. 55, no. 2, pp. 562–572, 1971.

[2] J. C. Tully, "Molecular dynamics with electronic transitions," *The Journal of Chemical Physics*, vol. 93, no. 2, pp. 1061–1071, 1990.

[3] C. Zhu and H. Nakamura, "Theory of nonadiabatic transition for general two-state curve crossing problems. II. Landau-Zener case," *The Journal of Chemical Physics*, vol. 102, no. 19, pp. 7448–7461, 1995.

[4] C. Zhu, H. Kamisaka, and H. Nakamura, "New implementation of the trajectory surface hopping method with use of the Zhu-Nakamura theory. II. application to the charge transfer processes in the 3D DH_2^+ system," *Journal of Chemical Physics*, vol. 116, no. 8, pp. 3234–3247, 2002.

[5] E. Tapavicza, I. Tavernelli, U. Rothlisberger, C. Filippi, and M. E. Casida, "Mixed time-dependent density-functional theory/classical trajectory surface hopping study of oxirane photochemistry," *The Journal of Chemical Physics*, vol. 129, no. 12, Article ID 124108, 2008.

[6] M. Sanier, U. Manthe, and G. Stock, "Quantum-classical Liouville description of multidimensional nonadiabatic molecular dynamics," *The Journal of Chemical Physics*, vol. 114, no. 5, pp. 2001–2012, 2001.

[7] I. Burghardt and G. Parlant, "On the dynamics of coupled Bohmian and phase-space variables: a new hybrid quantum-classical approach," *The Journal of Chemical Physics*, vol. 120, no. 7, pp. 3055–3058, 2004.

[8] P. Pechukas, "Time-dependent semiclassical scattering theory. II. atomic collisions," *Physical Review*, vol. 181, no. 1, pp. 174–185, 1969.

[9] J. S. Cao and G. A. Voth, "The formulation of quantum statistical mechanics based on the Feynman path centroid density. IV. algorithms for centroid molecular dynamics," *The Journal of Chemical Physics*, vol. 101, no. 7, pp. 6168–6183, 1994.

[10] M. Ben-Nun, J. Quenneville, and T. J. Martínez, "*Ab initio* multiple spawning: photochemistry from first principles quantum molecular dynamics," *The Journal of Physical Chemistry A*, vol. 104, no. 22, pp. 5172–5175, 2000.

[11] A. N. Alexandrova, J. C. Tully, and G. Granucci, "Photochemistry of DNA fragments via semiclassical nonadiabatic dynamics," *The Journal of Physical Chemistry B*, vol. 114, no. 37, pp. 12116–12128, 2010.

[12] B. F. E. Curchod, T. J. Penfold, U. Rothlisberger, and I. Tavernelli, "Local control theory in trajectory-based nonadiabatic dynamics," *Physical Review A*, vol. 84, no. 4, Article ID 042507, 2011.

[13] R. Crespo-Otero and M. Barbatti, "$Cr(CO)_6$ photochemistry: semi-classical study of UV absorption spectral intensities and dynamics of photodissociation," *The Journal of Chemical Physics*, vol. 134, no. 16, Article ID 164305, 2011.

[14] E. Fabiano, T. W. Keal, and W. Thiel, "Implementation of surface hopping molecular dynamics using semiempirical methods," *Chemical Physics*, vol. 349, no. 1–3, pp. 334–347, 2008.

[15] Z. Lan, E. Fabiano, and W. Thiel, "Photoinduced nonadiabatic dynamics of pyrimidine nucleobases: on-the-fly surface-hopping study with semiempirical methods," *The Journal of Physical Chemistry B*, vol. 113, no. 11, pp. 3548–3555, 2009.

[16] O. Weingart, Z. Lan, A. Koslowski, and W. Thiel, "Chiral pathways and periodic decay in *cis*-azobenzene photodynamics," *The Journal of Physical Chemistry Letters*, vol. 2, no. 13, pp. 1506–1509, 2011.

[17] T. W. Keal, M. Wanko, and W. Thiel, "Assessment of semiempirical methods for the photoisomerisation of a protonated Schiff base," *Theoretical Chemistry Accounts*, vol. 123, no. 1-2, pp. 145–156, 2009.

[18] V. Leyva, I. Corral, F. Feixas et al., "A non-adiabatic quantum-classical dynamics study of the intramolecular excited state hydrogen transfer in *ortho-nitrobenzaldehyde*," *Physical Chemistry Chemical Physics*, vol. 13, no. 32, pp. 14685–14693, 2011.

[19] I. Tavernelli, B. F. E. Curchod, and U. Rothlisberger, "Mixed quantum-classical dynamics with time-dependent external fields: a time-dependent density-functional-theory approach," *Physical Review A*, vol. 81, no. 5, Article ID 052508, 2010.

[20] M. Barbatti, R. Shepard, and H. Lischka, "Computational and methodological elements for nonadiabatic trajectory dynamics simulations of molecules," in *Conical Intersections: Theory, Computation and Experiment*, W. Domcke, D. R. Yarkony, and H. Köppel, Eds., World Scientific, Singapore, 2010.

[21] T. Ishida, S. Nanbu, and H. Nakamura, "Nonadiabatic *ab initio* dynamics of two models of Schiff base retinal," *The Journal of Physical Chemistry A*, vol. 113, no. 16, pp. 4356–4366, 2009.

[22] A. Gao, B. Li, P. Zhang, and K. Han, "Nonadiabatic *ab initio* molecular dynamics of photoisomerization in bridged azobenzene," *The Journal of Chemical Physics*, vol. 137, no. 20, Article ID 204305, 2012.

[23] A. Gao, B. Li, P. Zhang, and J. Liu, "Photochemical dynamics simulations for *trans-cis* photoisomerizations of azobenzene and bridged azobenzen," *Computational and Theoretical Chemistry*, vol. 1031, pp. 13–21, 2014.

[24] J.-P. Ryckaert, G. Ciccotti, and H. J. C. Berendsen, "Numerical integration of the cartesian equations of motion of a system with constraints: molecular dynamics of n-alkanes," *Journal of Computational Physics*, vol. 23, no. 3, pp. 327–341, 1977.

[25] V. Kräutler, W. F. van Gunsteren, and P. H. Hünenberger, "A fast SHAKE algorithm to solve distance constraint equations for small molecules in molecular dynamics simulations," *Journal of Computational Chemistry*, vol. 22, no. 5, pp. 501–508, 2001.

[26] G. Ciccotti and J.-P. Ryckaert, "Molecular dynamics simulation of rigid molecules," *Computer Physics Reports*, vol. 4, no. 6, pp. 346–392, 1986.

[27] P. Gonnet, "P-SHAKE: a quadratically convergent SHAKE in $O(n^2)$," *Journal of Computational Physics*, vol. 220, no. 2, pp. 740–750, 2007.

[28] S. Miyamoto and P. A. Kollman, "Settle: an analytical version of the SHAKE and RATTLE algorithm for rigid water models," *Journal of Computational Chemistry*, vol. 13, no. 8, pp. 952–962, 1992.

[29] E. Barth, K. Kuczera, B. Leimkuhler, and R. D. Skeel, "Algorithms for constrained molecular dynamics," *Journal of Computational Chemistry*, vol. 16, no. 10, pp. 1192–1209, 1995.

[30] P. E. Gill, W. Murray, and M. H. Wright, *Numerical Linear Algebra and Optimization*, Addison-Wesley, Redwood City, Calif, USA, 1991.

[31] T. Chu, Y. Zhang, and K. Han, "The time-dependent quantum wave packet approach to the electronically nonadiabatic processes in chemical reactions," *International Reviews in Physical Chemistry*, vol. 25, no. 1-2, pp. 201–235, 2006.

[32] K. Han, J. Huang, S. Chai, S. Wen, and W. Deng, "Anisotropic mobilities in organic semiconductors," *Nature Protocol Exchange*, 2013.

[33] Y. Lei, C. Zhu, Z. Wen, and S. Lin, "New implementation of semi-classical dynamic simulation on the photoisomerization of *cis*- and *trans*- isomers of free stilbene," *Acta Chimica Sinica*, vol. 70, no. 17, pp. 1869–1876, 2012.

[34] A. J. Neukirch, L. C. Shamberger, E. Abad et al., "Nonadiabatic ensemble simulations of *cis*-stilbene and *cis*-azobenzene photoisomerization," *Journal of Chemical Theory and Computation*, vol. 10, no. 1, pp. 14–23, 2014.

[35] Y. Ootani, K. Satoh, A. Nakayama, T. Noro, and T. Taketsugu, "*Ab initio* molecular dynamics simulation of photoisomerization in azobenzene in the n π state," *The Journal of Chemical Physics*, vol. 131, no. 19, Article ID 194306, 2009.

[36] A. Toniolo, C. Ciminelli, M. Persico, and T. J. Martínez, "Simulation of the photodynamics of azobenzene on its first excited state: comparison of full multiple spawning and surface hopping treatments," *The Journal of Chemical Physics*, vol. 123, no. 23, Article ID 234308, 2005.

[37] P. Cattaneo and M. Persico, "*An abinitio* study of the photochemistry of azobenzene," *Physical Chemistry Chemical Physics*, vol. 1, pp. 4739–4743, 1999.

[38] M. Pederzoli, J. Pittner, M. Barbatti, and H. Lischka, "Nonadiabatic molecular dynamics study of the *cis-trans* photoisomerization of azobenzene excited to the S_1 state," *The Journal of Physical Chemistry A*, vol. 115, no. 41, pp. 11136–11143, 2011.

[39] D. Gegiou, K. A. Muszkat, and E. Fischer, "Temperrature dependence of photoisomerization. VI. viscosity effect," *The Journal of the American Chemical Society*, vol. 90, no. 1, pp. 12–18, 1968.

[40] D. Gegiou, K. A. Muszkat, and E. Fischer, "Temperature dependence of photoisomerization. V. effect of subsituents on the photoisomerization of stilbenes and azobenzenes," *Journal of the American Chemical Society*, vol. 90, no. 15, pp. 3907–3917, 1968.

[41] A. Gilbert and J. Baggott, *Essentials of Molecular Photochemistry*, Blackwell Science, Oxford, UK, 1991.

[42] R. S. H. Liu, "Photoisomerization by Hula-Twist: a fundamentalsupramolecular photochemical reaction," *Accounts of Chemical Research*, vol. 34, no. 7, pp. 555–562, 2001.

[43] R. D. Sampedro, A. Cembran, M. Garavelli, M. Olivucci, and W. Fuβ, "Structure of the conical intersections driving the *cis-trans* photoisomerization of conjugated molecules," *Photochemistry and Photobiology*, vol. 76, no. 6, pp. 622–633, 2002.

[44] Y. Amatatsu, "*Ab initio* study on the electronic structures of stilbene at the conical intersection," *Chemical Physics Letters*, vol. 314, no. 3-4, pp. 364–368, 1999.

[45] J. Quenneville and T. J. Martínez, "*Ab initio* study of *cis-trans* photoisomerization in stilbene and ethylene," *The Journal of Physical Chemistry A*, vol. 107, no. 6, pp. 829–837, 2003.

[46] M. J. Bearpark, F. Bernardi, S. Clifford, M. Olivucci, M. A. Robb, and T. Vreven, "Cooperating rings in *cis*-stilbene lead to an S_0/S_1 conical intersection," *The Journal of Physical Chemistry A*, vol. 101, no. 21, pp. 3841–3847, 1997.

[47] J. H. Frederick, Y. Fujiwara, J. H. Penn, K. Yoshihara, and H. Petek, "Models for stilbene photoisomerization: experimental and theoretical studies of the excited-state dynamics of 1,2-diphenylcycloalkenes," *The Journal of Physical Chemistry*, vol. 95, no. 7, pp. 2845–2858, 1991.

[48] V. D. Vachev, J. H. Frederick, B. A. Grishanin, V. N. Zadkov, and N. I. Koroteev, "Stilbene isomerization dynamics on multidimensional potential energy surface. Molecular dynamics simulation," *Chemical Physics Letters*, vol. 215, no. 4, pp. 306–314, 1993.

[49] V. D. Vachev, J. H. Frederick, B. A. Grishanin, V. N. Zadkov, and N. I. Koroteev, "Quasiclassical molecular dynamics simulation of the photoisomerization of stilbene," *The Journal of Physical Chemistry*, vol. 99, no. 15, pp. 5247–5263.

[50] G. Orlandi, L. Gagliardi, S. Melandri, and W. Caminati, "Torsional potential energy surface and vibrational levels in *trans* stilbene," *Journal of Molecular Structure*, vol. 612, no. 2-3, pp. 383–391, 2002.

[51] W.-V. Chiang and J. Laane, "Fluorescence spectra and torsional potential functions for *trans*-stilbene in its S_0 and $S_1(\pi,\pi^*)$ electronic states," *The Journal of Chemical Physics*, vol. 100, no. 12, pp. 8755–8767, 1994.

[52] C. W. Jiang, R. H. Xie, F. L. Li, and R. E. Allen, "*Trans*-to-*cis* isomerization of stilbene following an ultrafast laser pulse," *Chemical Physics Letters*, vol. 474, no. 4–6, pp. 263–267, 2009.

[53] Y. Dou and R. E. Allen, "Detailed dynamics of a complex photochemical reaction: *cis-trans* photoisomerization of stilbene," *The Journal of Chemical Physics*, vol. 119, no. 20, pp. 10658–10666, 2003.

[54] S. Takeuchi, S. Ruhman, T. Tsuneda, M. Chiba, T. Taketsugu, and T. Tahara, "Spectroscopic tracking of structural evolution in ultrafast stilbene photoisomerization," *Science*, vol. 322, no. 5904, pp. 1073–1077, 2008.

[55] W. Fuß, C. Kosmidis, W. E. Schmid, and S. A. Trushin, "The lifetime of the perpendicular minimum of *cis*-stibene observed by dissociative intense-laser field ionization," *Chemical Physics Letters*, vol. 385, pp. 423–430, 2004.

[56] W. Fuß, C. Kosmidis, W. E. Schmid, and S. A. Trushin, "The photochemical *cis-trans* isomerization of free stilbene molecules follows a hula-twist pathway," *Angewandte Chemie International Edition*, vol. 43, no. 32, pp. 4178–4182, 2004.

[57] D. C. Todd and G. R. Fleming, "*Cis*-stilbene isomerization: temperature dependence and the role of mechanical friction," *The Journal of Chemical Physics*, vol. 98, no. 1, pp. 269–279, 1993.

[58] S. Abrash, S. Repinec, and R. M. Hochstrasser, "The viscosity dependence and reaction coordinate for isomerization of *cis*-stilbene," *The Journal of Chemical Physics*, vol. 93, no. 2, pp. 1041–1053, 1990.

[59] R. J. Sension, S. T. Repinec, A. Z. Szarka, and R. M. Hochstrasser, "Femtosecond laser studies of the *cis*-stilbene photoisomerization reactions," *The Journal of Chemical Physics*, vol. 98, no. 8, pp. 6291–6315, 1993.

[60] R. J. Sension, S. T. Repinec, and R. M. Hochstrasser, "Femtosecond laser study of energy disposal in the solution phase isomerization of stilbene," *The Journal of Chemical Physics*, vol. 93, no. 12, pp. 9185–9188, 1990.

[61] S. T. Repinec, R. J. Sension, A. Z. Szarka, and R. M. Hochstrasser, "Femtosecond laser studies of the *cis*-stilbene photoisomerization reactions: the *cis*-stilbene to dihydrophenanthrene reaction," *The Journal of Physical Chemistry*, vol. 95, no. 25, pp. 10380–10385, 1991.

[62] R. Improta and F. Santoro, "Excited-state behavior of *trans* and *cis* isomers of stilbene and stiff stilbene: a TD-DFT study," *The Journal of Physical Chemistry A*, vol. 109, no. 44, pp. 10058–10067, 2005.

[63] C. D. Berweger, W. F. van Gunsteren, and F. Müller-Plathe, "Molecular dynamics simulation with an *ab initio* potential energy function and finite element interpolation: the photoisomerization of *cis*-stilbene in solution," *The Journal of Chemical Physics*, vol. 108, no. 21, pp. 8773–8781, 1998.

[64] J. Tatchen and E. Pollak, "*Ab initio* spectroscopy and photoinduced cooling of the *trans*-stilbene molecule," *The Journal of Chemical Physics*, vol. 128, no. 16, Article ID 164303, 2008.

[65] A. Weigel and N. P. Ernsting, "Excited Stilbene: intramolecular vibrational redistribution and solvation studied by femtosecond

stimulated raman spectroscopy," *The Journal of Physical Chemistry B*, vol. 114, no. 23, pp. 7879–7893, 2010.

[66] G. Karlström, R. Lindh, P.-Å. Malmqvist et al., "MOLCAS: a program package for computational chemistry," *Computational Materials Science*, vol. 28, no. 2, pp. 222–239, 2003.

[67] Matlab, *User Guide*, The Mathworks, Torrance, Calif, USA, http://www.mathworks.com.

[68] J. K. Rice and A. P. Baronavski, "Ultrafast studies of solvent effects in the isomerization of *cis*-stilbene," *The Journal of Physical Chemistry*, vol. 96, no. 8, pp. 3359–3366, 1992.

[69] C. Zhu, K. Nobusada, and H. Nakamura, "New implementation of the trajectory surface hopping method with use of the Zhu-Nakamura theory," *The Journal of Chemical Physics*, vol. 115, no. 7, pp. 3031–3044, 2001.

[70] J. J. Moré, B. S. Garbow, and K. E. Hillstrom, "User guide for MINPACK-1," Argonne National Laboratory Report ANL-80-74, Argonne, Ill, USA, 1980.

[71] M. J. D. Powell, *Numerical Methods for Non-Linear Algebraic Equations*, Gordon and Breach, New York, NY, USA, 1970, Edited by P. Rabinowitz.

[72] L. F. Shampine and H. A. Watts, *Mathematical Software III*, Academic Press, New York, NY, USA, 1977, Edited by J. R. Rice.

[73] C. Zhu, "Unified semiclassical theory for the two-state system: analytical solutions for scattering matrices," *The Journal of Chemical Physics*, vol. 105, no. 10, pp. 4159–4172, 1996.

Hindawi Publishing Corporation
International Journal of Photoenergy
Volume 2014, Article ID 541791, 9 pages
http://dx.doi.org/10.1155/2014/541791

Research Article

Detailed Molecular Dynamics of the Photochromic Reaction of Spiropyran: A Semiclassical Dynamics Study

Gaohong Zhai,[1] Shuai Shao,[1] Shaomei Wu,[1] Yibo Lei,[1] and Yusheng Dou[2]

[1] *Key Laboratory of Synthetic and Natural Functional Molecule Chemistry of Ministry of Education, College of Chemistry & Materials Science and Shaanxi Key Laboratory of Physico-Inorganic Chemistry, Northwest University, Xi'an 710069, China*
[2] *Department of Physical Sciences, Nicholls State University, P.O. Box 2022, Thibodaux, LA 70310, USA*

Correspondence should be addressed to Gaohong Zhai; zgh@nwu.edu.cn and Yibo Lei; leiyb@nwu.edu.cn

Received 10 April 2014; Accepted 20 May 2014; Published 17 June 2014

Academic Editor: Fuli Li

A realistic semiclassical dynamics simulation study is reported for the photoinduced ring-opening reaction of spiropyran. The main simulation results show that one pathway involves hydrogen out-of-plane (HOOP) torsion of phenyl ring nearby N atom in 254 fs on the excited state and the isomerization from cis- to trans-SP that is complete in about 10 ps on the ground state after the electron transition $\pi\sigma^*$; the other dominate pathway corresponds to the ring-opening reaction of trans-SP to form the most stable merocyanine (MC) product. Unlike the previous theoretical finding, one C–C bond cleavage on the real molecule rather than the C–N dissociation of the model one is more probable than the ring-opening reaction after the photoexcitation of SP. The simulation findings provide more important complementarity for interpreting experimental observations, confirming the previously theoretical studies of photochromic ring-opening process and even supplying other possible reaction mechanisms.

1. Introduction

Spiropyran (SP) is one of the very recent most studied photochromic molecules, which are popular materials in sunglasses, optical switching, optical data storage, nonlinear optical devices, optical nanoparticles, photonic crystal, and so on [1–21]. As is well known, the lowest electronic transition of SP occurs in the near UV region ($\lambda < 400$ nm). As shown in Scheme 1, after photoexcitation the bond of Spiro-C and O atom is gradually broken and this compound converts to photoproducts called merocyanine MC. On the contrary, MC can also switch back to the closed form SP by irradiation in the visible region or heating.

The photochromic reactions of SP have been widely studied by time resolved spectroscopy to find the complex mechanism [22–28]. These experimental observations presume that the reaction would involve four steps. The first step corresponds to the initial excitation from the ground state to the excited state ($^1\pi\pi^*$), which very soon (about 50 fs) evolves along the state ($^1\pi\sigma^*$), this is the second step. Subsequently, the drastic changes in structures taking place on a time scale from subpico- to picosecond are the pyranic cycle opening and the C_{spiro}–O bond cleavage. On the final step, a cis-cisoid open-form intermediate is firstly produced, and then several other planar MC photoproducts are formed by the geometrical transformation on pico- to nanosecond scale. Since the substituents on the SP and experimental conditions would be different, the formed products MCs and reaction mechanism are accordingly various. For instance, eight possible conformations for the MC would appear on the reaction process and can be distinguished from each other relative to three central bonds between C atoms (cis, C, and trans, T) as shown in Scheme 1. The most stable MC in solution is trans-trans-cis (TTC) isomer. In addition, very recent experiments show that the ring-opening reaction of unsubstituted SP (1′,3′,3′-trimethylspiro [2*H*-1-benzopyran-2,2′-indoline], also known as BIPS) [29] and double NO_2-substituted derivative (6,8-dinitro-BIPS) [8] involve only singlet states, while a triple state makes a contribution to the dynamic of NO_2-substituted SP (6-nitro-BIPS) [23].

The mechanisms of photochromic reactions of SP have also been studied by various high level quantum calculations

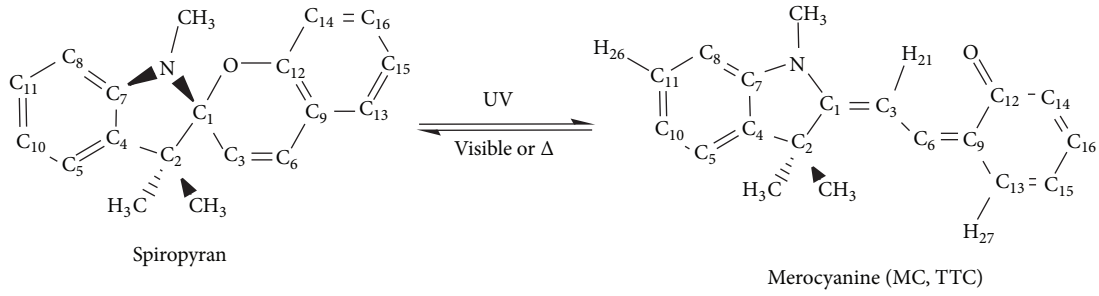

Scheme 1: The scheme of reversible reaction between SP and MC.

Table 1: Key geometry parameters for the ground states of cis- and trans-SP forms as well as the corresponding mode compounds (bond distance in angstroms and dihedral angles in deg).

Species	C_1–O	C_1–N	C_1–C_2	C_1–C_3	α	β	γ	τ
mSPc[a]	1.428	1.465	1.540	1.515	−97.8	−1.0	−11.6	177.1
mSPc[b]	1.445	1.452	1.544	1.502	−98.9	−3.6	−9.3	175.5
mSPc[c]	1.422	1.449	1.542	1.506	−101.6	−1.6	−9.5	176.4
cis-SP[a]	1.385	1.456	1.605	1.530	−101.7	−2.8	−8.9	174.2
mSPt[a]	1.413	1.442	1.570	1.536	−141.8	2.9	8.0	−175.3
mSPt[b]	1.448	1.447	1.551	1.502	−142.6	3.2	9.3	−177.2
mSPt[c]	1.424	1.443	1.548	1.507	−142.6	1.9	10.2	−177.8
trans-SP[a]	1.404	1.435	1.613	1.511	−148.7	5.5	8.6	−180.1

[a]The present work; [b]the previous work refers to [30] with CAM-B3LYP/6-31G(d) optimization; [c]the previous work refers to [30] with CASSCF/6-31G(d) optimization.

using the model molecule [30–41]. There are three different pathways for the photochromic reaction proposed by computations. The first and second kinds of paths are both associated with the C_{spiro}–O stretching and hydrogen-out-of-plane (HOOP) torsion modes (the C atom is connected by Spiro-C) of the excited SP [38–40]. The last pathway involves the lengthening C_{spiro}–N bond and the internal conversion from the electronically excited states to the SP ground state through $CI_{S1/S0}$ (CN) [38–40].

In order to more directly interpret these mechanisms, the semiclassical dynamics of the photochemical reaction have been carried out by the real SP following the excitation using several laser pulses, which is necessary for the photoinduced chemical reaction [42, 43]. The molecular dynamic method used in this work is called semiclassical electron-radiation-ion dynamics (SERID), on which the time-dependent quantum states are calculated for the valence electrons, while the radiation field and the motion of the nuclei are treated classically. The details of this method have been described elsewhere [44, 45]. All degrees of freedom of real SP in the dynamic simulations are included in the calculations and the laser pulse is explicitly coupled to electrons. By monitoring the nuclear motions triggered by a specific laser pulse, it is possible to describe a realistic photochromic reaction path and provide complementary information for the clarification of the complex mechanisms of photochromic process of SP.

2. Results and Discussion

2.1. Optimized Ground-State Geometries. Two ground state geometries of SP, cis- and trans-SP conformers, respectively, are optimized within 5000 fs dynamic simulation. In order to verify the geometry parameters, the mode compounds mSPc for cis- and mSPt for trans-isomers (in which three methyl groups are replaced by hydrogen) are also optimized. Hereafter, the primary dihedral angles N–C_1–C_3–C_6, C_1–C_3–C_6–C_9, C_3–C_6–C_9–C_{12}, and H_{21}–C_3–C_1–C_6 (see Scheme 1) are, respectively, labeled as α, β, γ, and τ that are consistent with the previous work [39, 40]. The key geometry parameters for the ground state of cis- and trans-SP forms as well as the corresponding mode compounds are displayed in Table 1. It is clear that the molecular geometries for both mSPc and mSPt obtained from the present simulations are in well agreement with those from the previous DFT and CASSCF calculations. It is evident that the optimization from the present dynamic simulation could provide reasonable geometry parameters for the real cis- and trans-SP conformers. It should be mentioned that the remarkable lengthening of the C_1–C_2 bonds can be seen on the real cis- and trans-SP in comparison with the previous model SP, where the C_2 atom is connected by two methyl groups not two H atoms on model compounds mSPc and mSPt. On the contrary, the C_1–O bond (also labeled as C_{spiro}–O above) is evidently shortened. The reason for the variations of these two bonds may arise from the donator character of methyl group, so that the electrons can be delocalized from C_2 to an acceptor O atom.

2.2. Internal Conversion Process to the Ground State from Excited SP. In consistence with the experimental conditions of 316 nm on the gas phase [24] and nearby 350 nm in water [28], a laser pulse of 80 fs (FWHM) with an effective photon

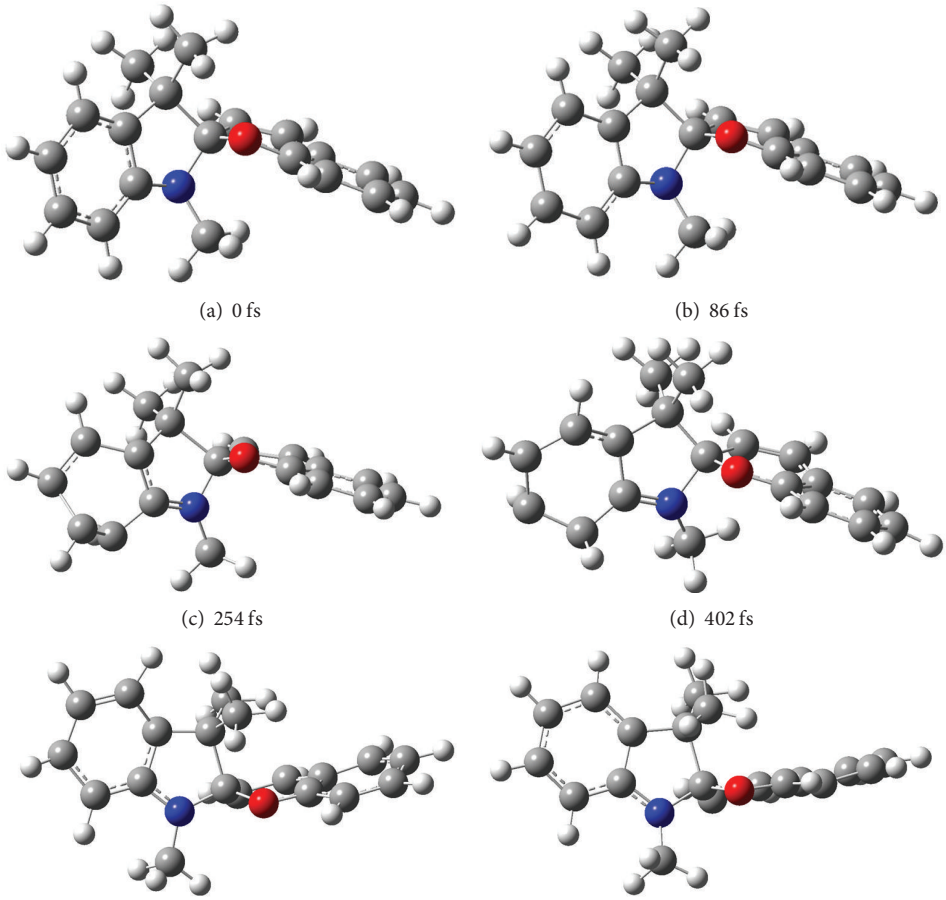

Figure 1: Snapshots taken at different times in a simulation of cis-SP in response to excitation by a 80 fs (FWHM) laser pulse with a fluence of 0.188 kJ/m^2 and photon energy of 4.054 eV, Atom C, H, N, and O are, respectively, denoted by dark grey, French grey, blue, and red; (a)–(f) are at 0 fs, 86 fs, 254 fs, 402 fs, 1658 fs, and 15000 fs, respectively.

Table 2: Key geometry parameters for the dynamic simulation of internal conversion process of cis-SP (time in fs, bond distance in angstroms, and dihedral angles in deg).

Time	C_1–O	C_1–N	C_1–C_2	C_1–C_3	α	β	γ	τ	θ
0	1.385	1.456	1.605	1.530	−101.7	−2.8	−8.9	−185.8	−179.7
86	1.441	1.458	1.570	1.524	−99.8	−3.7	−9.1	−188.9	−183.0
254	1.342	1.432	1.741	1.498	−101.3	−5.0	−5.6	−186.8	−235.4
402	1.466	1.513	1.538	1.486	−98.1	0.6	−12.5	−179.3	−245.7
1658	1.411	1.455	1.664	1.539	−169.1	18.4	4.1	−156.8	−158.7
15000	1.326	1.475	1.676	1.523	−164.1	25.7	−10.0	−134.1	−199.7

energy of 4.054 eV (corresponding to 305.8 nm light) was applied to generate an excitation of cis-SP, in which the primary vibrations, particularly the C_1–C_2 stretching, are impressively activated. The photon energy selected corresponds to the energy difference between the HOMO−1 and LUMO+1 for the beginning ground-state geometry of the molecule in the present approximation. The simulations were run for various fluences and only one typical trajectory will be examined for a fluence of 0.188 kJ/m^2 that creates the desired vibration modes so that the radiationless deactivation of excited SP occurs.

Six snapshots from the simulation at different times and the critical geometry parameters of them are shown in Figure 1 and Table 2, respectively. Starting from the equilibrium geometry in the electronic ground state at 0 fs, the cis-SP conformer is electronically excited by the laser pulse. The most impressive features of the nuclear motions of the excited molecule are the evident C_1–C_2 bond stretching, twist of α,

and HOOP torsion of the phenyl ring connected with N atom presented by the dihedral angle H_{26}–C_{11}–C_8–C_{10} (labeled as θ).

The variations of dihedral angles α, β, γ, τ with time are, respectively, plotted in Figure 2(a), the detailed changes about α, τ, θ in the very beginning of this simulation are also displayed in Figure 2(b) for illustration. It can be viewed that dihedral angle α twists largely from −101.7° at 0 fs to about −160.0° at about 10 ps, while both β and γ oscillate slightly about their initial value of 0°. This means that the initial cis-SP can be transformed into trans-SP in 10 ps, since it can been seen in Table 1 that the dihedral angle α of stable cis- and trans-SP is −97.8° and −148.7°, while β and γ are approximate to 0.0°. After that these angles mainly keep the values until the end of this simulation. It should be emphasized that the molecular vibration is started from the HOOP torsion of phenyl ring, corresponding to the change of dihedral angle θ. It is obvious in Figure 2(b) that this angle oscillates and decreases from −179.7° at 0 fs to −254.5° at 282 fs; after that the average value of −180.0° for θ is kept to the end and the variations of α and τ are initiate as shown in Figure 2(b) and Table 2. Similar to dihedral angle α, the large torsion of τ is weakened at about 10 ps and then the motion maintains an average value about −160.0°. The bond stretches with time are not notable expert for the variation of C_1–C_2 bond. As shown in Figure 2(c), this bond is lengthened after about 210 fs and then its value increases to 1.771 Å at 248 fs. Subsequently, this bond oscillates largely and has a large value of more than 1.800 Å around 4000 fs. After 10 ps, its length approximately decreases to the average value 1.630 Å and keeps this value to the end.

The populations and energies of four interesting frontier molecular orbitals with time, including the HOMO−1, HOMO, LUMO, and LUMO+1, are shown in Figures 3(a) and 3(b), respectively. There are also a small fraction of electrons in the higher-lying unoccupied orbitals and a small fraction of holes in the lower-lying occupied orbitals. However, they do not play a notable role in the dynamical process discussed below. The variations of the electronic populations in different molecular orbitals induce the changes in the forces on the nuclei, driving them into motion. Many vibration modes of the molecule, including the dihedral motions, bond bending vibrations, and bond stretch vibrations, are excited. These excitations in turn change the gaps between the different molecular orbitals.

By the analysis of molecular orbital coefficients, the electronic transitions HOMO−1→LUMO, HOMO−1→LUMO+1, HOMO→LUMO, and HOMO→LUMO+1 of the stable cis-SP can, respectively, be denoted as $\pi_{H-1}\pi_L^*$, $\pi_{H-1}\pi_{L+1}^*$, $n_H\pi_L^*$, and $n_H\pi_{L+1}^*$ at 0 fs. With the photon excitation, the electronic transitions vary with time. Before 86 fs, it can be seen in Figure 3(a) that main electronic transition is from HOMO−1 to LUMO+1, corresponding to $\pi_{H-1}\pi_{L+1}^*$. At 86 fs, it is distinct in Figure 4(b) that the HOMO and HOMO−1 are degenerate and then the significant electronic transfer changes from HOMO−1→LUMO ($\pi_{H-1}\pi_L^*$) to HOMO →LUMO ($\pi_H\pi_L^*$). The dominate transition of $\pi_H\sigma_L^*$ is at 254 fs, corresponding to the degeneracy of HOMO and LUMO. The main nuclear

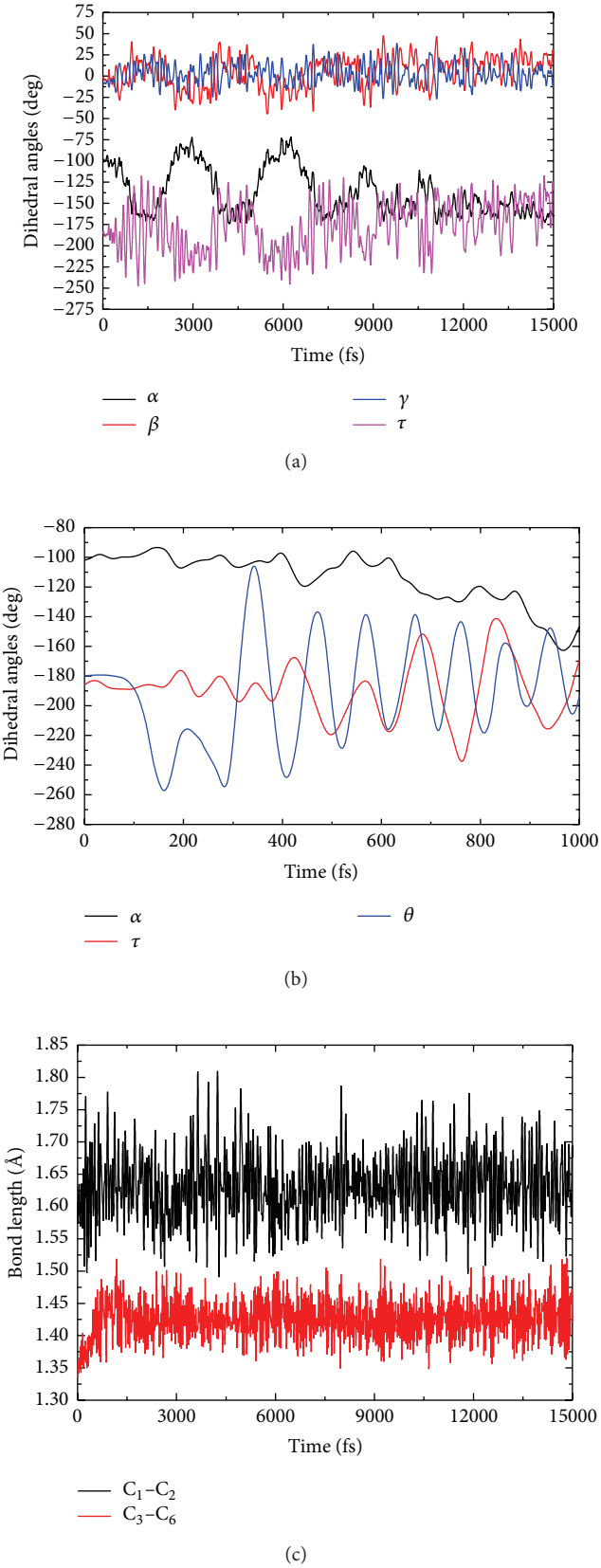

Figure 2: Changes in (a) the dihedral angles α, β, γ, and τ; (b) α, τ, and θ; (c) C_1–C_2 and C_3–C_6 bond lengthens of cis-SP subjected excitation by a 80 fs (FWHM) laser pulse with a fluence of 0.188 kJ/m^2 and photon energy of 4.054 eV.

Table 3: Key geometry parameters for the dynamic simulation of photochromic ring-opening reaction of trans-SP (time in fs, bond distance in angstroms, and dihedral angles in deg) [41].

Time	C_1–O	C_1–N	C_1–C_2	C_1–C_3	α	β	γ	τ	θ
0	1.404	1.435	1.613	1.511	−148.7	5.5	8.6	179.9	181.8
244	1.465	1.432	1.620	1.519	−154.4	1.0	20.1	163.0	244.1
422	1.571	1.430	1.618	1.556	−181.1	45.8	−1.0	134.0	142.7
616	3.618	1.350	1.607	1.504	−87.4	−10.8	58.6	203.7	150.8
4848	3.945	1.380	1.530	1.444	−201.6	−179.6	−37.7	190.2	190.8
15000	4.400	1.371	1.527	1.450	−160.3	−182.8	39.7	175.1	189.7

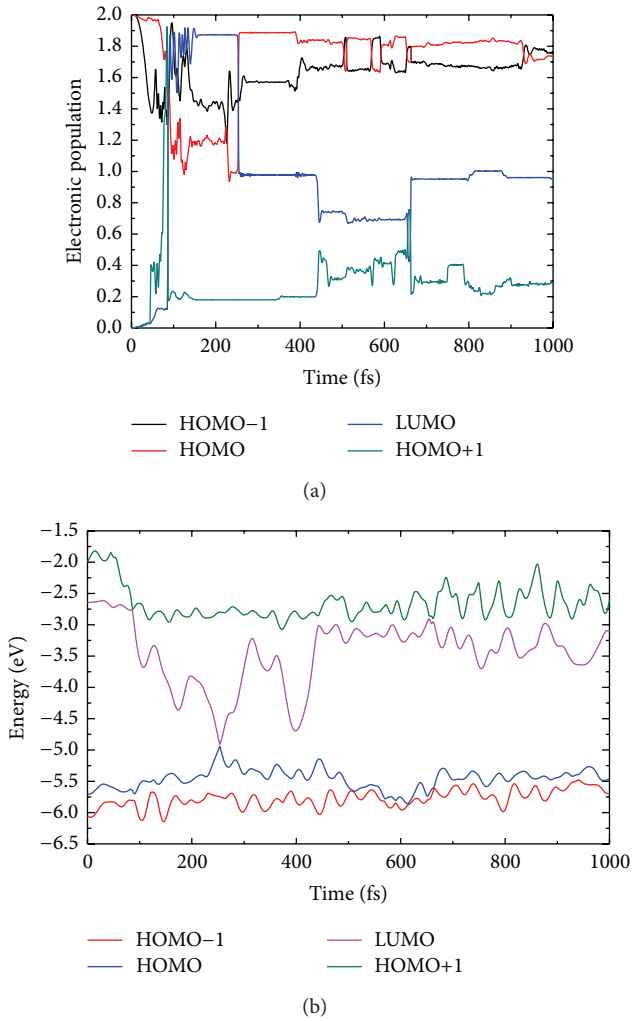

Figure 3: Variations with time of (a) the electronic populations and (b) energies of the HOMO−1, HOMO, LUMO, and LUMO+1 orbitals of cis-SP following application of a 80 fs (FWHM) laser pulse with a fluence of 0.188 kJ/m^2 and photon energy of 4.054 eV.

motion before 254 fs can be found to be the HOOP torsion of phenyl group nearby N atom as described in Figure 2(b). This torsion is similar to those on one pathway of radiationless deactivation reaction of 9H-adenine as reported by Lei et al. [46], where there is an out-of-plane twist of the C_2–H bond of pyrimidine ring before the significant transition between HOMO and LUMO. After that the excited electrons radiationless decay back to the ground state and no remarkable electron transfer between occupied and unoccupied orbitals exists until the end of this simulation. Accordingly, the obtained kinetic energies result in the large variations of dihedral angles α, and bond C_1–C_2 as mentioned above.

With these simulation results, it is easy to study the mechanism of internal conversion process from excited SP to the ground state. In fact, this process corresponds to the photoisomerization from cis-SP to trans-SP. This is an ultrafast process with excited state lifetime only 254 fs. The main nuclear motions on the excited states are the HOOP torsion leading to the deformation of phenyl group nearby N atom, while the isomerization takes place after the electron transition from S_1 to S_0 and go along the latter potential energy surface.

2.3. Photochromic Ring-Opening Reaction of SP. As reported in preceding paper [47] and redescribed in Figure 4 and Table 3, the representative trajectory for the phototriggered ring-opening process shows that ring-opening reaction of excited SP starts from the cooperative HOOP torsions on the excited states and the lifetime of excited states is 422 fs. Then on the ground state the C_1–O bond is broken and the MC-TCC is formed before 616 fs; after that a transient MC-CCC isomer appears and is suddenly replaced by the former MC conformation until 4848 fs. After that the final stable TTC form of MC is created and kept up to the end. This means that the ring-opening process takes about 616 fs, which basically agrees with 900 fs measured by the experiments on the gas phase [24]. The subsequent isomerization on the ground state takes about 4 ps, which is less than about 20 ps obtained by the previous studies [25, 31]. The expected mechanism for photochromic ring-opening here is also suggested by Liu and Morokuma in more accurate theoretical computations [39, 40].

2.4. Mechanism Differences between Real and Model SP. Except for the photochromic processes of SP described in Sections 2.2 and 2.3, there are many other trajectories run in this work; most of them provide information for the ionization of SP molecule, according to the C_1–C_2 dissociation. For instance, the lengthening of C_1–C_2 bond of one representative trajectory for the excited SP is presented in Figure 5. The lifetime of excited state on this trajectory is evaluated to be about 254 fs, while this bond is completely

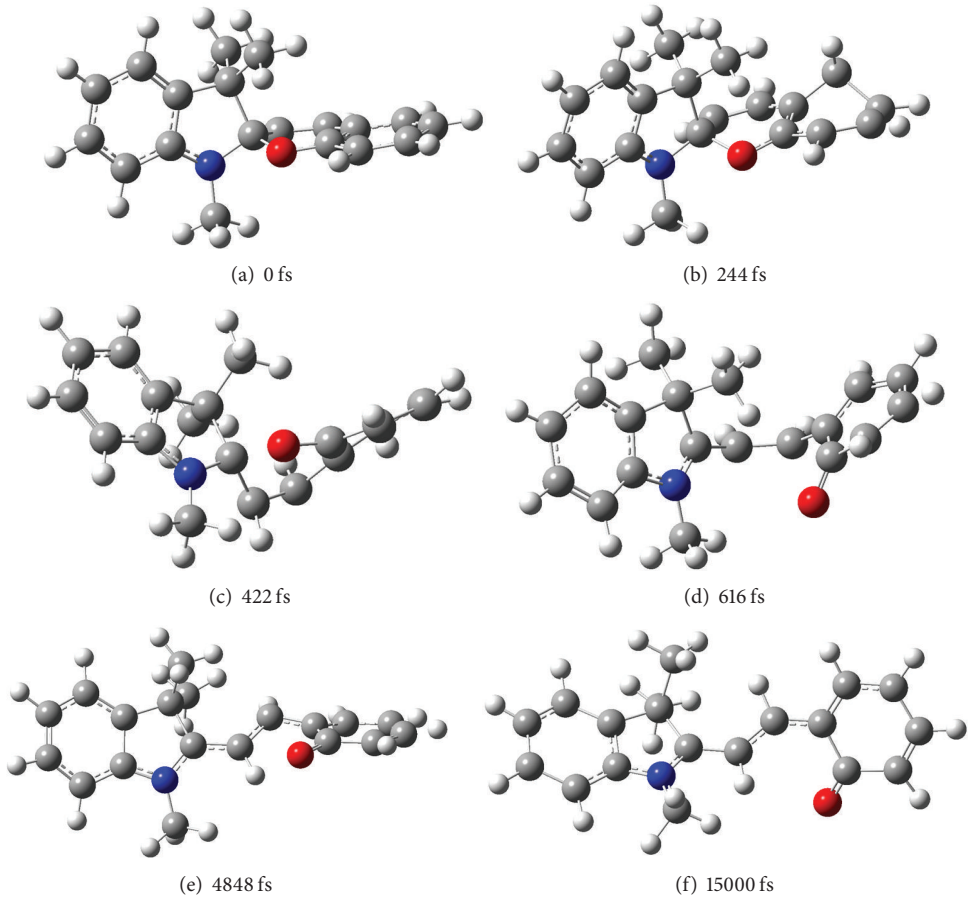

Figure 4: Snapshots taken at different times in a simulation of trans-SP in response to excitation by a 80 fs (FWHM) laser pulse with a fluence of 0.139 kJ/m^2 and photon energy of 3.972 eV, Atom C, H, N, and O are, respectively, denoted by dark grey, French grey, blue, and red; (a)–(f) are at 0 fs, 244 fs, 422 fs, 616 fs, 4848 fs, and 15000 fs, respectively [41].

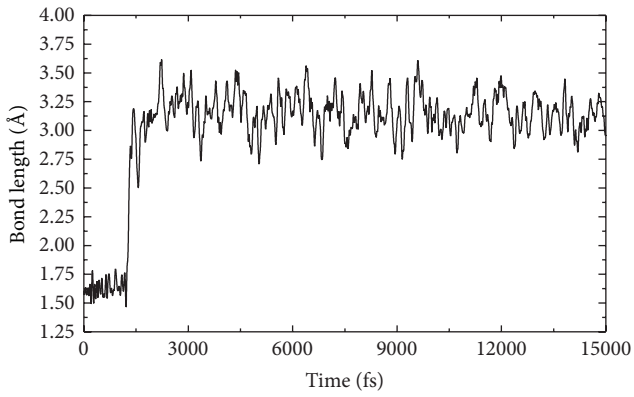

Figure 5: Variations with time of C_1–C_2 bond of cis-SP following application of a 80 fs (FWHM) laser pulse with a fluence of 0.186 kJ/m^2 and photon energy of 4.054 eV and excited state lifetime of 254 fs.

broken after about 1430 fs when the bond length approximately maintains a large average value. The dissociated C_1–C_2 bond is not recovered on this simulation as the high kinetic energies on the ground state are not dispersed to other vibration modes of SP. In comparison with the pathways in the above sections, it can be found the ionization and isomerization of excited SP with the same lifetime 254 fs are both more ultrafast than the ring-opening reaction with lifetime 422 fs, which confirm the previous conclusion that the quantum yield of MC products of this photochromic reaction is relatively less, since the internal conversion from the excited state to the ground state of SP is even more efficient [24, 28].

For the model compounds of SP, the pathways are of a wide variety. With photon excitations, all the four bonds between the central spiro–C and its connected atoms would be dissociated, since the bond lengths of them are similar. The most possible bond lengthening take places between C_1 and C_2 bond in consistent with the real SP molecule. All the typical simulation trajectories of these paths with the photoexcitations are displayed on the Supporting Information from Figures S1 to S7 available online at http://dx.doi.org/10.1155/2014/541791, corresponding to the cleavage of C_1–O bond in Figure S1, the cleavage and then recovery of C_1–C_3 bond in Figure S2, the dissociations of C_1–N, C_1–C_2, and C_1–C_3 bonds in Figures S3–S5, the isomerizations of mSPc and mSPt in Figures S6 and S7,

respectively. Among these trajectories, it is distinct in Figure S1 that, through electronic transition from the excited state to the ground state at 560 fs, the product MC-CCC, which is measured by the experiment but assumed by the computation, is formed. At about 12 ps, this MC conformation is started to convert to the more stable product MC-CTC accompanied with the lengthening of C_1–O bond until the final MC-CTC is completely formed after about 14 ps. This simulation provides a direct evidence for the very recent mechanism proposed by Liu and Morokuma [39, 40] and the previous findings that the transformation from unstable MC form to the final MC conformation takes about 20 ps [25, 31]. In addition, it can be found in Figure S2 that the dissociation of C_1–C_3 bond can be recovered at 13411 fs from the broken form at 9894 fs on the typical trajectory, accompanied with the recovery of cis-SP as the α, β, and γ finally twist back to their initial values, which is similar to the previous suggested process that dissociation of C_1–N bond has also a chance back to the original bonding form [39, 40].

The reason for only three types of trajectories on the simulations of the real SP may be partially deduced by the bond distances of these four bonds around the central spiro–C. As described on Table 1; no matter cis- or trans-SP, the C_1–C_2 bond of the real molecule is elongated while other bonds are shortened in comparison with the model ones, so that the break of C_1–C_2 bond is easier than other bonds. On the other hand, the C_1–O bond can be lengthened since it points to the stable MC product, while the dissociation of C_1–N or C_1–C_3 would result in the ionization of SP, which is more active than both SP and MC stable structures. Hence, no dissociation of C_1–N or C_1–C_3 can be discovered on the dynamic simulations of the real SP, which is different from the previous conclusions that the internal conversion occurs accompanying the dissociation of C_1–N bond from the model compounds [38–40].

3. Conclusions

In summary, we have investigated the photochromic reaction mechanism of SP, employing realistic simulation approach that couples the dynamics of electrons and nuclei. The main simulations follow two different excitations that lead to two altered reaction paths: one is the ultrafast photoisomerization from cis-SP to trans-SP, with respect to internal conversion process to the ground state from excited SP. The process on the excited state involves HOOP torsion of phenyl ring nearby N atom in 254 fs, while the isomerization takes place after the electron transition $\pi_H\sigma_L^*$ to S_0 and goes along the latter potential energy surface with the transformation from cis- to trans-SP in about 10 ps. The other path corresponds to the ring-opening reaction of trans-SP, with regard to the SP to the stable MC conformation MC-TTC. Similarly, the process on the excited state with the lifetime 422 fs involves two cooperative HOOP torsions of two connected six membered rings. After the electronic transition $\pi_H\sigma_L^*$ to the ground state, the first MC product MC-TCC is formed and C_1–O is completely broken after 616 fs, at this moment the unstable product MC-CCC, assigned to appear shortly after photoexcitation [48, 49], emerges and rapidly converts back to the origin MC product MC-TCC. After 4848 fs, this product is transformed to the final stable MC conformation MC-TTC with the large twist around the central C_3–C_6 bond. This simulation trajectory provides a direct proof for confirming the proposed mechanism by the very recent computations [39, 40].

Unlike the possible photodissociation of all the four bonds around the central C_1 atom of the model SP, containing the previously mentioned C_1–N bond cleavage [38–40], the real molecule would usually be ionized with only the C_1–C_2 dissociation. The ultrafast process of the photoinduced ionization and isomerization of SP plays very important roles in the effective internal conversion and less quantum yields of MC products after the photon excitations, which agrees with the previously experimental observations [24, 28].

The current dynamic simulations provide more important complementarity for the mechanism of the ultrafast photochromic ring-opening reaction as well as the internal conversion process of SP. The findings here confirm the previously theoretical proposals for the explanations of the ultrafast processes and even supply other possible reaction paths, for instance, the ultrafast photoisomerization from cis-SP to trans-SP. The foundational information shown in this paper would be available to interpret experimental conservations and helpful to design new photochromic devices based on these kinds of compounds.

Conflict of Interests

The authors declare that there is no conflict of interests regarding the publication of this paper.

Acknowledgments

This work is supported by the National Natural Science Foundation of China (nos. 21003100, 21073242), Natural Science Basic Research Plan in Shaanxi Province of China (nos. 2011JQ2013 and 2014JQ2060), and Special Fund of Education Department of Shaanxi Province (no. 12JK0619). The authors also thank Professor Zhenyi Wen, Associate Professor Huixian Han, and Bingbing Suo for the helpful suggestions.

References

[1] B. L. Feringa, *Molecular Switches*, Wiley-VCH, Weinheim, Germany, 2001.

[2] H. Dürr and H. Bouas-Laurent, *Photochromism: Molecules and Systems*, Elsevier, Amsterdam, The Netherlands, 2003.

[3] H. Bouas-Laurent and H. Dürr, "Organic photochromism," *Pure and Applied Chemistry*, vol. 73, no. 4, pp. 639–665, 2001.

[4] M. Heilemann, P. Dedecker, J. Hofkens, and M. Sauer, "Photoswitches: key molecules for subdiffraction-resolution fluorescence imaging and molecular quantification," *Laser and Photonics Reviews*, vol. 3, no. 1-2, pp. 180–202, 2009.

[5] R. C. Bertelson, "Reminiscences about organic photochromics," *Molecular Crystals and Liquid Crystals Science and Technology A: Molecular Crystals and Liquid Crystals*, vol. 246, pp. 1–8, 1994.

[6] J. P. Desvergne, H. Bouas-Laurent, and A. Deffieux, "Photochromism of anthracene derivatives in fluid solutions and polymers," *Molecular Crystals and Liquid Crystals Science and Technology A: Molecular Crystals and Liquid Crystals*, vol. 246, pp. 111–118, 1994.

[7] K. Schaffner, R. Schmidt, and H. D. Brauer, "Photochromism based on the reversible reaction of singlet oxygen with aromatic compounds," *Molecular Crystals and Liquid Crystals Science and Technology A: Molecular Crystals and Liquid Crystals*, vol. 246, pp. 119–125, 1994.

[8] J. Buback, M. Kullmann, F. Langhojer et al., "Ultrafast bidirectional photoswitching of a spiropyran," *Journal of the American Chemical Society*, vol. 132, no. 46, pp. 16510–16519, 2010.

[9] G. Berkovic, V. Krongauz, and V. Weiss, "Spiropyrans and spirooxazines for memories and switches," *Chemical Reviews*, vol. 100, no. 5, pp. 1741–1753, 2000.

[10] D. A. Parthenopoulos and P. M. Rentzepis, "Three-dimensional optical storage memory," *Science*, vol. 245, no. 4920, pp. 843–845, 1989.

[11] B. L. Feringa, R. A. van Delden, N. Koumura, and E. M. Geertsema, "Chiroptical molecular switches," *Chemical Reviews*, vol. 100, no. 5, pp. 1789–1816, 2000.

[12] F. M. Raymo and S. Giordani, "All-optical processing with molecular switches," *Proceedings of the National Academy of Sciences of the United States of America*, vol. 99, no. 8, pp. 4941–4944, 2002.

[13] K. Fujimoto, M. Amano, Y. Horibe, and M. Inouye, "Reversible photoregulation of helical structures in short peptides under indoor lighting/dark conditions," *Organic Letters*, vol. 8, no. 2, pp. 285–287, 2006.

[14] W. Zhou, D. Chen, J. Li et al., "Photoisomerization of spiropyran for driving a molecular shuttle," *Organic Letters*, vol. 9, no. 20, pp. 3929–3932, 2007.

[15] S. Silvi, A. Arduini, A. Pochini et al., "A simple molecular machine operated by photoinduced proton transfer," *Journal of the American Chemical Society*, vol. 129, no. 44, pp. 13378–13379, 2007.

[16] D. S. Achilleos, T. A. Hatton, and M. Vamvakaki, "Light-regulated supramolecular engineering of polymeric nanocapsules," *Journal of the American Chemical Society*, vol. 134, no. 13, pp. 5726–5729, 2012.

[17] J. Chen, P. Zhang, G. Fang et al., "Synthesis and characterization of novel reversible photoswitchable fluorescent polymeric nanoparticles via one-step miniemulsion polymerization," *Journal of Physical Chemistry B*, vol. 115, no. 13, pp. 3354–3362, 2011.

[18] E. A. Osborne, B. R. Jarrett, C. Tu, and A. Y. Louie, "Modulation of T_2 relaxation time by light-induced, reversible aggregation of magnetic nanoparticles," *Journal of the American Chemical Society*, vol. 132, no. 17, pp. 5934–5935, 2010.

[19] M. K. Maurer, I. K. Lednev, and S. A. Asher, "Photoswitchable spirobenzopyran-based photochemically controlled photonic crystals," *Advanced Functional Materials*, vol. 15, no. 9, pp. 1401–1406, 2005.

[20] R. Q. Albuquerque, J. Kühni, P. Belser, and L. de Cola, "On the reversible photoisomerization of spiropyran-modified zeolite L single crystals," *A European Journal of Chemical Physics and Physical Chemistry*, vol. 11, no. 3, pp. 575–578, 2010.

[21] T. A. Darwish, R. A. Evans, M. James, N. Malic, G. Triani, and T. L. Hanley, "CO_2 triggering and controlling orthogonally multiresponsive photochromic systems," *Journal of the American Chemical Society*, vol. 132, no. 31, pp. 10748–10755, 2010.

[22] N. Tamai and H. Miyasaka, "Ultrafast dynamics of photochromic systems," *Chemical Reviews*, vol. 100, no. 5, pp. 1875–1890, 2000.

[23] C. Lenoble and R. S. Becker, "Photophysics, photochemistry, kinetics, and mechanism of the photochromism of 6′-nitroindolinospiropyran," *Journal of Physical Chemistry*, vol. 90, no. 1, pp. 62–65, 1986.

[24] M. Rini, A. K. Holm, E. T. J. Nibbering, and H. Fidder, "Ultrafast UV-mid-IR investigation of the ring opening reaction of a photochromic spiropyran," *Journal of the American Chemical Society*, vol. 125, no. 10, pp. 3028–3034, 2003.

[25] L. Poisson, K. D. Raffael, B. Soep, J.-M. Mestdagh, and G. Buntinx, "Gas-phase dynamics of spiropyran and spirooxazine molecules," *Journal of the American Chemical Society*, vol. 128, no. 10, pp. 3169–3178, 2006.

[26] M. Kullmann, S. Ruetzel, J. Buback, P. Nuernberger, and T. Brixner, "Reaction dynamics of a molecular switch unveiled by coherent two-dimensional electronic spectroscopy," *Journal of the American Chemical Society*, vol. 133, no. 33, pp. 13074–13080, 2011.

[27] J. Hobley, U. Pfeifer-Fukumura, M. Bletz, T. Asahi, H. Masuhara, and H. Fukumura, "Ultrafast photo-dynamics of a reversible photochromic spiropyran," *Journal of Physical Chemistry A*, vol. 106, no. 10, pp. 2265–2270, 2002.

[28] J. Kohl-Landgraf, M. Braun, C. Özçoban, D. P. N. Gonçalves, A. Heckel, and J. Wachtveitl, "Ultrafast dynamics of a spiropyran in water," *Journal of the American Chemical Society*, vol. 134, no. 34, pp. 14070–14077, 2012.

[29] N. P. Ernsting and T. Arthen-Engeland, "Photochemical ring-opening reaction of indolinospiropyrans studied by subpicosecond transient absorption," *Journal of Physical Chemistry*, vol. 95, no. 14, pp. 5502–5509, 1991.

[30] P. Celani, F. Bernardi, M. Olivucci, and M. A. Robb, "Conical intersection mechanism for photochemical ring opening in benzospiropyran compounds," *Journal of the American Chemical Society*, vol. 119, no. 44, pp. 10815–10820, 1997.

[31] Y. Sheng, J. Leszczynski, A. A. Garcia, R. Rosario, D. Gust, and J. Springer, "Comprehensive theoretical study of the conversion reactions of spiropyrans: substituent and solvent effects," *Journal of Physical Chemistry B*, vol. 108, no. 41, pp. 16233–16243, 2004.

[32] B. O. Roos, *Advances in Chemical Physics*, vol. 69, John Wiley & Sons, New York, NY, USA, 1987.

[33] J. Finley, P.-Å. Malmqvist, B. O. Roos, and L. Serrano-Andrés, "The multi-state CASPT2 method," *Chemical Physics Letters*, vol. 288, no. 2–4, pp. 299–306, 1998.

[34] Y. Kurashige and T. Yanai, "High-performance ab initio density matrix renormalization group method: applicability to large-scale multireference problems for metal compounds," *Journal of Chemical Physics*, vol. 130, no. 23, Article ID 234114, 2009.

[35] D. Ghosh, J. Hachmann, T. Yanai, and G. K. L. Chan, "Orbital optimization in the density matrix renormalization group, with applications to polyenes and ß -carotene," *Journal of Chemical Physics*, vol. 128, no. 14, Article ID 144117, 2008.

[36] Y. Kurashige and T. Yanai, "Second-order perturbation theory with a density matrix renormalization group self-consistent field reference function: theory and application to the study of chromium dimer," *Journal of Chemical Physics*, vol. 135, no. 9, Article ID 094104, 2011.

[37] I. Gómez, M. Reguero, and M. A. Robb, "Efficient photochemical merocyanine-to-spiropyran ring closure mechanism

through an extended conical intersection seam. A model CASSCF/CASPT2 study," *Journal of Physical Chemistry A*, vol. 110, no. 11, pp. 3986–3991, 2006.

[38] S.-L. Marta, E. Carlos Manuel, H.-R. Jose, and S.-A. Luis, "Ultrafast ring-opening/closing and deactivation channels for a model spiropyran-merocyanine system," *Journal of Physical Chemistry A*, vol. 115, no. 33, pp. 9128–9138, 2011.

[39] F. Liu and K. Morokuma, "Multiple pathways for the primary step of the spiropyran photochromic reaction: a CASPT2//CASSCF study," *Journal of the American Chemical Society*, vol. 135, no. 29, pp. 10693–10702, 2013.

[40] F. Y. Liu, Y. Kurashige, T. Yanai, and K. Morokuma, "Multireference Ab initio density matrix renormalization group (DMRG)-CASSCF and DMRG-CASPT2 Study on the Photochromic Ring Opening of Spiropyran," *Journal of Chemical Theory and Computation*, vol. 9, no. 10, pp. 4462–4469, 2013.

[41] V. I. Minkin, A. V. Metelitsa, I. V. Dorogan, B. S. Lukyanov, S. O. Besugliy, and J.-C. Micheau, "Spectroscopic and theoretical evidence for the elusive intermediate of the photoinitiated and thermal rearrangements of photochromic spiropyrans," *Journal of Physical Chemistry A*, vol. 109, no. 42, pp. 9605–9616, 2005.

[42] T.-S. Chu, Y. Zhang, and K.-L. Han, "The time-dependent quantum wave packet approach to the electronically nonadiabatic processes in chemical reactions," *International Reviews in Physical Chemistry*, vol. 25, no. 1-2, pp. 201–235, 2006.

[43] K. Han, J. Huang, S. Chai, S. Wen, and W. Deng, "Anisotropic mobilities in organic semiconductors," *Nature Protocol Exchange*, 2013.

[44] Y. Dou, B. R. Torralva, and R. E. Allen, "Semiclassical electron-radiation-ion dynamics (SERID) and cis-trans photoisomerization of butadiene," *Journal of Modern Optics*, vol. 50, no. 15–17, pp. 2615–2643, 2003.

[45] Y. Dou and R. E. Allen, "Another important coordinate in the photoisomerization of cis-stilbene," *Chemical Physics Letters*, vol. 378, no. 3-4, pp. 323–329, 2003.

[46] Y. Lei, S. Yuan, Y. Dou, Y. Wang, and Z. Wen, "Detailed dynamics of the nonradiative deactivation of adenine: a semiclassical dynamics study," *Journal of Physical Chemistry A*, vol. 112, no. 37, pp. 8497–8504, 2008.

[47] G. Zhai, P. Yang, S. Wu, Y. Lei, and Y. Dou, "A semiclassical molecular dynamics of the photochromic ring-opening reaction of spiropyran," *Chinese Chemical Letters*, vol. 25, no. 5, pp. 727–731, 2014.

[48] S. A. Krysanov and M. V. Alfimov, "Ultrafast formation of transients in spiropyran photochromism," *Chemical Physics Letters*, vol. 91, no. 1, pp. 77–80, 1982.

[49] S. A. Antipin, A. N. Petrukhin, F. E. Gostev et al., "Femtosecond transient absorption spectroscopy of non-substituted photochromic spirocompounds," *Chemical Physics Letters*, vol. 331, no. 5-6, pp. 378–386, 2000.